

# Phase-Field Modeling of Spiral Eutectic Dendrites

PH.D. DISSERTATION

**László Rátkai**

Institute for Solid State Physics and Optics  
Wigner Research Centre for Physics  
Hungarian Academy of Sciences

**Supervisor: Dr. Tamás Pusztai, D.Sc.**



EÖTVÖS LORÁND UNIVERSITY  
FACULTY OF SCIENCE

Doctoral School of Physics  
Head of the School: Prof. Dr. Tamás Tél, D.Sc.

Materials Science and Solid State Physics Program  
Program Leader: Prof. Dr. István Groma, D.Sc.

Budapest

2018



# Contents

<b>1</b>	<b>Introduction</b>	<b>1</b>
1.1	Motivation and objective . . . . .	3
1.2	Structure of the dissertation . . . . .	5
<b>2</b>	<b>Theoretical background</b>	<b>7</b>
2.1	Thermodynamics of a binary system . . . . .	7
2.1.1	Ideal and regular solution models . . . . .	10
2.1.2	Equilibrium of phases . . . . .	13
2.1.3	Multi-component alloys and Gibbs' phase rule . . . . .	15
2.2	Phase diagrams . . . . .	16
2.2.1	Binary eutectic systems . . . . .	18
2.2.2	Ternary eutectic systems . . . . .	20
2.3	Microstructure . . . . .	22
2.3.1	Excess energy of a curved interface . . . . .	22
2.3.2	Dendritic growth . . . . .	24
2.3.3	Eutectics . . . . .	29
2.3.4	Spiral two-phase dendrites . . . . .	31
2.3.5	Jackson–Hunt theory for lamellar eutectic growth . . . . .	32
2.4	The Phase-Field Method . . . . .	34
2.4.1	Field variables of the Phase-Field Method . . . . .	34
2.4.2	Free energy functional . . . . .	35
2.4.3	Equations of motion . . . . .	36
<b>3</b>	<b>Model description</b>	<b>39</b>
3.1	Free energy functional . . . . .	39
3.2	Equations of motion . . . . .	41
3.3	Discretized equations . . . . .	43
<b>4</b>	<b>Numerical simulations</b>	<b>45</b>
4.1	The simulation box . . . . .	45
4.2	The simulation program . . . . .	47

4.2.1	Structure of the simulation program . . . . .	50
4.2.2	Visualization of the results . . . . .	51
4.3	Starting configurations . . . . .	52
4.4	Reference conditions . . . . .	53
4.5	Hardware used . . . . .	53
<b>5</b>	<b>Results and discussion</b>	<b>55</b>
5.1	Formation of a two-phase dendrite . . . . .	55
5.2	Domain of ordered two-phase dendrites . . . . .	57
5.3	Dendrite morphology . . . . .	59
5.3.1	Characteristic quantities . . . . .	59
5.3.2	Morphology of a single spiral dendrite . . . . .	60
5.3.3	Effect of pulling speed and the Jackson–Hunt scaling . . . . .	61
5.3.4	Effect of solid-liquid interface free energy . . . . .	64
5.3.5	Effect of kinetic anisotropy . . . . .	65
5.3.6	Eutectic wavelength vs. tip radius . . . . .	66
5.4	Eutectic patterns . . . . .	68
5.4.1	Pattern selection . . . . .	72
5.4.2	Rotation direction . . . . .	74
5.4.3	Defects in the spiraling eutectic patterns . . . . .	75
5.5	Significance of the presence of anisotropy in the spiral growth . . . . .	76
5.5.1	Eutectic colonies and cells . . . . .	77
5.5.2	Stabilizing effect of the anisotropy . . . . .	79
5.6	Off-eutectic compositions . . . . .	85
5.6.1	Gradually changing composition . . . . .	86
5.6.2	Directly set composition . . . . .	90
<b>6</b>	<b>Summary</b>	<b>95</b>
	<b>References</b>	<b>99</b>
	<b>List of Publications</b>	<b>107</b>
	<b>Theses</b>	<b>109</b>
	<b>Résumé</b>	<b>111</b>
	<b>Összefoglaló</b>	<b>113</b>
	<b>Acknowledgments</b>	<b>115</b>

# Chapter 1

## Introduction

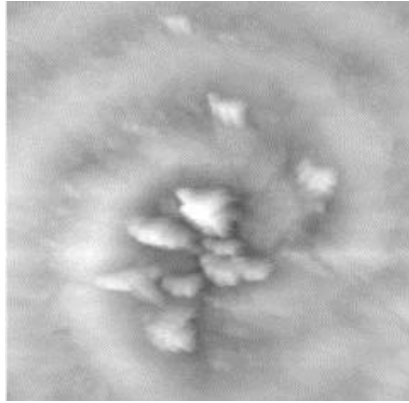
Spiral pattern is a ubiquitous structural feature that is observed in broad variety of systems at length scales of wide range. For example spiral galaxies [1], cyclones [2], banded spherulites in polymeric systems [3], biological excitable systems [4, 5], sunflowers [6], oscillating chemical reactions [7, 8], spiraling growth edges on flat crystalline surfaces [9], ridges in sputtered high-temperature superconducting thin films [10, 11], certain semiconductor materials grown by molecular beam epitaxy [12], *binary* eutectics [13, 14], helical Liesegang systems [8, 15], and the recently discovered *ternary* eutectic dendrites [16]. A few illustrations are shown in Fig. 1.1.

Although the formation mechanism of spiral structures is an actively researched topic for a long time, a general explanation is not available partly due to the diversity of the underlying physical phenomena. While the details differ in various realizations of spiral growth, diffusion and phase separation often play a role in the respective models. For example, the aggregation of starving cells is controlled by propagating spiral waves of a chemo-attractant, often yielding multiarmed spiral patterns in the case of slime mold [17]. In binary eutectics spiraling has been associated with a specific anisotropy of the free energy of the solid-solid interface [13], the presence of screw dislocations [18], or recently to fingering driven by osmotic flow [19]. In contrast, the newly discovered spiraling ternary eutectic dendrites emerge from the interplay of two-phase eutectic solidification with the Mullins-Sekerka-type diffusional instability caused by a third component, which has different solubility in the solid and liquid phases [16].

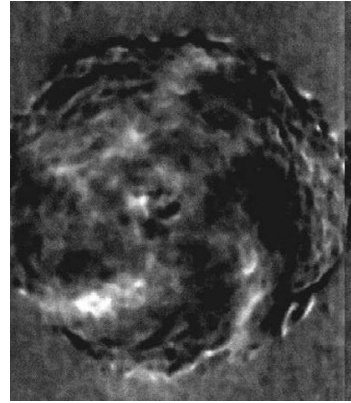
Models of spiral growth range from wave theory [20, 21], via the FitzHugh-Nagumo



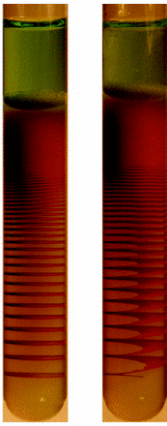
(a) Whirlpool Galaxy. [1]



(b) Spherulite nucleus with a spiral structure. [3]



(c) Five-armed spiral in the mound. [4]



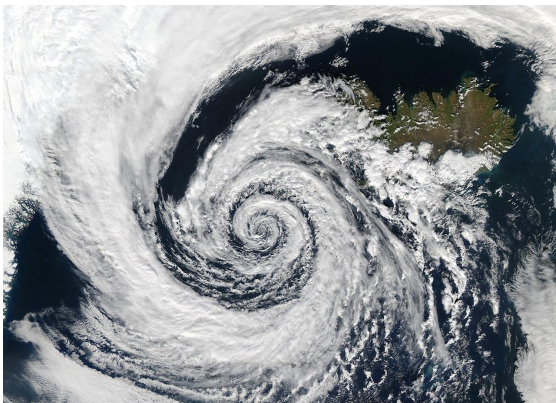
(d) Bands and helices in Liesegang system. [8]



(e) STM image of sputtered thin film of  $\text{YBa}_2\text{Cu}_3\text{O}_7$ . [10]



(f) Typical microstructure of Zn-3%-Mg alloy. [13]



(g) An extratropical cyclone near Iceland. Source: Wikipedia/NASA's Aqua/MODIS satellite



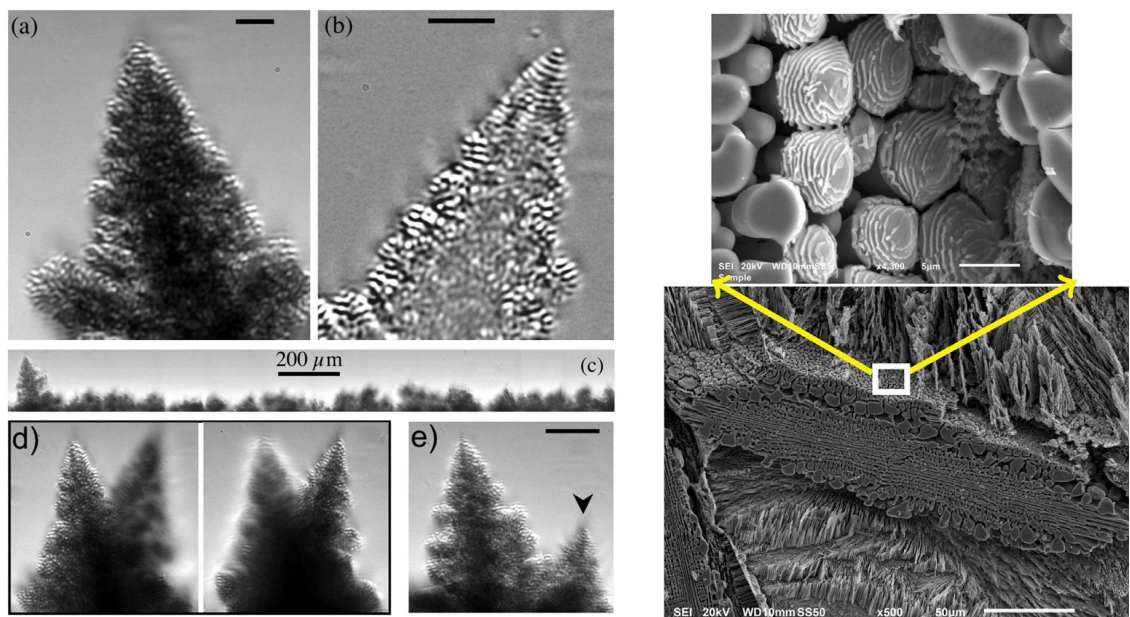
(h) Seeds in a head of sunflower form a multi-armed spiral. Source: Wikipedia/Esdras Calderan

**Figure 1.1.** Various spiral formations in the nature.

(FN) theory for excitable media [17] and reaction-diffusion models [22, 15, 23] to the Ginzburg-Landau/phase-field type models [24, 25]. Studies of biological excitable media, relying on the FN model, have clarified essential features of spiral growth [17]: The mechanism by which the multi-arm spirals do form is the attraction of single spirals rotating in the same direction, whereas the number of spiral arms is associated with the ratio of the single spiral period to the refractoriness of the medium. Even pure confined systems were found to display chiral symmetry breaking, and thus spiral growth in phase-field simulations [26]. A recent work based on Cahn-Hilliard type reaction-diffusion model of helical Liesegang systems indicate that single and multiple helices may occur and the fluctuations choose from the possible configurations [15].

## 1.1 Motivation and objective

The main motivation of this work were the experimental results of Akamatsu *et al.* [16]. These two-phase spiraling structures (see left panel of Fig. 1.2) were exciting new results in the area of eutectic systems, which were investigated both experimentally and theoretically for a long time. Our goal was to construct a suitable physical model,



(a) Two-phase spiral dendrites in succinonitrile based ternary alloy. [16]

(b) Spiral-like structures in Ni-Al-Zr alloy. [27]

**Figure 1.2.** Spiraling structures in experiments.

and show that by a simple ternary extension of the standard binary phase-field theory we would be able to describe the formation of spiraling eutectic dendrites, offering thus the first model that is able to capture details of these exotic growth patterns.

Most recently, after our work, spiraling structures have been found by Lahiri *et al.* [27] in a Ni-Al-Zr ternary eutectic alloy as well (see right panel of Fig. 1.2). They also used a ternary phase-field model, similar to ours, to investigate these eutectic structures.

A proposed optical application area for these helical structures is the chiral metamaterials, which have an unique property: a negative refraction that never occurs otherwise in the nature [28]. A log-pile-shaped 3D lattice made of helical structures can act as a metamaterial, resulting in a negative refraction index for one polarization within a given frequency range. Furthermore, perfect lens can be made out of metamaterials, where the only limiting factor of the resolution is the quality of the manufacture, not the wavelength of the lightsource.

Some unusually regular structures seen in Al-Cr-Nb ternary eutectic alloy [29] could also be the results of the two-phase spiraling growth. In Fig. 1.3 a dense array of diagonally oriented, “fish spine cell”-like structures can be seen. Such pattern can be

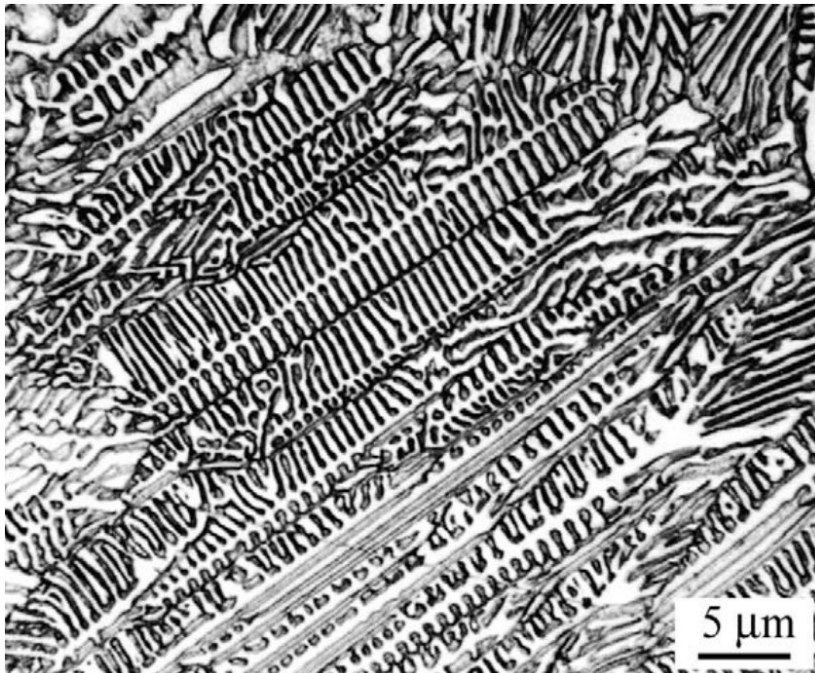



**Figure 1.3.** Complex regular microstructure (“fish spine cell” morphology) presented by the eutectic alloy 49.3%Al–39.7%Cr–11%Nb. [29]



the result of multiple two-phase spiraling dendrites with unequal volume fraction, when they are growing in the same direction.

## 1.2 Structure of the dissertation

The dissertation consist of five main chapters. In Chapter 2, I start with the theoretical background which introduces the phase diagrams, the eutectic systems and the formation of various microstructures, including the experimental two-phase spiral dendrites, then lastly the phase-field method. In Chapter 3, I describe our model we developed, the ternary extension of the phase-field method. In Chapter 4, I show the simulation environment, the programs developed and how the simulation data were evaluated. In Chapter 5, I present our results.

The dissertation has numerous supplementary videos located on this dedicated website<sup>1</sup>: <https://rlphd.phasefield.hu>. If there is a corresponding video to a figure, then there will be a direct link (indicated by a small video icon: ) at the end of their caption. The numbering of the videos are corresponding to the numbering of the figures in the dissertation.

---

<sup>1</sup>A backup can be found on the <http://raptor.web.elte.hu/rlphd/> address.



# Chapter 2

## Theoretical background

In this chapter I briefly summarize the previous relevant studies, starting with some basic thermodynamics in order to define the Gibbs free energy for a multi-component, multi-phase system. After that, I present a binary and a ternary eutectic phase diagram and describe how to obtain them using the Gibbs free energy functions. At the end of the chapter, I present various eutectic and dendritic microstructures, including the two-phase spiral dendrites.

### 2.1 Thermodynamics of a binary system

A *system* contains all of the matter that can interact within a space of defined boundary. This system may contain several *components*, chemically distinct entities such as pure elements or molecules. There may also be several *phases*, which are defined as portions of a system that are physically distinct in terms of their state (solid, liquid, vapor), crystal structure or composition. For example in the binary alloy Al-Cu, various phases can be present, including a liquid, in which both elements are completely miscible; limited solid solutions of Cu in Al and Al in Cu; and intermetallic compounds, such as  $\text{Al}_2\text{Cu}$ , etc.

Consider the volume illustrated in Fig. 2.1, composed of a homogeneous phase made up of two components (atoms or molecules), labeled A and B. For the moment, the mixture will be assumed to consist of a single phase, i.e. a solution of the two components. B is assumed to be the minor component and is called the solute, whereas the major component A is the solvent. The system contains  $n_A$  moles of component

A, and  $n_B$  moles of species B.

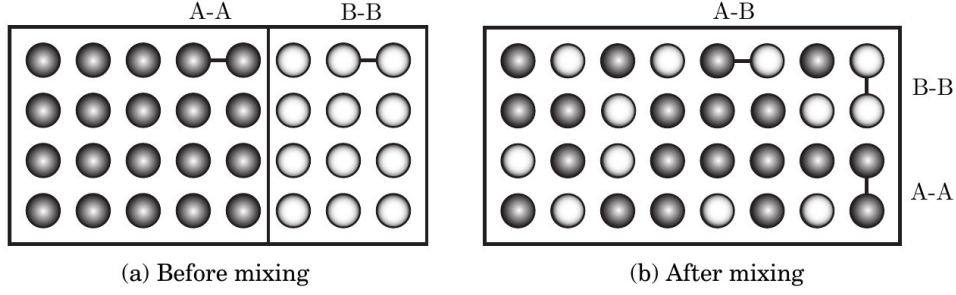


**Figure 2.1.** Schematic of the mixing of  $n_A$  moles of A atoms/molecules (black spheres) with  $n_B$  moles of B atoms/molecules (white spheres). (a) Before the components are mixed, there are only A-A and B-B bonds. (b) Upon forming a solution, some of these bonds are replaced by A-B bonds. [30]

The total number of moles:  $n = n_A + n_B$ . One can also specify the *composition* using the mole fraction of each component;  $X_A$  and  $X_B$ , defined as

$$X_A = \frac{n_A}{n_A + n_B} \quad \text{and} \quad X_B = \frac{n_B}{n_A + n_B}. \quad (2.1)$$

By definition, it follows that  $X_A + X_B = 1$ .

The most frequently used thermodynamic state variable for solidification is the *Gibbs free energy*,  $G = G(T, V)$ , which can be expressed in a single component system as

$$G = E - TS + pV, \quad (2.2)$$

where  $E = E(T, V)$  is the internal energy,  $S = S(p, T)$  is the entropy,  $T$  is the temperature,  $p$  is the pressure and  $V$  is the volume of the system. In a binary system the molecules or atoms are interacting when they are mixed, thus the Gibbs free energy of the solution varies with the composition as well. Writing  $G = G(T, p, n_A, n_B)$ , the differential  $dG$  can be written as

$$\begin{aligned} dG(p, T, n_A, n_B) = & V(p, T, n_A, n_B)dp - S(p, T, n_A, n_B)dT \\ & + \mu_A(p, T, X_B)dn_A + \mu_B(p, T, X_B)dn_B, \end{aligned} \quad (2.3)$$

where  $\mu_A$  and  $\mu_B$  are the *chemical potential* of each species defined as:

$$\mu_A = \left( \frac{\partial G}{\partial n_A} \right)_{p, T, n_B} \quad \text{and} \quad \mu_B = \left( \frac{\partial G}{\partial n_B} \right)_{p, T, n_A}. \quad (2.4)$$

Dividing Eq. (2.3) by  $n$ , and invoking relation  $dX_A = -dX_B$ , one can write the expression in terms of molar quantities:

$$dG^m(p, T, X_B) = V^m(p, T, X_B)dp - S^m(p, T, X_B)dT + [\mu_B(p, T, X_B) - \mu_A(p, T, X_B)]dX_B. \quad (2.5)$$

Keeping the temperature and pressure constant,  $G$  is a *homogeneous function* of the  $n_j$  ( $j$  is A or B), meaning that its magnitude is directly proportional to the amount of its constituents:

$$G = n_A\mu_A + n_B\mu_B \quad (\text{Fixed } T, p) \quad (2.6)$$

This expression is shown graphically in Fig. 2.2. Computing the differential of Eq. (2.6):

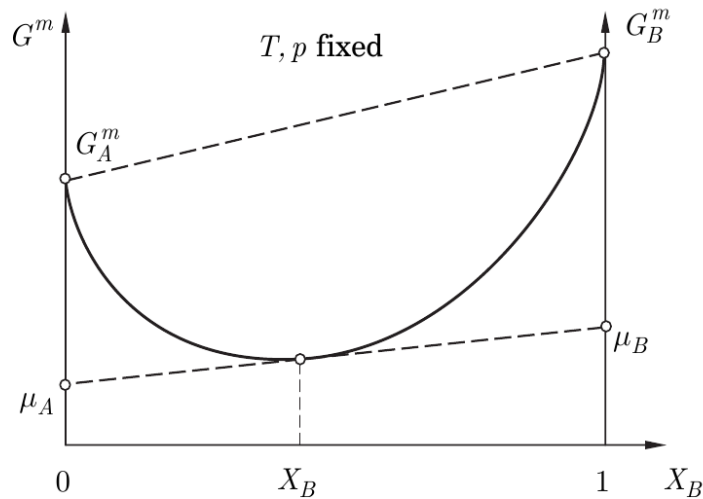


**Figure 2.2.** Molar free energy of a binary solution as a function of the mole fraction of component B, showing the tangent construction to compute  $\mu_A$  and  $\mu_B$  chemical potentials. [30]

$$dG = n_A d\mu_A + n_B d\mu_B + \mu_A dn_A + \mu_B dn_B \quad (2.7)$$

Choosing fixed  $p$  and  $T$  in Eq. (2.3), and equating  $dG$  with Eq. (2.7) yields the *Gibbs-Duhem* equation:

$$n_A d\mu_A + n_B d\mu_B = 0. \quad (2.8)$$

Dividing Eq. (2.6) by  $n$  (the total number of moles) gives:

$$G^m = X_A\mu_A + X_B\mu_B, \quad (2.9)$$

then differentiate with respect to  $X_B$  (using  $X_A + X_B = 1$  relation):

$$\frac{\partial G^m}{\partial X_B} = \mu_B - \mu_A. \quad (2.10)$$

Combining Eq. (2.9) and Eq. (2.10) yields the following two equations:

$$\begin{aligned} \mu_A(T, p, X_B) &= G^m(T, p, X_B) - X_B \left( \frac{\partial G^m}{\partial X_B} \right)_{p,T} \\ \mu_B(T, p, X_B) &= G^m(T, p, X_B) + (1 - X_B) \left( \frac{\partial G^m}{\partial X_B} \right)_{p,T}. \end{aligned} \quad (2.11)$$

These define the *tangent rule construction*, giving the chemical potential of components A and B for a solution having a composition  $X_B$  (see Fig. 2.2). If the molar free energy  $G^m$  around composition  $X_B$  (with fixed  $p$  and  $T$ ) is known, the tangent to  $G^m$  at that point intersects the vertical axes,  $X_B = 0$  and  $X_B = 1$ , at the values  $\mu_A$  and  $\mu_B$ , respectively.

### 2.1.1 Ideal and regular solution models

To incorporate the effect of thermodynamic variables on the free energy of the solution, two models are commonly used: the ideal- and the regular solution models. We will also use them in our ternary phase-field model: ideal solution model for the liquid phase and regular solution model for the solid phases.

The Gibbs free energy contribution of the mixture can be written as  $\Delta G_{\text{mix}} = \Delta H_{\text{mix}} - T\Delta S_{\text{mix}}$ , where  $\Delta H_{\text{mix}}$  is the *enthalpy of mixing* and  $\Delta S_{\text{mix}}$  is the *entropy of mixing*. The total Gibbs free energy of the solution is defined by the free energies of the pure components before the mixing with this additional  $\Delta G_{\text{mix}}$  mixing contribution term. For a completely disordered solution such as illustrated in Fig. 2.1 (b), the formation of one mole of solution with  $X_A$  moles of A and  $X_B$  moles of B will create

on average

$$\begin{aligned}
& 0.5X_A N_0 \times X_A N_b && \text{bonds } (A-A), \\
& 0.5[X_A N_0 \times X_B N_b + X_B N_0 \times X_A N_b] && \text{bonds } (A-B), \\
& 0.5X_B N_0 \times X_B N_b && \text{bonds } (B-B),
\end{aligned} \tag{2.12}$$

where  $N_0$  is the Avogadro constant and  $N_b$  is the coordination number. Thus there are  $X_J N_0$  atoms or molecules of species  $J$  and each one is surrounded by  $N_b$  neighbors, whose types A/B are precisely in the ratio  $X_A/X_B$  if the solution is random. The internal energy associated with the bonds is given by:

$$E_i^m = 0.5N_0 N_b (X_A^2 \epsilon_{AA} + X_B^2 \epsilon_{BB} + 2X_A X_B \epsilon_{AB}), \tag{2.13}$$

where  $\epsilon_{IJ}$  is the bond energy between components  $I$  and  $J$ . This equation can also be written as:

$$\begin{aligned}
E_i^m &= 0.5N_0 N_b (X_A^2 \epsilon_{AA} + X_B^2 \epsilon_{BB} + X_A X_B \epsilon_{AA} + X_A X_B \epsilon_{BB}) \\
&+ 0.5N_0 N_b X_A X_B (2\epsilon_{AB} - \epsilon_{AA} - \epsilon_{BB}).
\end{aligned} \tag{2.14}$$

Using that  $X_A + X_B = 1$ :

$$E_i^m = X_A E_{iA}^m + X_B E_{iB}^m + \Omega^m X_A X_B, \tag{2.15}$$

where the last term is called the *enthalpy of mixing*:  $\Delta H_{\text{mix}} = \Omega^m X_A X_B$  and

$$\begin{aligned}
E_{iA}^m &= 0.5N_0 N_b \epsilon_{AA} \\
E_{iB}^m &= 0.5N_0 N_b \epsilon_{BB} \\
\Omega^m &= N_0 N_b \bar{\epsilon}_{AB} = N_0 N_b \left( \epsilon_{AB} - \frac{\epsilon_{AA} + \epsilon_{BB}}{2} \right)
\end{aligned} \tag{2.16}$$

The bonding energy  $\bar{\epsilon}_{AB} = N_0 N_b [\epsilon_{AB} - 0.5(\epsilon_{AA} + \epsilon_{BB})]$  measures the relative affinity of atoms A and B. The sign of  $\bar{\epsilon}_{AB}$  determines whether the mixing is favorable for the components. When  $\bar{\epsilon}_{AB} < 0$ , the system can lower its energy by forming A-B bonds, thus will have a tendency to form a phase where A components have a B-environment and vice-versa. However, when  $\bar{\epsilon}_{AB} > 0$ , the bonding energy between A

and B components are smaller than the average A-B and B-B bonding energy. In this case the system can lower its energy by having demixing between A and B species.

To determine the Gibbs free energy of the solution, the vibrational energy must be taken into account as well. The simplest model consistent with the internal energy computed above is one with only two contributions to the free energy beyond the simple rule of mixtures: the excess energy  $\Omega^m X_A X_B$  and the *entropy of mixing*,  $S_{\text{mix}}^m$ . The latter is modeled by enumerating the number of distinguishable configurations of a collection containing  $N_A$  A-components and  $N_B$  B-components ( $N_A + N_B = N_0$ ). After Boltzmann, the molar entropy of mixing is then given by

$$S_{\text{mix}}^m = k_B \ln \frac{(N_A + N_B)!}{N_A! N_B!}, \quad (2.17)$$

where  $k_B$  is the Boltzmann's constant. Using the Stirling's formula ( $\ln x! \approx x \ln x - x$  for  $x \rightarrow \infty$ ), the entropy of mixing can be written as:

$$S_{\text{mix}}^m = -R(X_A \ln X_A + X_B \ln X_B), \quad (2.18)$$

where  $R = k_B N_0$  is the gas constant.

The Gibbs free energy of the solution can be derived as follows:

$$\begin{aligned} G^m &= E^m + pV^m - TS^m \\ &= (X_A E_A^m + X_B E_B^m) + p(X_A V_A^m + X_B V_B^m) - T(X_A S_A^m + X_B S_B^m) \\ &\quad + \Omega^m X_A X_B - TS_{\text{mix}}^m \\ &= X_A (E_A^m + pV_A^m - TS_A^m) + X_B (E_B^m + pV_B^m - TS_B^m) + \Omega^m X_A X_B - TS_{\text{mix}}^m \\ G^m &= X_A G_A^m + X_B G_B^m + \Omega^m X_A X_B - TS_{\text{mix}}^m, \end{aligned} \quad (2.19)$$

where  $S_{A/B}^m$  are the molar entropies and  $G_{A/B}^m$  are the molar free energies of the pure components before mixing. Inserting Eq. (2.18) into this equation, one gets the general expression for the free energy of a *regular solution*:

$$G_{\text{regular}}^m = X_A G_A^m + X_B G_B^m + \Omega^m X_A X_B + RT(X_A \ln X_A + X_B \ln X_B). \quad (2.20)$$

When  $\Omega^m = 0$ , i.e. the bonds between A and B components are to those between the



pure substance, the expression reduces to the *ideal solution*:

$$G_{\text{ideal}}^m = X_A G_A^m + X_B G_B^m + RT(X_A \ln X_A + X_B \ln X_B). \quad (2.21)$$

### 2.1.2 Equilibrium of phases

Consider a single component, closed system consisting of two phases,  $\alpha$  and  $\beta$  (e.g. solid and liquid) and assume that mechanical and thermal equilibrium have been established (i.e. fixed  $p$  and  $T$ ). The second law of thermodynamics states that the free energy of this system at equilibrium must be at minimum. The Gibbs free energy of the system is the following:

$$G = n_\alpha G_\alpha^m + n_\beta G_\beta^m, \quad (2.22)$$

where  $G_\alpha$  and  $G_\beta$  are the molar Gibbs free energies of the phases and  $n_\alpha$  and  $n_\beta$  are the number of moles of each phase with the constraint  $n_\alpha + n_\beta = n = \text{constant}$ . Dividing Eq. (2.22) by  $n$  and introducing mole fraction of phases,  $\chi_i$ , which have the property:  $\chi_\alpha + \chi_\beta = 1$ , Eq. (2.22) can be written as:

$$G^m = \chi_\alpha G_\alpha^m + \chi_\beta G_\beta^m. \quad (2.23)$$

Since the equilibrium corresponds to a minimum free energy, derivative of Eq. (2.23) with respect to  $\chi_\alpha$  must vanish:

$$\frac{\partial G^m}{\partial \chi_\alpha} = 0 = G_\alpha^m - G_\beta^m. \quad (2.24)$$

Therefore, at equilibrium a single component system consisting of two phases must satisfy the following conditions:

- $T_\alpha = T_\beta = T \quad \Rightarrow$  thermal equilibrium
- $p_\alpha = p_\beta = p \quad \Rightarrow$  mechanical equilibrium
- $G_\alpha^m = G_\beta^m = G^m \quad \Rightarrow$  phase equilibrium

The conditions for equilibrium of several phases in a single component system can be extended to multiple components. Consider a closed system containing A and B

components and two phases: solid and liquid. The compositions in these phases are:  $X_{Bs}$  for the solid and  $X_{Bl}$  for the liquid. At fixed pressure and temperature, the molar free energies of the two phases are  $G_s^m$  and  $G_l^m$ . If the two free energy curves do not cross, the minimum free energy of the system would always be described by the lowest free energy curve over the whole composition field, and thus only one phase (with the lowest free energy) would be present in the system. If the two curves intersect, as illustrated in Fig. 2.3 (a), there are three regions. Far from the  $X_{B0}$  intersection point, only one phase (with the lowest free energy) would be present in the system: solid on the left side, and liquid on the right side. At the  $X_{B0}$  intersection point, the free energy of the two phases are equal:  $G_s^m = G_l^m$ , but it is not an equilibrium point, since the chemical potentials of the two components in the solid and liquid are not equal [see Fig. 2.3 (a)]. Thus the system could decrease its free energy by transferring solute components B from the solid to the liquid (gain of energy:  $\mu_{Bl} - \mu_{Bs} < 0$ ), and solvent components A from the liquid to the solid ( $\mu_{As} - \mu_{Al} < 0$ ). The variation of free energy of the system during this operation would be given by:

$$dG = (\mu_{As} - \mu_{Al})dn_A + (\mu_{Bs} - \mu_{Bl})dn_B < 0. \quad (2.25)$$

Therefore, the equilibrium condition for two co-existing phases corresponds to

$$\mu_{As} = \mu_{Al} \quad \text{and} \quad \mu_{Bs} = \mu_{Bl}. \quad (2.26)$$

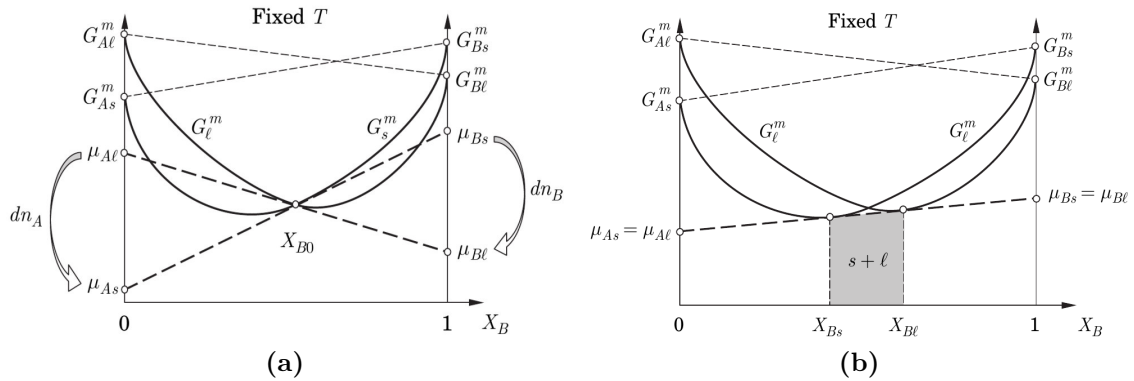


**Figure 2.3.** Gibbs free energies of the solid and liquid phases as function of the composition  $X_B$ . (a) Chemical potentials at the intersection of the curves. (b) The condition of equilibrium when solid and liquid phases co-exist is illustrated with the common tangent. [30]

This condition for equilibrium is illustrated in Fig. 2.3 (b). The  $\mu_{As} = \mu_{Al}$  and  $\mu_{Bs} = \mu_{Bl}$  conditions require that the compositions for the solid and liquid phases ( $X_{Bs}$  and  $X_{Bl}$ ) lie on the *common tangent*. For any alloy, whose composition lies in the interval  $X_{Bs} < X_B < X_{Bl}$ , the system will minimize its free energy by having both phases with composition  $X_{Bs}$  for the solid and  $X_{Bl}$  for the liquid. To ensure the solute conservation, the fraction of phases will change from fully solid (at composition  $X_{Bs}$ ) to fully liquid (at composition  $X_{Bl}$ ). The mole fractions of phases,  $\chi_s$  and  $\chi_l$  can be calculated as

$$\chi_s X_{Bs} + \chi_l X_{Bl} = X_B. \quad (2.27)$$

The ratio  $X_{Bs}/X_{Bl}$  of the solute element B in the solvent A is called the *partition coefficient*,  $k_0^m$ :

$$k_0^m = X_{Bs}/X_{Bl}. \quad (2.28)$$

### 2.1.3 Multi-component alloys and Gibbs' phase rule

A similar procedure exists for dealing with multi-component alloy consisting of  $N_c$  chemical species (A, B, C, ...). Assuming that element A is the solvent, the molar Gibbs free energy is a function of  $T, p$  and the  $(N_c - 1)$  solute compositions. Considering a regular solution model with only two-element interactions, the Gibbs free energy is given by:

$$G^m = \sum_{I=1}^{N_c} X_I G_I^m + \sum_{I=1}^{N_c} \sum_{J>I}^{N_c} \Omega_{IJ}^m X_I X_J + RT \sum_{I=1}^{N_c} X_I \ln X_I, \quad (2.29)$$

where  $G_I^m$  is the molar Gibbs free energy of the pure component I, and  $\Omega_{IJ}^m$  is the interaction parameter between I and J components. At fixed temperature and pressure, the free energy curves become hypersurfaces in  $(N_c - 1)$ -dimensional space, e.g. surfaces in a ternary alloy. The conditions for having  $N_\xi$  phases ( $\alpha, \beta, \gamma, \dots, \xi$ ) in equilibrium is to have the temperature, pressure and chemical potentials of all the components equal in all of the phases:

- $T_\alpha = T_\beta = T_\gamma = \dots = T_{N_\xi} = T \quad \Rightarrow$  thermal equilibrium
- $p_\alpha = p_\beta = p_\gamma = \dots = p_{N_\xi} = p \quad \Rightarrow$  mechanical equilibrium
- $\mu_{A\alpha} = \mu_{A\beta} = \mu_{A\gamma} = \dots = \mu_{A\xi} = \mu_A \quad \Rightarrow$  chemical eq. of A component
- $\mu_{B\alpha} = \mu_{B\beta} = \mu_{B\gamma} = \dots = \mu_{B\xi} = \mu_B \quad \Rightarrow$  chemical eq. of B component

- $\vdots$
- $\mu_{N_c\alpha} = \mu_{N_c\beta} = \mu_{N_c\gamma} = \dots = \mu_{N_c\xi} = \mu_{N_c} \quad \Rightarrow$  chemical eq. of  $N_c$  comp.

At fixed  $p$  and  $T$ , the condition of equilibrium given by the chemical potentials can be represented as a common hyperplane tangent to the free energy hypersurfaces of all the co-existing phases. For example a plane tangent to a surface for a ternary alloy.

Gibbs defined the degrees of freedom of a system,  $N_F$ , as the number of independent variables which can be changed and still maintain the same number of phases in equilibrium. In a multi-component alloy consisting of  $N_c$  component in which  $N_\xi$  phases are present, the free variables are:

- temperature: 1 variable
- pressure: 1 variable
- $N_c - 1$  free composition in each phase:  $N_\xi(N_c - 1)$  variables

The number of constraints imposed by the equality of the chemical potentials is  $(N_\xi - 1)N_c$ . Thus, the number of free variables therefore:

$$N_F = N_c - N_\xi + 2. \quad (2.30)$$

This relation is known as the *Gibbs' phase rule*.

## 2.2 Phase diagrams

The equilibrium phase diagrams are very useful tools for studying the development of microstructure. A phase diagram contains information derived from the thermodynamic principles described in the previous section, specialized for a particular range of composition. The diagram shows the phases present in equilibrium, and also their stability boundaries in composition and temperature. However it should be noted that thermodynamics identifies only the lowest free energy configuration, the behavior of the real system can be constrained by kinetic processes, such as solute or heat transport. For simplicity, I assume that there is sufficient time for these processes to establish local thermodynamic equilibrium at the solid-liquid interface, or even in the entire system.

Considering only condensed phases at constant pressure (i.e. open to the atmosphere), the Gibbs' phase rule becomes:

$$N_F = N_c - N_\xi + 1. \quad (2.31)$$

In binary systems this means that two phases may co-exist over a range of compositions or temperatures, since  $N_F = 1$  in that case. For three co-existing phases  $N_F = 0$ , so no free variable is left, thus the three phases: the liquid and the two distinct solids occur at a specific composition and temperature, called *invariant point*, and the reaction occurs at this point is the *invariant reaction*. Various types of phase diagrams are classified according to the types of transformations and invariant reactions present, for example:

- eutectic:  $l \rightarrow \alpha + \beta$
- peritectic:  $l + \alpha \rightarrow \beta$
- monotectic:  $l_1 + l_2 \rightarrow \alpha$
- eutectoid:  $\gamma \rightarrow \alpha + \beta$
- peritectoid:  $\gamma + \alpha \rightarrow \beta$

Fig. 2.4 shows a collection of the possible reactions in a binary system.

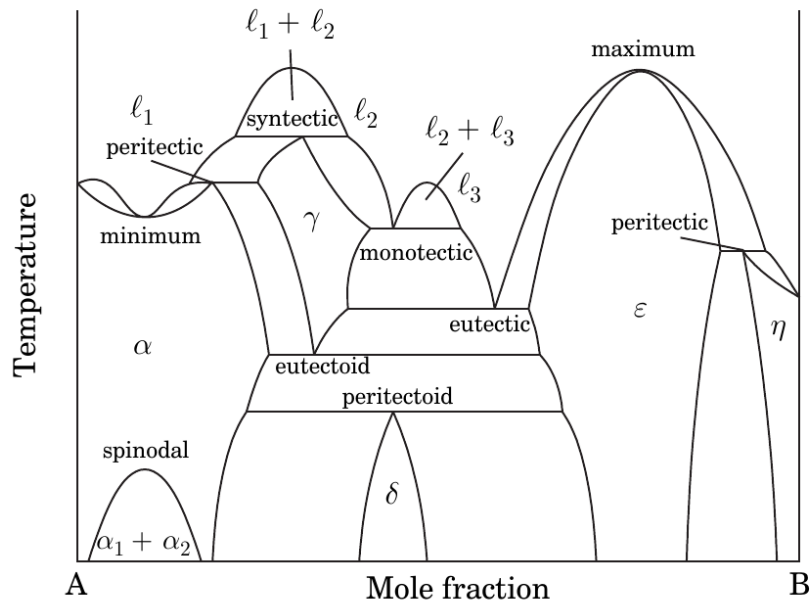


**Figure 2.4.** A hypothetical phase diagram of binary alloy showing some of the possible invariant reactions. [30]

## 2.2.1 Binary eutectic systems

In this section I briefly present a phase diagram for a binary eutectic system. At the invariant point, three phases can co-exist: two solids and one liquid. The second solid phase can appear for several reasons, for example when the two solute elements are not sufficiently similar (e.g. their atomic sizes or crystal structures are dissimilar), then they cannot form a continuous solid solution over the entire composition range.

The equilibrium phase diagram is a direct result of the common tangent construction rule applied to the Gibbs free energy curves of the different phases (shown in Fig. 2.5) that may be present. For simplicity, I approximate the liquid phase with ideal solution model, and the solid phases with regular solution model. The regular solution can be fitted to have a double-well curve,  $G_s^m$  with minima close to those

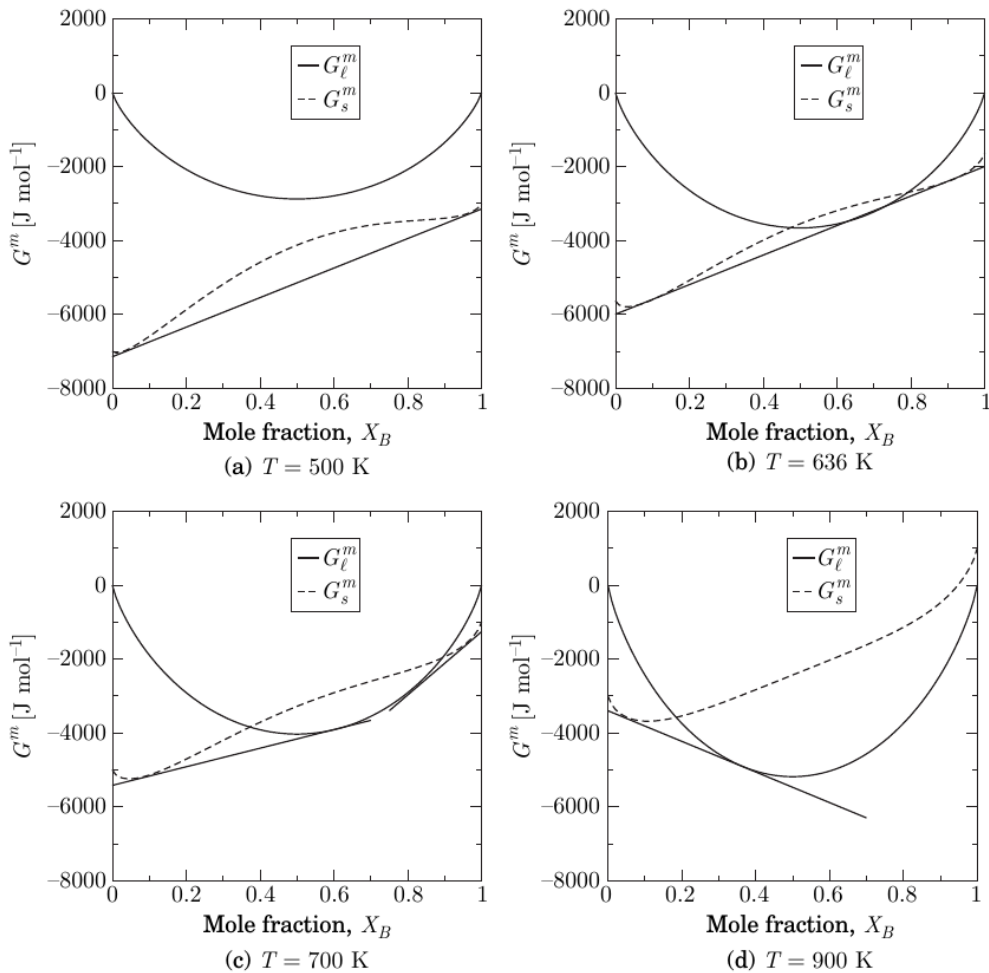


**Figure 2.5.** Gibbs free energy curves for 4 different temperatures for an alloy described by regular solution model. [30]

of the curves  $G_\alpha^m$  and  $G_\beta^m$ . This procedure replaces two distinct solid phases with a single solid  $\alpha$ , that has two minima which will from hereon be denoted  $\alpha_1$  and  $\alpha_2$ . The corresponding equilibrium phase diagram is shown in Fig. 2.6.

At low temperatures, shown in Fig. 2.5 (a), the common tangent indicates the composition of two solids in equilibrium. This results the  $\alpha_1 + \alpha_2$  region in the phase diagram shown in Fig. 2.6. The convex shape of the solid free energy curve is the result of large positive value of  $\Omega_s^m$ . Increasing the temperature, a unique value has been reached, shown in Fig. 2.5 (b), where the common tangent connects three compositions: two solids and one liquid. These three phases are in equilibrium, and according to the Gibbs' phase rule, this assigns an invariant point  $X_{\text{eut}}$ , called *eutectic*, and the corresponding temperature is the *eutectic temperature*,  $T_{\text{eut}}$ . Above  $T_{\text{eut}}$  [Fig. 2.5 (c)], the free energy curves for the solid and the liquid pass through each other, while the convexity of  $G_s^m$  decreases due to the increasing entropy of mixing partially overcoming  $\Omega_s^m$ . At this temperature, there are two sets of common tangents between the liquid and solid, which are corresponds to the regions marked " $l + \alpha_1$ " and " $l + \alpha_2$ " in the phase diagram. As the temperature increases further, as shown in Fig. 2.5 (d), there is only one region of two-phase equilibrium:  $l + \alpha_1$ .

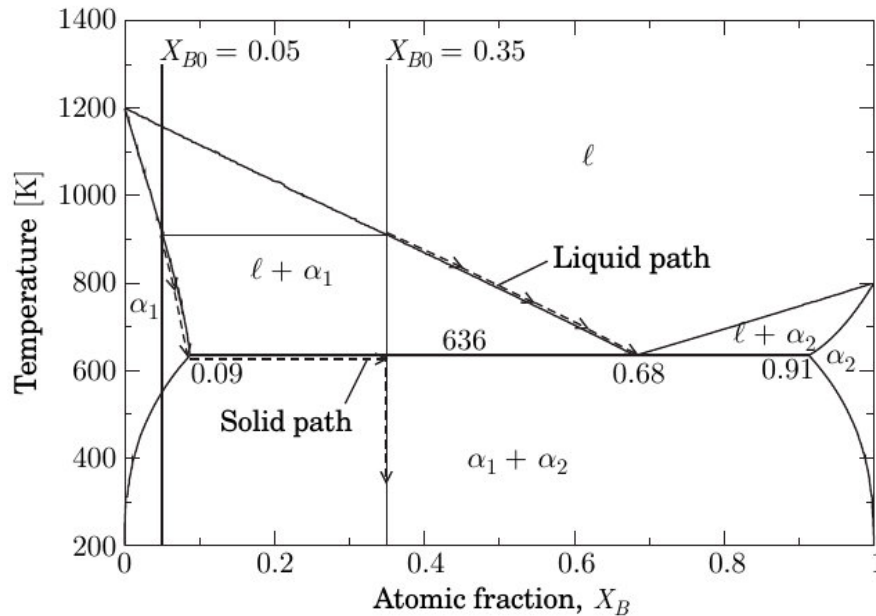


**Figure 2.6.** Binary eutectic phase diagram for a regular solution. A *solidification path*, i.e. the sequence of compositions taken by the solid and liquid phases during solidification (from  $X_{B0}$  composition), is also shown. [30]

The  $T_{\text{liq}}(X_B)$  values define the *liquidus curve*, above which the system is fully

liquid. The  $T_{\alpha_1}(X_B)$  and  $T_{\alpha_2}(X_B)$  defines the *solidus curve* for the solid phases, below which the system is fully solid. The solidus and liquidus curves must meet at the two ends of the diagram, since those points correspond to the melting points of the pure components.

## 2.2.2 Ternary eutectic systems

According to the Gibbs' phase rule, in a three component system when the pressure is fixed, then up to four phases can co-exist at the invariant point, with the invariant reaction  $l \rightarrow \alpha + \beta + \gamma$ . Since  $X_A + X_B + X_C = 1$ , the composition can be represented using a triangle, where the individual components are placed at the vertices of the triangle. In a ternary phase diagram (shown in Fig. 2.7), the temperature is plotted on an axis perpendicular to the composition triangle, thus producing a 3D figure.

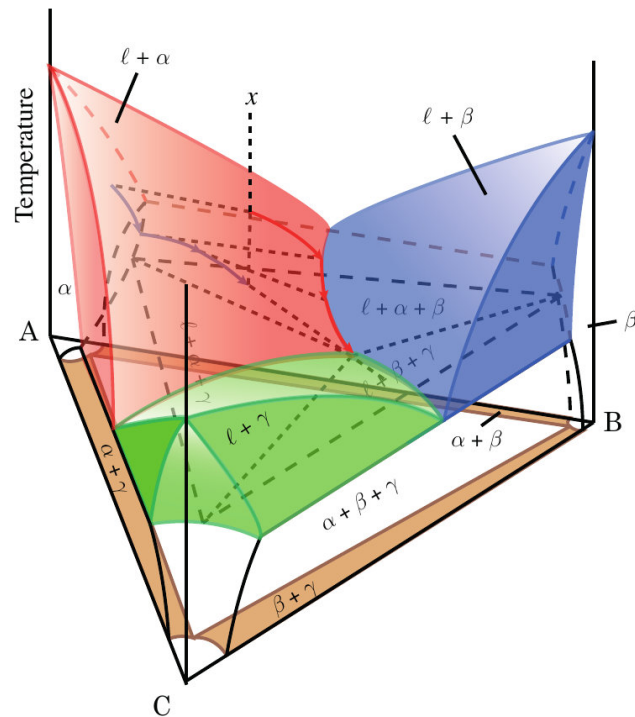


**Figure 2.7.** An isometric view of a ternary eutectic phase diagram. Series of isothermal sections are shown in Fig. 2.8. [30]

The ternary phase diagrams are most easily understood through the use of horizontal (isothermal), and vertical (pseudo-binary) sections. Assume that the melting points of the pure components  $T_f^A$ ,  $T_f^B$  and  $T_f^C$ , the eutectic temperatures in the binary systems  $T_{\text{eut}}^{AB}$ ,  $T_{\text{eut}}^{AC}$  and  $T_{\text{eut}}^{BC}$ , and the temperature of the ternary eutectic reaction,  $T_{\text{eut}}^{ABC}$



are such that  $T_f^A > T_f^B > T_f^C > T_{eut}^{AB} > T_{eut}^{AC} > T_{eut}^{BC} > T_{eut}^{ABC}$ . The series of isothermal sections shown in Fig. 2.8 follow the solidification path of an alloy of composition  $X_0 = (X_{A0}, X_{B0}, X_{C0})$ . Fig. 2.8 (a) shows an isothermal section at a temperature below the melting points of the pure components A and B, but above any of the binary eutectic temperatures or the melting point of pure C component. There are two two-phase regions:  $l + \alpha$  and  $l + \beta$ , and the two solid solution region:  $\alpha$  and  $\beta$  in their respective corners. At this temperature the alloy is completely liquid with composition  $X_0$ . At a temperature below  $T_{eut}^{AB}$ , but still above the eutectic temperatures in the other binary systems [Fig. 2.8 (b)], a three-phase equilibrium ( $l + \alpha + \beta$ ) region ap-

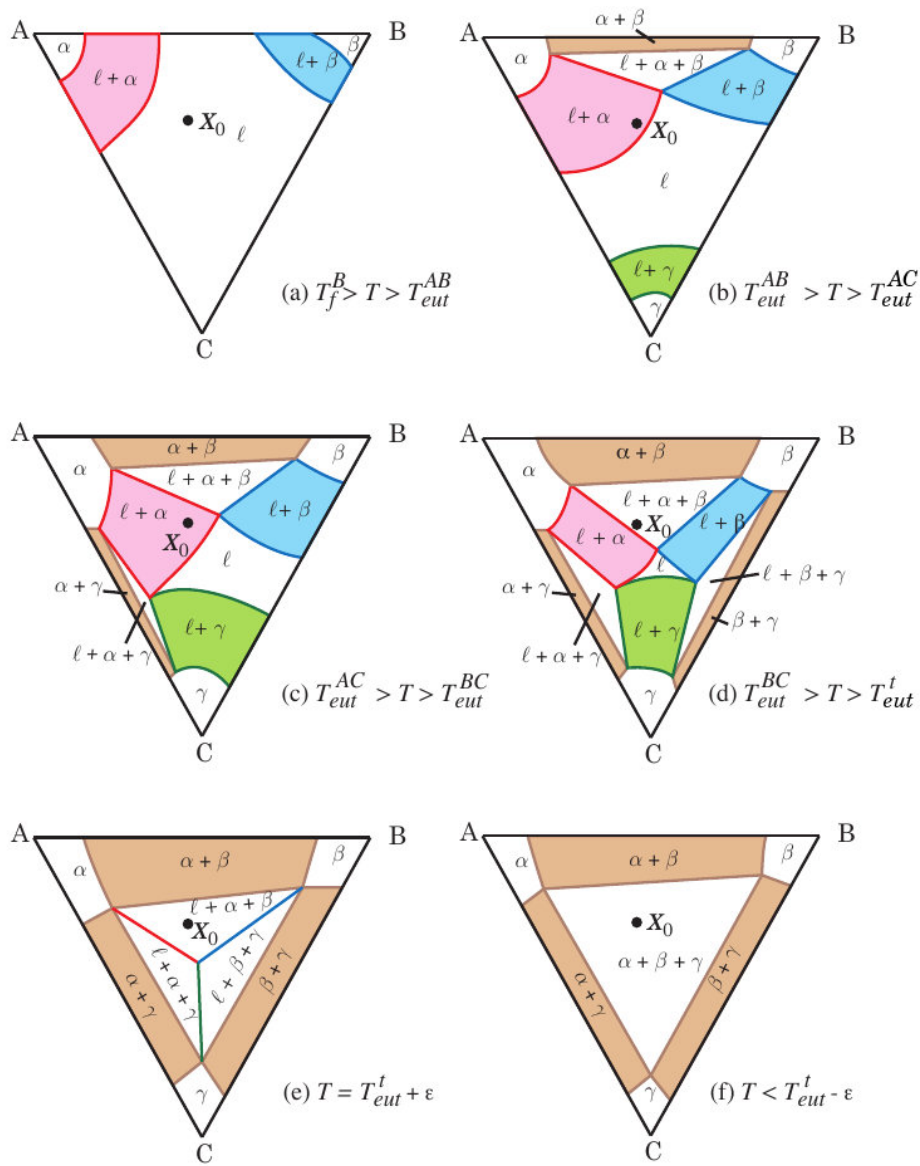


**Figure 2.8.** A series of isothermal sections through the ternary phase diagram shown in Fig. 2.7. [30]

pears as a triangle. The alloy lies within the two-phase  $l + \alpha$  region at this temperature. Fig. 2.8 (c) and (d) illustrate the movement of the phase regions as the temperatures decreases below the other two binary eutectic temperatures, resulting the formation of two additional three-phase equilibrium triangles. The alloy  $X_0$  now lies within the  $l + \alpha + \beta$  three-equilibrium triangle, the compositions of the phases corresponds to those at the vertices of the triangle. In Fig. 2.8 (e), the regions converge at the ternary eutectic temperature  $T_{\text{eut}}^{ABC}$ , where four-phase equilibrium exist:  $l + \alpha + \beta + \gamma$ . Below this temperature [Fig. 2.8 (f)] according to the Gibbs' phase rule, the liquid phase must disappear, and now the alloy  $X_0$  consists of three solid phases.

A pseudobinary section along B-y line is shown in the right panel of Fig. 2.9. The points  $a$  through  $e$  indicate the place where the section intersects a phase boundary. For example the point  $d$  at temperature  $T_{\text{eut}}^{ABC}$  separates two three-equilibrium regions,  $l + \alpha + \beta$  and  $l + \alpha + \gamma$ .

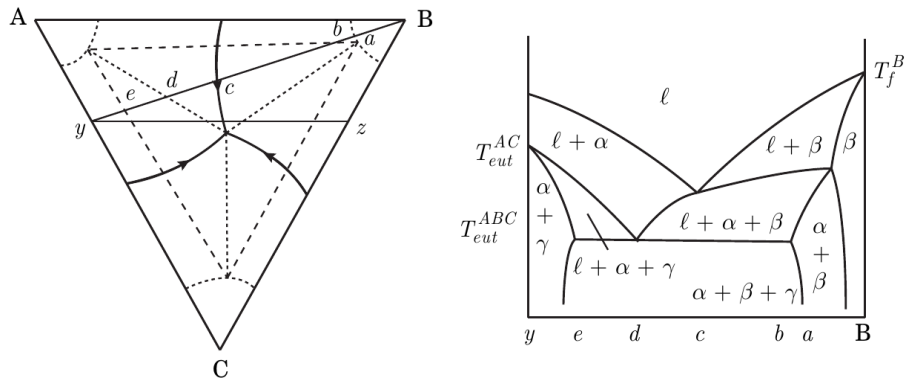


**Figure 2.9.** The projection of the ternary phase diagram onto the composition triangle (left), and the vertical section B-y (right). [30]

## 2.3 Microstructure

### 2.3.1 Excess energy of a curved interface

Considering a single component system at equilibrium, the atoms or molecules at the solid-liquid interface do not have the same molar Gibbs free energy as those in either the solid or the liquid. They have an excess energy because of the slight structural changes on both sides. The integral of this excess free energy over the thickness of the

interface, multiplied by some form of molar volume ( $V^m$ ), is the solid-liquid interfacial energy,  $\gamma_{\text{SL}}$  having units of  $\text{Jm}^{-2}$  (see Fig. 2.10). In general, since the solid phase is crystalline, the surface energy will be anisotropic.

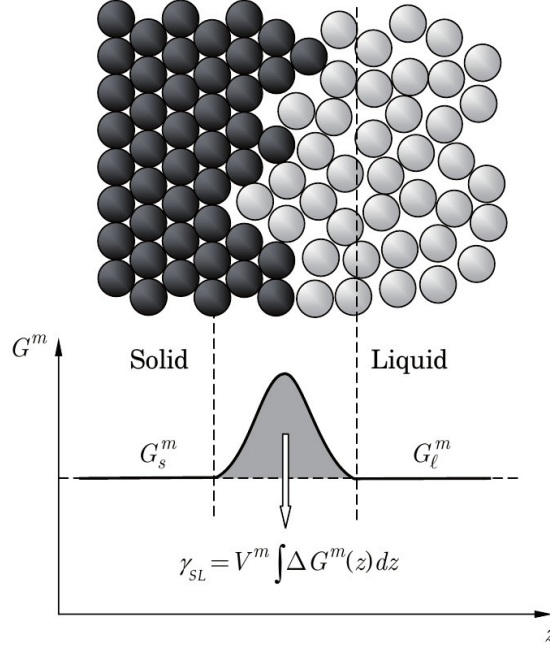


**Figure 2.10.** Interfacial energy as the excess Gibbs free energy of atoms located within a diffuse solid-liquid interface. [30]

The total Gibbs free energy of the system can be expressed as:

$$G = G_l^m n_l + G_s^m n_s + A_{\text{SL}} \gamma_{\text{SL}}, \quad (2.32)$$

where  $n_l$  and  $n_s$  are the number of moles in the liquid and solid, respectively, and  $A_{\text{SL}}$  is the interfacial area between the liquid and the solid of  $V_s$  volume. The condition for equilibrium between the liquid and a solid particle of *mean curvature*,  $\bar{\kappa}$ :

$$G_l^m = G_s^m + 2V_s^m \bar{\kappa} \gamma_{\text{SL}}, \quad (2.33)$$

where the mean curvature can be written as:

$$\bar{\kappa} = \frac{1}{2} \frac{\partial A_{\text{SL}}}{\partial V_s}. \quad (2.34)$$

The melting point of a positively curved (convex) solid,  $T_f^R$ , is lower than that of the

planar solid,  $T_f$ . The decrease of the melting point associated with curvature is called the *curvature undercooling*, and can be expressed as:

$$\Delta T_R = T_f - T_f^R = 2\bar{\kappa} \frac{\gamma_{\text{SL}} V^m}{\Delta S_f^m} = 2\Gamma_{\text{SL}} \bar{\kappa}, \quad (2.35)$$

where  $\Delta S_f^m = L_f^m/T_f$  is the *entropy of fusion*,  $L_f^m$  is the *latent heat of fusion* per mole and  $\Gamma_{\text{SL}}$  is the *Gibbs-Thomson coefficient*, given by:

$$\Gamma_{\text{SL}} = \frac{\gamma_{\text{SL}} V^m}{\Delta S_f^m} = \frac{\gamma_{\text{SL}} T_f}{\rho_s L_f}, \quad (2.36)$$

where  $\rho_s$  is the density of the solid and  $L_f$  is the bulk latent heat. The expression that gives the melting point for the pure material with curved surface is called the *Gibbs-Thomson equation*:

$$T_f^R = T_f - 2\Gamma_{\text{SL}} \bar{\kappa}. \quad (2.37)$$

### 2.3.2 Dendritic growth

As the solid, e.g. a sphere or a flat front grows, the initial morphology eventually becomes unstable, which leads to the formation of *cells* and/or *dendrites*. The subject can be divided into a discussion of free growth, the evolution of one isolated solid particle in an undercooled melt, and a discussion of *constrained growth*, where many solid structures grow at the same time under an imposed thermal gradient.

#### Free growth

Starting with free growth, considering pure melt with a spherical solid nucleus of radius greater than the critical radius  $R_c = 2\Gamma_{\text{SL}}/\Delta T$ , where  $\Delta T$  is the undercooling. The critical radius,  $R_c$  is known from classical nucleation theory, it is energetically favorable for the sphere to continue to grow as soon as its radius is greater than the critical value. However, the particle cannot grow indefinitely, because the spherical morphology becomes unstable with respect to perturbations in shape. Once these disturbances to the spherical shape can grow, the solid shape begins to express the preferred growth directions of the underlying crystal. This preference is derived from anisotropy.

Fig. 2.11 shows an optical image of succinonitrile (SCN) crystal growing in an

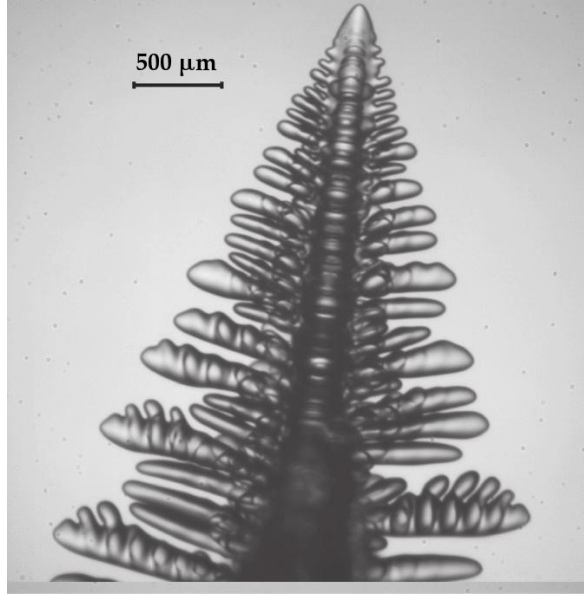


**Figure 2.11.** Succinonitrile dendrite for  $\Delta T = 0.2K$  undercooling. [31]

undercooled melt. This alloy is often used in solidification experiments, because it crystallizes with BCC structure, it is transparent and behaves similarly to metals. The solid takes on a tree-like structure, called dendrite, consisting of a primary trunk growing along one of the six equivalent  $\langle 100 \rangle$  direction of the crystal, with secondary arms in the four conjugate  $\langle 100 \rangle$  directions appearing behind the dendrite tip. The  $\langle 100 \rangle$  preferred growth direction is typical of BCC crystals and reflects the underlying surface energy anisotropy.

In most metallic systems the fact that the solid grows along preferred crystallographic directions can be understood as an attempt by the system to minimize the area of those surfaces with the highest interfacial energy. Thus, as the anisotropy of the interfacial energy  $\gamma_{SL}$  increases, assuming that all other quantities remain the same, the dendrite will exhibit a sharper tip. If the anisotropy of  $\gamma_{SL}$  is large enough, the dendrites will present a *faceted* morphology. As two examples of this morphology, Fig. 2.12 (a) shows a crystal of pure bismuth grown from an undercooled melt, and Fig. 2.12 (b) displays an array of faceted Si dendrites growing during directional solidification in a Si-Al alloy.

One can examine in more detail the evolution of the shape using linear stability analysis. In this method, small perturbations are introduced to the base state of the system, and the governing equations are used to determine whether the disturbance

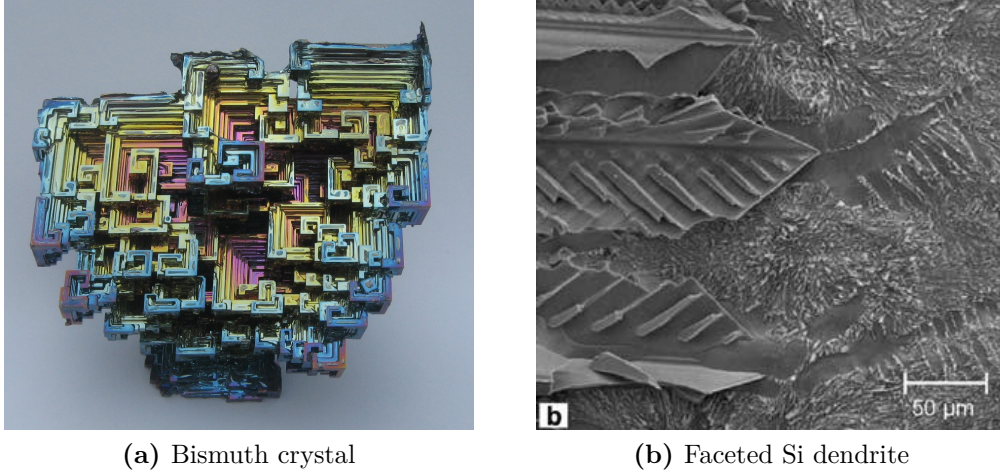


**Figure 2.12.** Examples of faceted morphologies. (a) A photograph of bismuth crystal grown from a grain inserted into an undercooled melt. Source: [bismuthcrystal.com](http://bismuthcrystal.com). (b) A micrograph of a quenched interface in directionally solidified Si-Al alloy [32].

will decay or grow in time. If the disturbance decays in time, the base state is said to be stable, conversely, if the perturbation grows in time, the base state is called unstable. The linear stability of a spherical particle was first examined by Mullins and Sekerka [33], who introduced small, non-symmetric perturbations on the surface using spherical harmonics. The criterion for instability of harmonic mode  $n = 2$  is:

$$R^* > (4k_T + 7)R_c, \quad (2.38)$$

where  $k_T = k_s/k_l$  is the thermal conductivity ratio and  $R^*$  is the size of the sphere, above which it becomes morphologically unstable and the perturbation starts to grow. The estimation of the wavelength of the instability is the following:

$$\lambda \approx 4.5\pi\sqrt{d_0(\alpha_l/v^*)}, \quad (2.39)$$

where  $d_0 = c_{pl}\Gamma_{SL}/L_f$  is the *thermal capillary length*,  $c_{pl}$  is the specific heat of the liquid at constant pressure and  $\alpha_l/v^*$  term is the ratio of the thermal diffusivity to the interface velocity. This equation relates the wavelength of the disturbance to the geometric mean of two length scales: the capillary length  $d_0$  and the characteristic length scale for the diffusion field ahead of the moving interface,  $\alpha_l/v^*$ .

The stability analysis can be adapted to solidification of a binary metallic alloy.

The disparity in diffusivities,

$$D_s \ll D_l \ll \alpha_l \leq \alpha_s, \quad (2.40)$$

where  $D_s$  and  $D_l$  are the diffusion coefficients for the solid and the liquid, respectively, means large separation in length and time scales for the head and solute transport, thus the binary melt can be considered isothermal. The alloy spherical particle becomes unstable for:

$$R^* > \left(3 \frac{D_s}{D_l}\right) R_c. \quad (2.41)$$

And the wavelength is:

$$\lambda \approx 3.5\pi \sqrt{d_0^C (D_l/v^*)}, \quad (2.42)$$

where  $d_0^C$  is the *chemical capillary length*, defined by:

$$d_0^C = -\Gamma_{SL}/(m_l C_l^{\text{eq}}(1 - k_0)), \quad (2.43)$$

where  $m_l$  is the steepness of the liquidus line,  $C_l^{\text{eq}}$  is the equilibrium composition and  $k_0$  is the partition coefficient [see Eq. (2.28)].

The stability analysis of a spherical particle yields the result, that the length scale for the instability is proportional to the geometric mean of the length scales associated with capillarity ( $d_0$  or  $d_0^C$ ) and diffusion ( $\alpha/v^*$  or  $D_l/v^*$ ). The wavelength is selected by a competition between surface energy and diffusion.

### Constrained growth

At constrained growth there is a temperature gradient,  $G_l^*$  ahead of the interface, which will control the growth rate of the solid. The temperature gradient is traveling with  $v_p$  pulling speed by e.g. moving the mold over a heater.

Fig. 2.13 shows a transition from planar interface to dendrites as the pulling velocity increases in a thin sample of succinonitrile-salol alloy. At very low pulling velocities the solidification front is planar (not shown). Above a critical velocity, shallow *cells* develop, separated by grooves parallel to the temperature gradient,  $G_l$ . As the velocity increases, the grooves between the cells become deeper and the cell spacing increases.

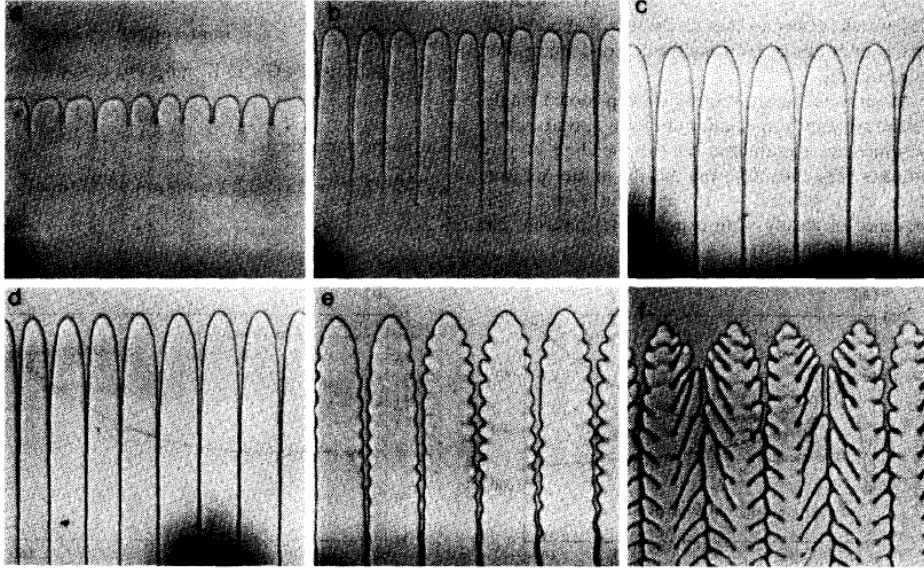


**Figure 2.13.** Microstructures observed in an succinonitrile–0.66wt% salol alloy, directionally solidified with 4.5 K/mm temperature gradient. The pulling speeds from (a) to (f) are: 0.57, 0.95, 2.0, 4.1, 5.7 and 7.6  $\mu\text{m/s}$ . [34]

In Fig. 2.13 (e) perturbations start to appear along the sides of the cells, then at an even higher velocity, the cells eventually transform into dendrites with sidebranches [panel (f)]. These dendrites have much sharper tips than the cells.

The conditions for stability of a solid-liquid interface can also be calculated. Consider a planar front directional solidification of a binary alloy at constant speed,  $v_p$ , in a constant temperature gradient,  $G > 0$ . In this case, the pulling speed and interface speed are the same (i.e.  $v_p = v^*$ ). Fig. 2.14 shows the temperature and composition environment near the solid-liquid interface. Depending on the conditions of the growth, a *supercooled region* may appear near the interface, where the actual temperature is lower than the liquidus temperature. In that region any perturbation will continue to grow and the planar interface becomes unstable. The stability condition is the following:

$$\frac{G}{v_p} \geq \frac{\Delta T_0}{D_l}, \quad (2.44)$$

where  $\Delta T_0 = T_{\text{liq}} - T_{\text{sol}}$  is the nominal freezing range of the alloy, the difference of the liquidus- and solidus (interface) temperatures.



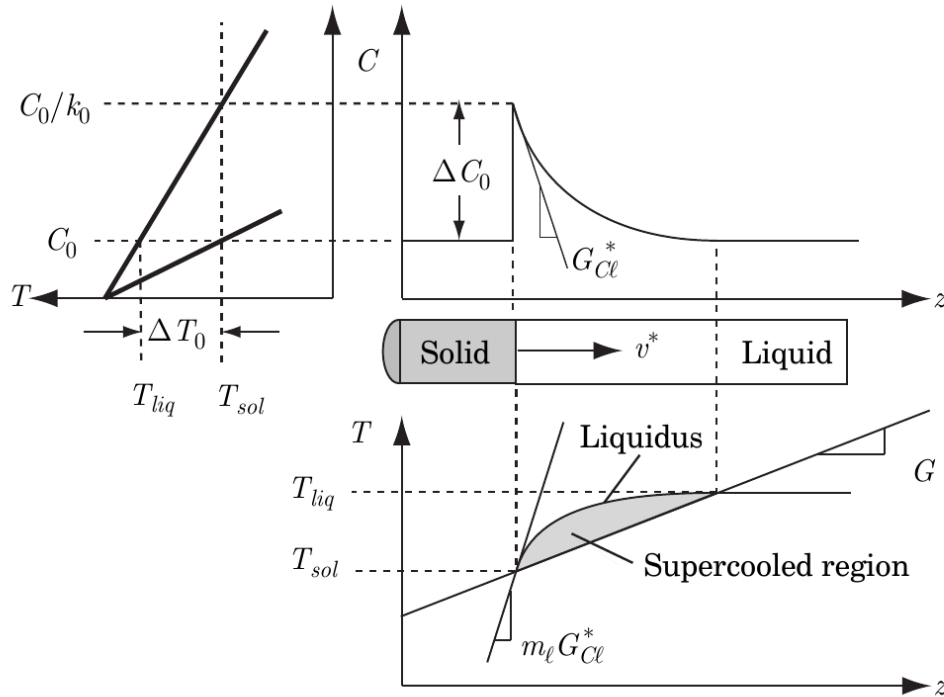


**Figure 2.14.** Illustration of the constitutional undercooling criterion for stability of a planar interface for a binary alloy under steady-state directional solidification at constant velocity ( $v^*$ ). In the supercooled region any perturbation will continue to grow and the planar interface becomes unstable. The front grows in the positive  $z$  direction,  $C$  is the composition,  $C_0$  is the nominal composition of the alloy,  $m_l$  is the slope of liquidus,  $G_{Cl}^*$  is the composition gradient at the interface,  $G$  is the temperature gradient,  $k_0$  is the partition coefficient. [30]

### 2.3.3 Eutectics

As a single phase,  $\alpha$  solidification proceeds, the liquid becomes richer in solute (if  $k_0 < 1$ ), and at some point, its composition reaches an invariant point, e.g. a eutectic one. In order for the invariant reaction to proceed, a second solid phase,  $\beta$  must nucleate and grow concurrently with or expense of the  $\alpha$  phase. During eutectic growth, the exchange of solute between the two solid phases occurs via transport in the liquid phase. Since the  $\alpha$  solid phase rejects solute B, whereas the  $\beta$ -phase rejects A, the coupling of  $\alpha$  and  $\beta$ , illustrated in Fig. 2.15, allows a lateral diffusion in the liquid. This mode is called *coupled growth*, which results in a small maximum and minimum compositions ahead of the two solid phases. The speed of the lateral diffusion increases as the lamellar spacing (the eutectic wavelength),  $\lambda$  decreases. In contrast, the capillarity (due to surface tension) is inversely proportional to  $\lambda$ . The actual eutectic wavelength

is determined by a balance between transport and surface tension (see Section 2.3.5), similarly to what was found for dendritic growth [Eq. (2.39)].

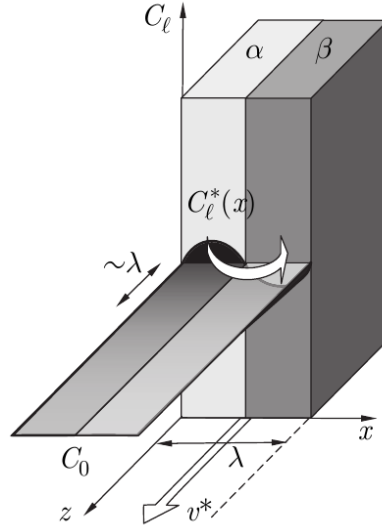


**Figure 2.15.** Schematic diagram showing the steady-state solute field ahead of two lamellae  $\alpha$  and  $\beta$  during coupled growth. The front grows in the positive  $z$  direction with  $v^*$  velocity,  $\lambda$  is the eutectic wavelength,  $C_0$  is the nominal composition of the alloy. [30]

### Coupled eutectic growth morphologies

Different morphologies can be observed for coupled growth depending on the volume fractions of the two phases and whether the phases are faceted or not. When both phases are faceted, they grow along well-defined direction, and cannot maintain steady triple junction. Therefore, no coupled growth is possible in this case.

In *irregular eutectics* one of the two phases grows with a non-faceted morphology while the other phases are faceted. Triple junctions can be maintained: the non-faceted phase follows the needles or plates of the faceted phase. The resulting eutectic structure is complex and irregular as sketched schematically on the right-hand side of Fig. 2.16. In *regular eutectics* both phases are non-faceted, triple junctions can be maintained in almost any growth direction. Rod-like and lamellar morphologies are shown on the left-hand side of Fig. 2.16.

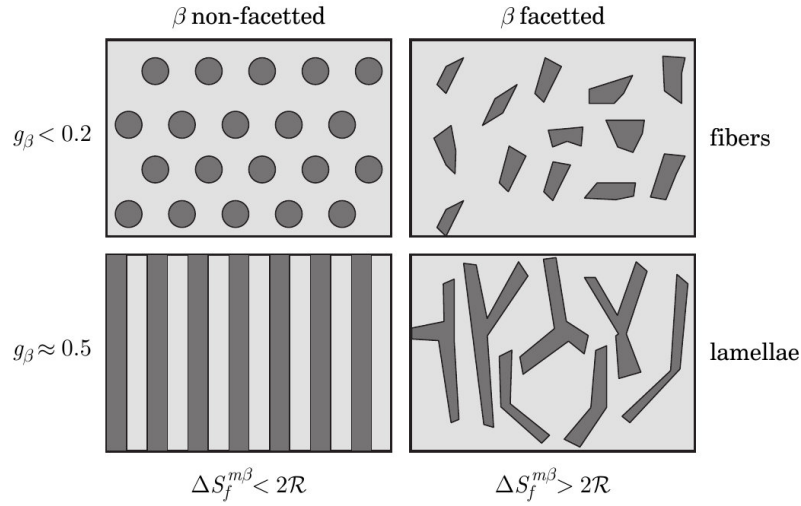


**Figure 2.16.** Eutectic interface morphologies for two volume fractions of the  $\beta$ -phase when the  $\alpha$ -phase is non-faceted and the  $\beta$ -phase is either non-faceted (left column) or faceted (right column). [30]

### 2.3.4 Spiral two-phase dendrites

In ternary alloys more exotic solidification patterns may appear, like the spiral two-phase dendrites during univariant directional solidification [16]. Two different crystal phases grow from the apex of a parabolic finger, forming a spiral pattern, which leaves behind a double helix microstructure in the solid. Fig. 2.17 shows an optical image of

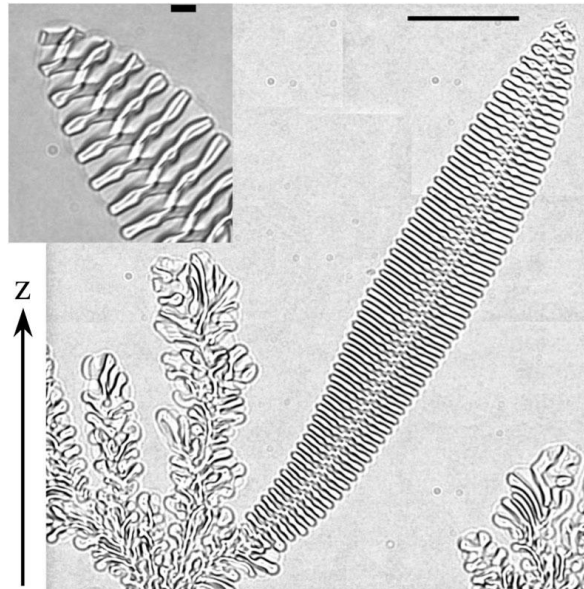


**Figure 2.17.** A spiral two-phase dendrite in process of overgrowing a two-phase branched structure during directional solidification. Bar:  $100\ \mu\text{m}$ ,  $\mathbf{z}$ : direction of the thermal gradient. Inset: Tip of a steady-state dendrite.  $v_p = 0.1\ \mu\text{m s}^{-1}$ . Bar:  $10\ \mu\text{m}$ . [16]

a spiral two-phase dendrite. In the experiment a transparent, pseudo-ternary-eutectic, succinonitrile-based alloy, called SCN-DC-NA [35], was used, under such conditions that the solid is a composite of two crystal phases, namely, SCN-rich  $\alpha$  and DC-rich  $\beta$  phases. The optical contrast is small between  $\alpha$  and the liquid, and large between  $\beta$  and the other two phases.

During the growth of a two-phase solid from a ternary melt, two components of the alloy combine to form the eutectic microstructure. Meanwhile, the third one (the “ternary” component) is rejected into the liquid which generates the Mullins-Sekerka dynamics, i.e. destabilizing the planar eutectic growth front if the pulling speed is high enough. The tip radius,  $R_{\text{tip}}$  is close to the Jackson-Hunt scaling length (see next section):  $\lambda_{\text{JH}} = \sqrt{K_{\text{JH}} v_p^{-1/2}}$ , where  $K_{\text{JH}}$  is a material constant and  $v_p$  is the pulling speed. A full cycle of the spiraling growth can be seen in Fig. 2.18. Both left- and right-handed spirals were observed, despite the chirality of the DC molecules.

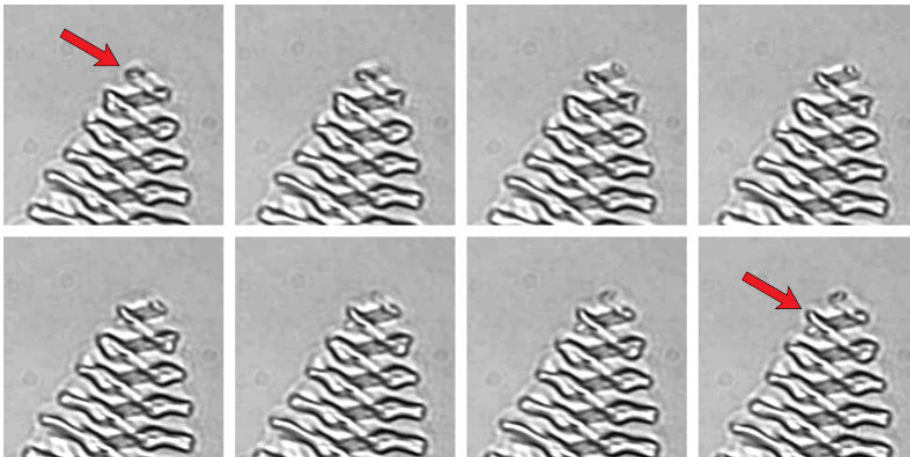


**Figure 2.18.** Snapshots extracted from a video of a thin sample showing a full spiraling cycle. The red arrows point to the same location before and after the spiraling cycle. Source: unpublished video of Silvère Akamatsu.

### 2.3.5 Jackson–Hunt theory for lamellar eutectic growth

The growth of lamellar eutectics has been studied theoretically and experimentally long ago. Zener predicted [36] that the product of the growth velocity,  $v$ , and square of the lamellar wavelength,  $\lambda$ , should be constant:  $\lambda^2 v = \text{const}$ . Several experiments confirmed this relation for lamellar growth [37] (and also for rod eutectics). These modes of growth depend on the interplay between the diffusion required for phase

separation and the formation of phase boundaries. Jackson and Hunt presented an analysis of these factors [38]. Considering a periodic flat lamellar front of  $\alpha$  and  $\beta$  phases with  $\lambda$  characteristic spacing and solving the diffusion equations, the average undercooling of the eutectic front is:

$$\Delta T = A_C \frac{v\lambda}{D_l} + \frac{A_R}{\lambda} \quad (2.45)$$

with

$$\begin{aligned} A_C &= \frac{\Delta C_0}{g_\alpha g_\beta} \frac{|m_{l\alpha}| |m_{l\beta}|}{|m_{l\alpha}| + |m_{l\beta}|} \sum_{n=1}^{\infty} \frac{\sin^2(n\pi g_\alpha)}{(n\pi)^3} \\ A_R &= \frac{|m_{l\alpha}| |m_{l\beta}|}{|m_{l\alpha}| + |m_{l\beta}|} \left( \frac{2\Gamma_{\alpha l} \cos(\theta_\alpha)}{|m_{l\alpha}| g_\alpha} + \frac{2\Gamma_{\beta l} \cos(\theta_\beta)}{|m_{l\beta}| g_\beta} \right), \end{aligned} \quad (2.46)$$

where  $D_l$  is the diffusion coefficient of the liquid,  $\Delta C_0 = [(1 - k_{0\beta}) + (k_{0\beta} - k_{0\alpha})C_{\text{eut}}]$ ,  $C_{\text{eut}}$  is the concentration at the eutectic point,  $g_{\alpha|\beta}$  is the volume fraction,  $m_{l\alpha|\beta}$  is the slope of liquidus curve and  $\theta_{\alpha|\beta}$  is the contact angle for  $\alpha$  and  $\beta$  phases.

The expression for the undercooling for the eutectic front Eq. (2.45) shows the contributions of diffusion and capillarity. The diffusion contribution [first term in the RHS of Eq. (2.45)] increases with eutectic spacing  $\lambda$  and velocity  $v$ , while the capillarity [second term in the RHS of Eq. (2.45)] is inversely proportional to  $\lambda$ . For any given velocity, the undercooling has a minimum value at particular spacing,  $\lambda_{\text{ext}}$ :

$$\lambda_{\text{ext}} = \sqrt{\frac{A_R D_l}{A_C v}}, \quad (2.47)$$

which is the geometric mean of two length scales:  $A_R/A_C$  is essentially a weighted average capillary length, whereas  $D_l/v$  is the thickness of the boundary layer ahead of a steady-state planar front. Thus the lamellae spacing, growth rate, and undercooling at the extremum relate via the following expressions:

$$\lambda_{\text{ext}}^2 v = \frac{A_R}{A_C} D_l \quad \text{and} \quad \Delta T = 2\sqrt{\frac{A_R A_C}{D_l}} \sqrt{v}. \quad (2.48)$$

It is concluded from stability analysis that the stable growth occurs at or near the minimum interface undercooling for a given growth rate. The lamellar spacing at the

minimum undercooling is called the Jackson-Hunt wavelength:  $\lambda_{\text{JH}}$ , and the

$$\lambda^2 v = \text{const.} \quad (2.49)$$

expression is referred as the Jackson-Hunt scaling rule.

## 2.4 The Phase-Field Method

The phase-field method is a versatile technique for simulating microstructure evolution at the mesoscale. It is widely used for describing different phenomena, such as solidification [39], solid-state phase transformations [40, 41], grain-growth [42], coarsening [43], dislocation dynamics [44], crack propagation [45], electromigration [46], solid-state sintering [47], and even vesicle membranes in biological applications [48].

The phase-field theory is a direct descendant of the Ginzburg-Landau/Cahn-Hilliard type classical field theory approaches [49, 50] to phase boundaries. Its origin can be traced back to a model of Langer [51], Collins & Herbert [52], and Caginalp & Fife [53].

### 2.4.1 Field variables of the Phase-Field Method

In the phase-field method, the microstructural evolution is analyzed by means of a set of field variables, or *order parameters* that are continuous functions of time and spatial coordinates. A distinction can be made between variables related to a conserved quantity and those related to a non-conserved quantity.

The most important one is the non-conserved phase field  $\phi$ , which characterizes the local phase state of the matter. In the simplest case,  $\phi = 0$  in bulk liquid phase and  $\phi = 1$  in the bulk solid phase, interpolating between these values in a narrow interface region. An important advantage of the phase-field method is that, thanks to the diffuse interface description, there is no need to track the interfaces during the microstructural evolution. The location of the interface can be obtained from the numerical solution for the phase-field variable by finding the positions, where  $\phi = 0.5$ . In most cases, in addition to the phase field, other fields, such as the concentration in two- or multi-component systems are required. The concentration variable,  $c \in [0, 1]$ ,

is a conserved order parameter, since the number of moles of each component in the system is constant.

## 2.4.2 Free energy functional

The total free energy of the system in the phase-field method is formulated as a functional of the set of chosen field variables and their gradients. For a binary, two-phase (solid and liquid) system the free energy functional,  $F$ , is:

$$F = \int_V \left[ \frac{\epsilon_\phi^2}{2} (\nabla\phi)^2 + \frac{\epsilon_c^2}{2} (\nabla c)^2 + f_0(\phi, c, T) \right] dV, \quad (2.50)$$

where  $\epsilon_\phi$  and  $\epsilon_c$  are gradient energy coefficients and  $f_0(\phi, c, T)$  is the classical homogeneous free energy density. The gradient terms are responsible for the diffuse character of the interfaces. The gradient energy coefficients are related to the interfacial energy and interface thickness. They are always positive, so that gradients in the system are energetically unfavorable.

The homogeneous free energy density consist of an interpolation function  $f(\phi, c, T)$  and a double-well function  $wg(\phi)$ :

$$f_0(\phi, c, T) = f(\phi, c, T) + wg(\phi). \quad (2.51)$$

The double-well potential  $g(\phi)$ :

$$g(\phi) = \phi^2(1 - \phi)^2 \quad (2.52)$$

has minima at  $\phi = 0$  and  $1$  and  $w$  is the depth of the energy well [see Fig. 2.19 (b)]. The parameter  $w$  is either a constant [54] or depends linearly on the molar fraction of the components [55], or the temperature. The interpolation function,  $f(\phi, c, T)$ , combines the free energy expressions of the coexisting phases,  $f_l$  and  $f_s$  into one expression using the  $p(\phi)$  weight function:

$$f(\phi, c, T) = [1 - p(\phi)]f_l(c, T) + p(\phi)f_s(c, T), \quad (2.53)$$

where  $p(\phi)$  is a smooth function that equals 1 for  $\phi = 1$  and 0 for  $\phi = 0$  and also has local extrema at these values [see Fig. 2.19 (a)]. One common choice for  $p(\phi)$  is the following:

$$p(\phi) = \phi^3(10 - 15\phi + 6\phi^2). \quad (2.54)$$

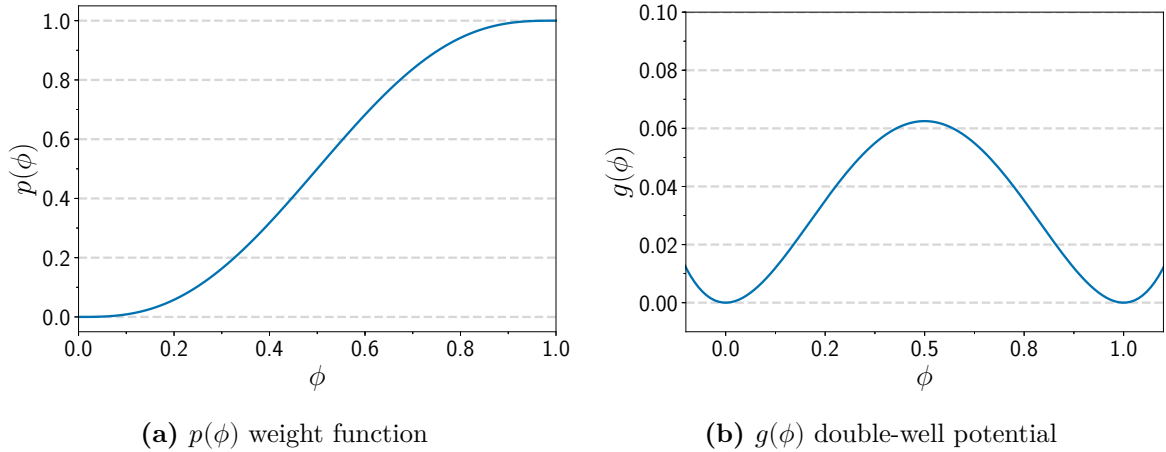


**Figure 2.19.** The weight function  $p(\phi)$  [Eq. (2.54)] and the double-well potential  $g(\phi)$  [Eq. (2.52)] used to construct the homogeneous free energy density.

### 2.4.3 Equations of motion

The time evolution of the field variables is given by a set of coupled partial differential equations, one for each variable. The equations are chosen in a way that the free energy decreases monotonically and mass is conserved for all components. The equation of motion for non-conserved fields (such as the phase field) is called the Allen-Cahn equation [56]:

$$\frac{\partial \phi}{\partial t} = -M_\phi \frac{\delta F}{\delta \phi} + \xi, \quad (2.55)$$

where the parameter  $M_\phi$  is a positive mobility that may depend on the local values of the field variables to introduce anisotropy,  $\delta$  denotes the functional derivative and  $\xi$  is a non-conserved Gaussian noise term with an amplitude determined by the fluctuation-dissipation theorem [57].

For conserved fields (such as the concentration) the evolution equation is called the



Cahn-Hilliard equation [50]:

$$\frac{\partial c}{\partial t} = \nabla \cdot \left[ M_c \nabla \frac{\delta F}{\delta c} \right] + \xi_c, \quad (2.56)$$

where the parameter  $M_c$  is a positive mobility related to the solute diffusional coefficient, and  $\xi_c$  is a conservative Gaussian flux-noise term to model the concentration fluctuations.



# Chapter 3

## Model description

In our work we used a simple ternary phase-field model, which can be obtained as a straightforward generalization of the phase-field model of binary solidification [58, 59] introduced in the previous chapter. The ternary model is solved in a dimensionless form; accordingly, the size scale is determined by the interface thickness chosen for redimensionalizing the results. Considering that the physical interface thickness is about 1-2 nm, the present results refer to nano-scale eutectic structures, expected to form at high undercoolings.

### 3.1 Free energy functional

The free energy functional has been obtained as a simple ternary generalization of the standard binary phase-field model:

$$F[\phi, \mathbf{c}] = \int \left[ \frac{\epsilon_\phi^2}{2} (\nabla \phi)^2 + wg(\phi) + [1 - p(\phi)] f_l(\mathbf{c}) + p(\phi) \left( f_s(\mathbf{c}) + \frac{\epsilon_c^2}{2} \sum_{i=1}^3 (\nabla c_i)^2 \right) \right] dV. \quad (3.1)$$

Here  $\phi(\vec{r}, t) \in [0, 1]$  is the phase field, which is defined 0 for bulk liquid and 1 for bulk solid phase,  $\mathbf{c} = (c_1, c_2, c_3)$  are the three concentration fields,  $g(\phi) = \phi^2(1 - \phi)^2/4$  is the quartic function which ensures the double-well form of  $F$ , and the  $p(\phi) = \phi^3(10 - 15\phi + 6\phi^2)$  function interpolates between the free energy densities of the solid and

liquid phases. For the liquid phase, ideal solution model was used [Fig. 3.1 (a)-(b)]:

$$f_l(\mathbf{c}) = \sum_{i=1}^3 c_i [f_i^l + \log c_i]. \quad (3.2)$$

For the solid phases, regular solution model was used [Fig. 3.1 (c)-(d)]:

$$f_s(\mathbf{c}) = \sum_{i=1}^3 c_i [f_i^s + \log c_i] + \frac{1}{2} \sum_{i \neq j} \Omega_{ij} c_i c_j. \quad (3.3)$$

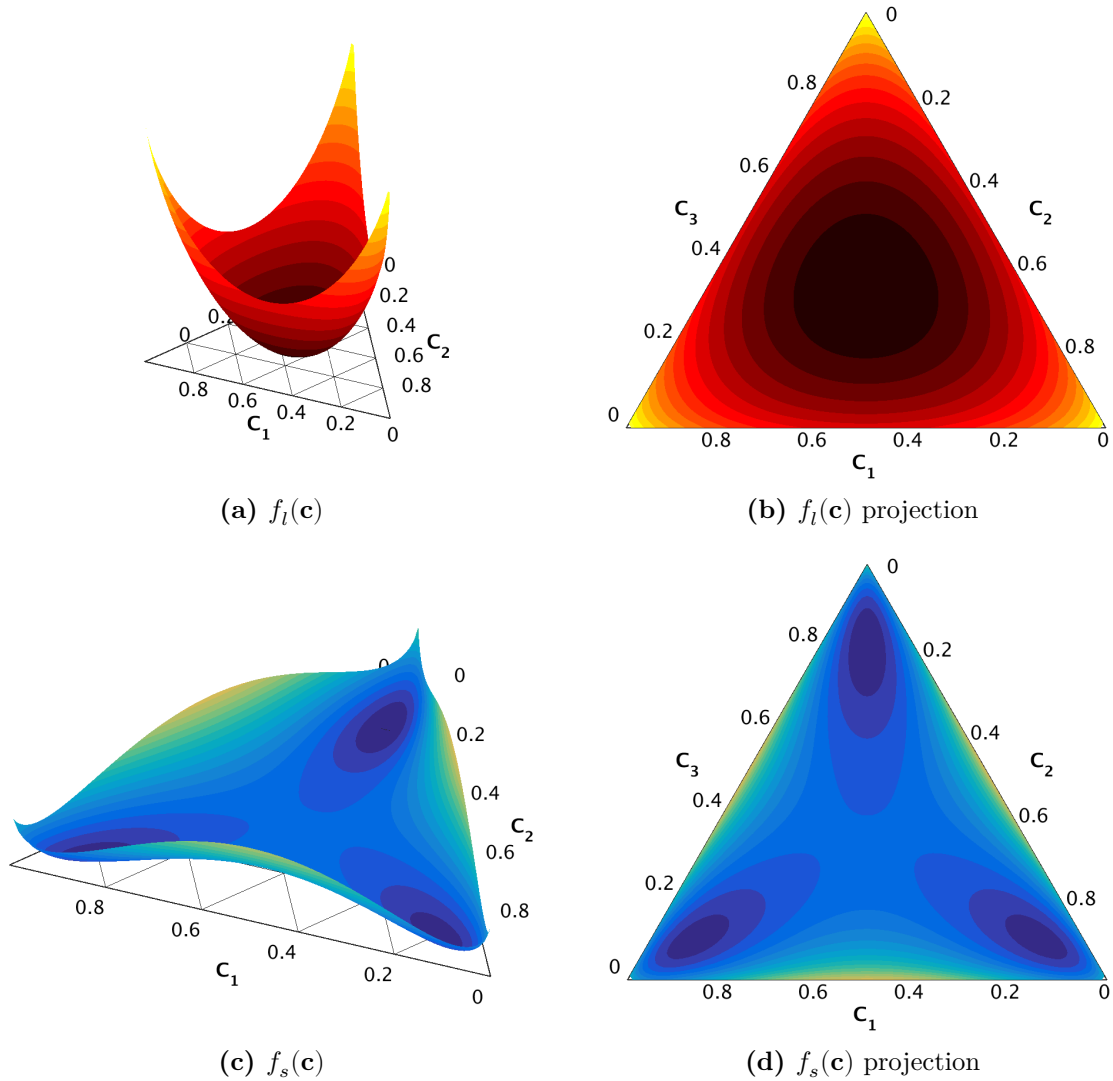


**Figure 3.1.** The free energy functions displayed above the Gibbs-simplex (concentration triangle). (a)-(b) Liquid phase:  $f_l(\mathbf{c})$  [Eq. (3.2)]. (c)-(d) Solid phases:  $f_s(\mathbf{c})$  [Eq. (3.3)].

In the case of a single component phase-field model, the interface thickness ( $\delta$ )

and the solid-liquid interface free energy ( $\gamma_{\text{SL}}$ ) has an analytical form, which can be obtained by solving the 1D Euler-Lagrange equation for the equilibrium planar interface ( $\delta F/\delta\phi = 0$ ):

$$\delta = \frac{1}{6} \sqrt{\frac{\epsilon_\phi^2 w}{2}} \quad \text{and} \quad \gamma_{\text{SL}} = 4 \ln 3 \sqrt{\frac{2\epsilon_\phi^2}{w}}. \quad (3.4)$$

However, when the concentration has been also incorporated in the model, the interface free energy no longer has a simple, analytical form. The total solid-liquid interface free energy can be written as:  $\gamma_{\text{SL}} = \gamma_{\text{SL},0} + \gamma_{\text{SL}}^c$ , where  $\gamma_{\text{SL},0}$  is the single-component part of the interface free energy, and the  $\gamma_{\text{SL}}^c$  is the chemical contribution, which is proportional to the interface thickness [54]. In our model we used an approximation for the interface free energy, where the chemical contribution was neglected, therefore the  $\gamma_{\text{SL}}$  can be set using only the single-component part,  $\gamma_{\text{SL},0}$ .

## 3.2 Equations of motion

The equations of motion (EOMs) are derived variationally starting from the free energy functional. For the non-conserved phase field, it has the following form [see Eq. (2.55)]:

$$\begin{aligned} \dot{\phi} = \epsilon(\mathbf{n}) M_\phi \left[ \epsilon_\phi^2 \nabla^2 \phi - w g'(\phi) + \right. \\ \left. + p'(\phi) [f_l(\mathbf{c}) - f_s(\mathbf{c})] - p'(\phi) \frac{\epsilon_c^2}{2} \sum_{i=1}^3 (\nabla c_i)^2 \right], \end{aligned} \quad (3.5)$$

where  $\epsilon(\mathbf{n})$  is an orientation-dependent coefficient of the mobility, which provides the 4-fold kinetic anisotropy in our model:

$$\epsilon(\mathbf{n}) = (1 - 3\epsilon_4) \left[ 1 + \frac{4\epsilon_4}{1 - 3\epsilon_4} (n_x^4 + n_y^4 + n_z^4) \right]. \quad (3.6)$$

In this expression

$$\mathbf{n} = (n_x, n_y, n_z) = \nabla\phi / |\nabla\phi| \quad (3.7)$$

is the surface normal and  $\epsilon_4$  is the strength of the anisotropy. This function does not depend on the concentration, therefore the same kinetic anisotropy applies for the  $\alpha$ -liquid and  $\beta$ -liquid interfaces, as well as to the two-phase solid-liquid interface.

The EOMs of the conserved concentration fields have the following form [see

Eq. (2.56)]:

$$\dot{c}_i = \sum_{j=1}^3 \nabla \cdot \left[ [1 - p(\phi)] M_{i,j}^c \left( \nabla \frac{\delta F}{\delta c_j} \right) \right], \quad (3.8)$$

where the  $\delta F/\delta c_i$  variational derivative is the  $\mu_i$  chemical potential:

$$\mu_i = \frac{\delta F}{\delta c_i} = [1 - p(\phi)] \frac{\partial f_l(\mathbf{c})}{\partial c_i} + p(\phi) \frac{\partial f_s(\mathbf{c})}{\partial c_i} - \epsilon_c^2 \nabla \cdot [p(\phi) \nabla c_i]. \quad (3.9)$$

A simple form of the  $\mathbf{M}^c$   $3 \times 3$  mobility matrix that maintains the condition  $\sum_i c_i = 1$ , or equivalently, the  $\sum_i \dot{c}_i = 1$  constraint is the following:

$$\mathbf{M}^c = \begin{pmatrix} 1 & -0.5 & -0.5 \\ -0.5 & 1 & -0.5 \\ -0.5 & -0.5 & 1 \end{pmatrix}. \quad (3.10)$$

In some cases where the effect of concentration fluctuations was explored, a conservative flux-noise was also included in the concentration equation. The noise term,  $\nabla(1 - \phi)\Xi_i$  was added to the right hand side of Eq. (3.8), where the vector  $\Xi_i(\mathbf{r}, t)$  is a random current of component  $i$ . Since local mass conservation ( $\sum_i c_i = 1$ ) has to be obeyed even in the presence of fluctuations, the sum of the divergences of these random currents must be zero, i.e.  $\sum_i \nabla(1 - \phi)\Xi_i = 0$  has to be satisfied. Local mass conservation is realized by the construction:

$$\Xi_i = \sum_{i \neq j} \xi_{ij}, \quad (3.11)$$

where  $\xi_{ij}$  represents that part of the total current  $\Xi_i$ , where the flow of component  $i$  is compensated by the back-flow of component  $j$  as dictated by the linked term  $\xi_{ij}(\mathbf{r}, t) = -\xi_{ji}(\mathbf{r}, t)$  in the respective expression for  $\Xi_j$ . When solving the discretized equations, the random currents  $\xi_{ij} = -\xi_{ji}$  were realized by exchanging random amounts of components  $i$  and  $j$  between each possible pairs of neighboring cells and for all the  $i$ - $j$  combinations. Random numbers of Gaussian distribution and zero mean were used to determine the amount of the components exchanged.

### 3.3 Discretized equations

The equations are solved using the finite difference method with forward Euler time-stepping scheme. Here I present the discretized form of the equations of motion, for simplicity only in 1D (one can get the 3D formulas in a straightforward way) and the kinetic anisotropy coefficient in 3D. At the discretized equations  $\phi_k^t$  denotes the phase-field value at grid point  $k$  at discrete time  $t$ ,  $\Delta x$  is the spatial step and  $\Delta t$  is the time step. The discretized phase-field equation [Eq. (3.5)] without the anisotropy term is:

$$\begin{aligned} \frac{\phi_k^{t+1} - \phi_k^t}{M_\phi \Delta t} = & \epsilon_\phi^2 \frac{\phi_{k+1}^t + \phi_{k-1}^t - 2\phi_k^t}{\Delta x^2} - wg'(\phi_k^t) + p'(\phi_k^t)[f_l(\mathbf{c}_k^t) - f_s(\mathbf{c}_k^t)] \\ & - p'(\phi_k^t) \frac{\epsilon_c^2 \sum_{i=1}^3 [(c_i)_{k+1}^t - (c_i)_{k-1}^t]^2}{2\Delta x}, \end{aligned} \quad (3.12)$$

where  $\mathbf{c}_k^t = [(c_1)_k^t, (c_2)_k^t, (c_3)_k^t]$ . The discretized concentration equation for component  $c_i$  [Eq. (3.8)] is:

$$\begin{aligned} \frac{(c_i)_k^{t+1} - (c_i)_k^t}{\Delta t} = & \sum_{j=1}^3 M_{i,j}^c \left[ \frac{(1 - \frac{\phi_{k+1}^t + \phi_k^t}{2})[(\mu_j)_{k+1}^t - (\mu_j)_k^t]}{\Delta x^2} \right. \\ & \left. - \frac{(1 - \frac{\phi_{k-1}^t + \phi_k^t}{2})[(\mu_j)_k^t - (\mu_j)_{k-1}^t]}{\Delta x^2} \right], \end{aligned} \quad (3.13)$$

where the discretized form of the chemical potential [Eq. (3.9)] is:

$$\begin{aligned} (\mu_i)_k^t = & p(\phi_k^t)(\partial_{c_i} f_s)(\mathbf{c}_k^t) + [1 - p(\phi_k^t)](\partial_{c_i} f_l)(\mathbf{c}_k^t) \\ & - \epsilon_c^2 \frac{p(\frac{\phi_{k+1}^t + \phi_k^t}{2})[(c_i)_{k+1}^t - (c_i)_k^t] - p(\frac{\phi_{k-1}^t + \phi_k^t}{2})[(c_i)_{k-1}^t - (c_i)_k^t]}{\Delta x^2}, \end{aligned} \quad (3.14)$$

where  $\partial_{c_i}$  denotes the partial derivative with respect to the component  $c_i$ .

The kinetic anisotropy [Eq. (3.6)] has the following discretized form in 3D at grid point  $(k, l, m)$  at time  $t$ :

$$\epsilon_{k,l,m}^t = (1 - \epsilon_4) \left[ 1 + \frac{4\epsilon_4}{1 - 3\epsilon_4} [(n_{k,l,m}^t)_x^4 + (n_{k,l,m}^t)_y^4 + (n_{k,l,m}^t)_z^4] \right], \quad (3.15)$$

where  $(n_{k,l,m}^t)_x$ ,  $(n_{k,l,m}^t)_y$  and  $(n_{k,l,m}^t)_z$  are the components of the surface normal vector

[Eq. (3.7)]. The discretized form of  $(n_{k,l,m}^t)_x$  is the following:

$$(n_{k,l,m}^t)_x = \frac{\phi_{k+1,l,m}^t - \phi_{k-1,l,m}^t}{[(\phi_{k+1,l,m}^t - \phi_{k-1,l,m}^t)^2 + (\phi_{k,l+1,m}^t - \phi_{k,l-1,m}^t)^2 + (\phi_{k,l,m+1}^t - \phi_{k,l,m-1}^t)^2]^{1/2}}. \quad (3.16)$$

The  $y$  and  $z$  components can be obtained similarly.



# Chapter 4

## Numerical simulations

During the simulations, the equations of motions were solved numerically on uniformly spaced rectangular 3D grids. For this, I have developed a parallel simulation code that can run on CPU clusters and graphics cards (GPU) as well. In this chapter I will introduce the code itself, the numerical methods used, the simulation environment and how the raw data were evaluated and post-processed from a simulation.

### 4.1 The simulation box

For the numerical solution of the phase-field and concentration equations using the finite difference method, the continuous equations are discretized on a lattice that consists of  $N = N_x \times N_y \times N_z$  uniformly spaced points. The discretization results in a sets of  $N$  difference equations. Solution of these equations yields the time evolution of the values of the phase-field and concentration variables in all lattice points. The choice of the lattice spacing,  $\Delta x$ , and the size of the simulation box depend on different factors. In the phase-field method, as discussed earlier, the interfaces between the phases are diffuse, which means that  $\Delta x$  must be fine enough to resolve the interface profile of the variables. Practically, 5-10 grid points are required within the interfacial regions to maintain numerical stability and accuracy [60]. On the other hand, the simulation box must be large enough to capture the features of the discussed physical system and to avoid artifacts originating from the finite size of the domain. However, with increasing number of grid points, the memory requirement and the computational time are increasing as well, that limits the maximum box size. For 3D simulations parallel

codes are essential for achieving appropriate system sizes.

The simulation box is shown in Fig. 4.1. The conditions during the simulations corresponded to directional solidification via imposing a temperature gradient along the  $z$  coordinate axis. This temperature gradient is then moved with velocity  $v_{\text{pull}}$  in the positive  $z$  direction, enforcing a front speed in this direction equal to  $v_{\text{pull}}$  for any steady-state growth form. In order to incorporate sufficiently large diffusion zone in front of the dendrites, the simulation box was longer along the growth direction, typically  $N_x \times N_y \times N_z = 96 \times 96 \times 612$  voxels<sup>1</sup>.

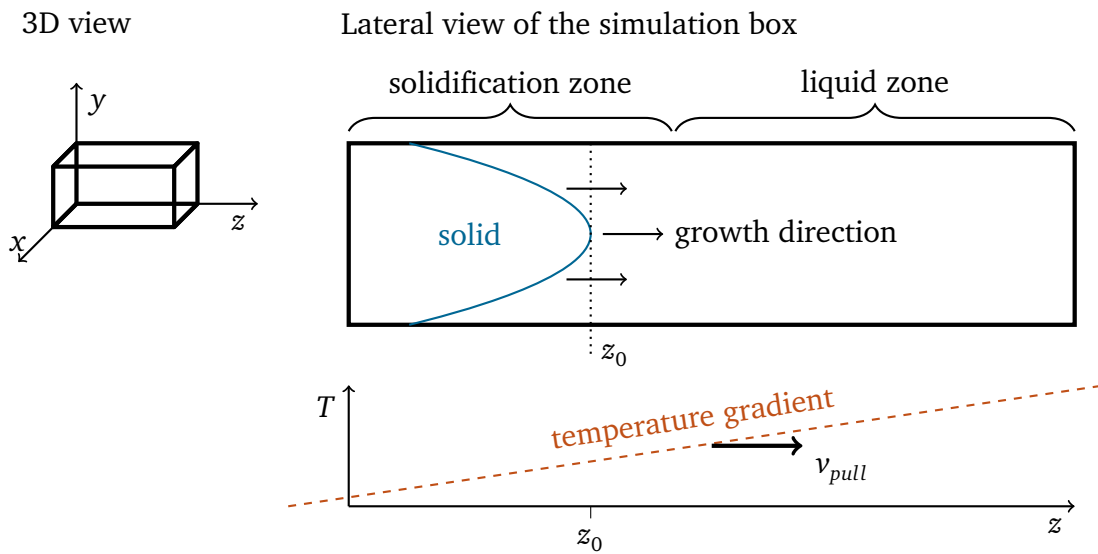


**Figure 4.1.** The simulation box. Left side: 3D view of the domain, the growth direction is along the  $z$  axis, in which direction the box is longer to incorporate the whole diffusion zone ahead of the solid front. Right top: lateral view of the simulation box. To save computation time, the phase field equation is solved only in the solidification zone. The tip of the solid was kept around the position  $z_0$  via occasionally shifting the content of the box back in the  $z$  direction by one voxel. Right bottom: the temperature gradient, which was moved with  $v_{\text{pull}}$  velocity.

To make the simulations more efficient, the box was divided into two regions, (Fig. 4.1): the solidification zone and the liquid zone. In the solidification zone the equations were solved as required by Eq. (3.5) and Eq. (3.8), while in the liquid zone, where the phase field is small ( $< 10^{-8}$ ), only the concentration equations [Eq. (3.8)] were solved, which, in this case, simplifies to a simple diffusion equation. With this approach, essentially the whole diffusion zone ahead of the solidification front was in-

<sup>1</sup>Voxel (from **v**olumetric **p**ixel) represents a value on a regular grid in 3D space, like a pixel in 2D.

corporated in the simulation box, which then ensured that the dendrite morphology became independent of the length of the simulation box.

The temperature gradient (Fig. 4.1 bottom) was imposed indirectly via making the free energy density of the solid dependent on position:

$$f_i^{*s}(z) = f_i^s - z \frac{\partial f_i^s}{\partial z}, \quad (4.1)$$

where  $z$  is the spatial coordinate along the growth direction. The velocity of the temperature gradient was  $v_{\text{pull}}$  pointing in the positive  $z$  direction. In order to make the simulations more efficient, I made the simulation box follow the solidification front by shifting its content one voxel back in the  $z$  direction whenever the  $z$  coordinate of the tip of the solid phase exceeds a position marked  $z_0$ . Using this technique, a much smaller simulation box is required to model the solidification process, which saves a lot of computation time and memory. During the shifting process, liquid with concentration  $c_{i,0}$  enters the domain on the high  $T$  side. Periodic boundary condition was used in the  $x$  and  $y$  directions and no-flux (which means that e.g.  $\partial\phi/\partial z = 0$  at the boundary) in the  $z$  direction.

The initial composition of the liquid was typically  $c_1 = c_2 = 0.455$  and  $c_3 = 0.09$ , illustrated by a white circle plotted over the planar projection of  $f_s(\mathbf{c})$  in Fig. 4.2. Therefore the corresponding equilibrium phases defined by the common tangent plane are the  $L$  liquid phase, the  $c_1$ -rich  $\alpha$  and the  $c_2$ -rich  $\beta$  solid phases (yellow circles). The third solid phase, the  $c_3$ -rich  $\gamma$ , does not appear in the system using the reference composition.

## 4.2 The simulation program

For the numerical simulations, I have developed two parallel codes. The first one was aimed to run on CPU clusters with hundreds of CPU cores. Later, the code was rewritten to be able to run on GPU cards as well. The first version was written in the C programming language using OpenMPI<sup>2</sup> [61]. The main idea in parallel computing is to split the big, computational-heavy problem into smaller parts, which then can

---

<sup>2</sup>The MPI (Message Passing Interface) protocol is a standard communication system for parallel computers. OpenMPI is an open source implementation of MPI.

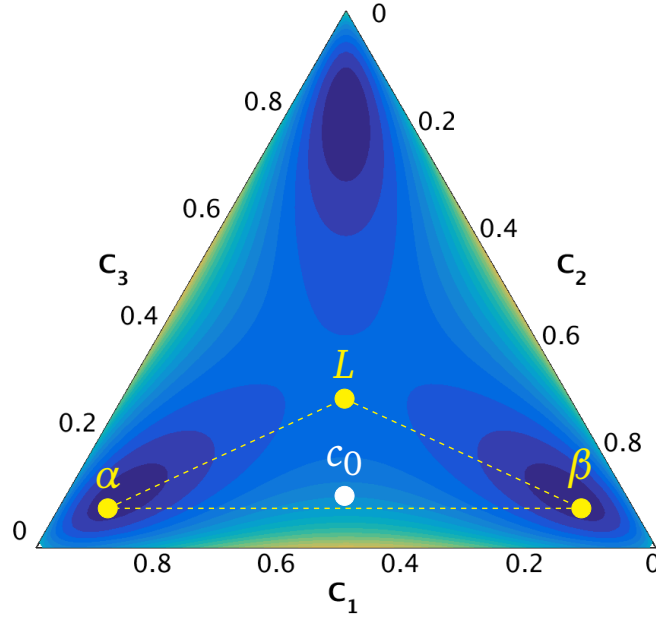


**Figure 4.2.** The equilibrium phases over the planar projection of  $f_s(\mathbf{c})$ . The yellow circles show the compositions of the three equilibrium phases corresponding to the initial liquid concentration  $c_0$  (white circle).

be executed simultaneously, therefore the run time becomes smaller. Optimally, the speedup from parallelization would be linear (i.e. proportional to the number of processors used), however, usually not every part of the problem is parallelizable, thus the achievable speedup has a theoretical maximum value depending on the problem [62].

An illustration of partitioning a simulation domain can be seen in Fig. 4.3. In this 2D example, the domain is split into two sections along the  $z$  axis, each computing node holding and operating on only half size of the full domain. However, to calculate the spatial derivatives in 2D, values of the four neighboring points are also required. These adjacent points are available for inner the cells, but some neighbors are missing for the cells located at the section edges (e.g. the right side of  $z = 4$  column at Node 1). This issue can be solved by using a *ghost layer*, an additional column of points added to the section edges, which holds the boundary cells of the corresponding adjacent section. After each time step, the cells in the ghost layers are overwritten with the updated values calculated at the adjacent nodes. The additional communication time, in which the neighboring nodes exchange their ghost layers, can be practically eliminated by calculating the boundary cells of the sections first, then starting the synchronization process. In this way, the synchronization can be finished before the calculation of the

inner cells. Using special network hardware (called InfiniBand<sup>3</sup>) between the computing nodes also helps in reducing the communication time with greater bandwidth and smaller latency than regular ethernet network adapters.

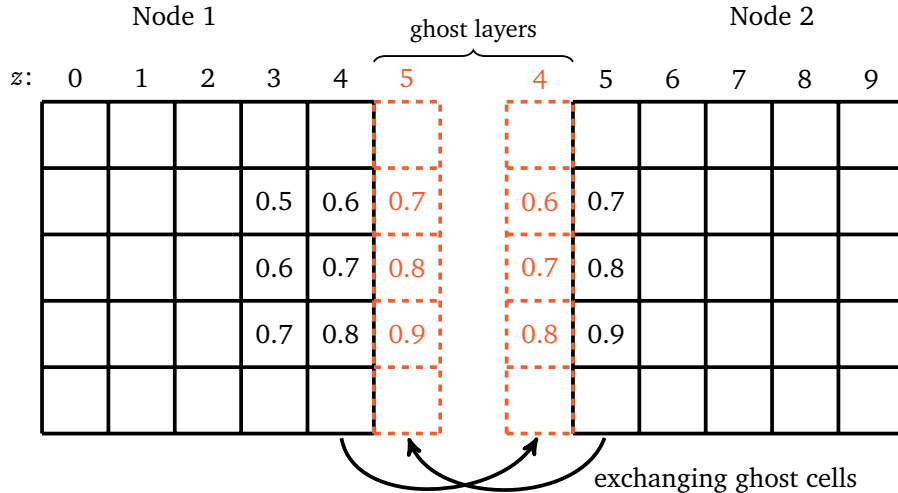


**Figure 4.3.** Partitioning a 2D simulation box between two nodes (black cells). At the edges of the sections the ghost layers contain the values of boundary points (red cells) from the adjacent blocks. After each time step, the sections update their ghost cells with their new values.

The creation of the GPU-compatible version of the code was inspired by the availability of high performance, but relatively cheap graphics cards and the advancement in the GPGPU<sup>4</sup> ecosystem in the recent years. In an optimal case, the performance of a single GPU card is comparable to a CPU cluster containing hundreds of cores.

The main differences in the programming of GPUs are in the memory and execution models. A GPU card has its own very fast memory, which is separated from the system memory<sup>5</sup>, one has to explicitly take care of uploading and downloading the calculated data to/from the card. The computational tasks (e.g. a time step of the phase field EOM) are arranged in *kernel functions*, which can be submitted for execution on a GPU for a given *index space*, e.g. items of an array. Then the device executes the kernel function exactly one time for each item using thousands of computing units

<sup>3</sup>InfiniBand is a network communication standard developed in 2000 for high-performance computing. The recent version has up to 290 GBit/s bandwidth with only 0.5  $\mu$ s adapter latency. Introduction: [http://www.mellanox.com/pdf/whitepapers/IB\\_Intro\\_WP\\_190.pdf](http://www.mellanox.com/pdf/whitepapers/IB_Intro_WP_190.pdf)

<sup>4</sup>GPGPU: General-Purpose Computing on Graphics Processing Units <https://arxiv.org/abs/1408.6923>

<sup>5</sup>See chapter 3.3 in OpenCL 2.2 Specification <https://www.khronos.org/registry/OpenCL/specs/opencl-2.2.pdf>

(cores in the GPU) in parallel.

The GPU version of the code was written in OpenCL (Open Computing Language<sup>6</sup>) with auxiliary parts (the *host* program) in Python<sup>7</sup> using PyOpenCL library [63]. It can run on a single GPU only, therefore it could be used for system sizes that fit in the few gigabytes memory of a card.

### 4.2.1 Structure of the simulation program

The block diagram of the program is shown in Fig. 4.4. After the initialization of the simulation box, a time stepping begins. First the chemical potentials [Eq. (3.9)] are calculated and stored in auxiliary arrays, that simplify calculation of the concentration equations for the cost of three additional arrays. Next, the phase field equation

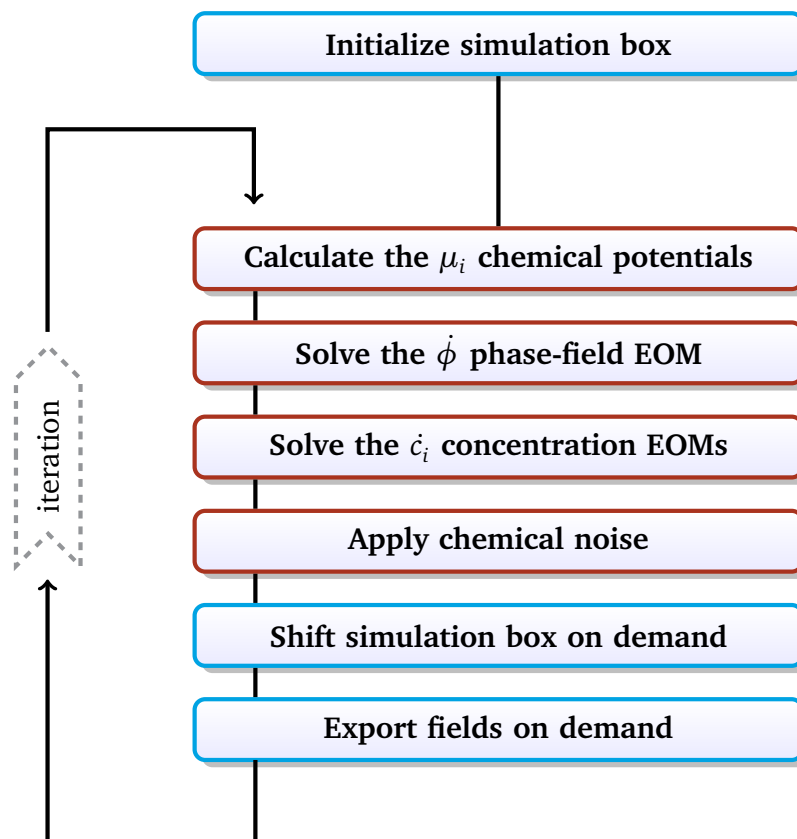


**Figure 4.4.** Block diagram of the simulation program.

<sup>6</sup>OpenCL is a general framework for writing parallel programs that execute across heterogeneous platforms (like CPUs or GPUs). <https://www.khronos.org/opencl>

<sup>7</sup>Python is a free, high-level, dynamic typed, general-purpose programming language. It is very widely used in info-tech and also very popular in the scientific community due to availability of many useful libraries and tools. <https://www.python.org>

[Eq. (3.5)] is solved, then the concentration equations [Eq. (3.8)] using the stored values of chemical potentials. After that, the flux noise is added to the concentration fields, if the chemical noise is turned on. In the end of the time step, the box shifting and exporting of the arrays for evaluation take place, if required. The equations are solved using the finite difference method with the forward Euler explicit time-stepping scheme (Chapter 19 of [64]).

## 4.2.2 Visualization of the results

The raw results from the simulations are sets of 3D arrays, containing the phase-field and concentration values. To plot the various phases in 3D perspective, first, the boundary of the solids was determined by the  $\phi = 0.9$  isosurface<sup>8</sup> of the phase field. The resulted set of triangles was colored by using the local value of concentration fields. An example of spherical particles of the two solid phases,  $\alpha$  and  $\beta$ , can be seen in Fig. 4.5.

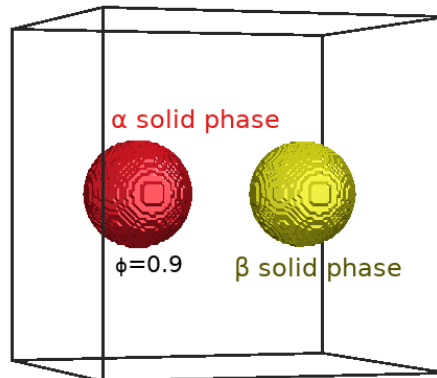


**Figure 4.5.** Example of spherical particles of the two solid phases. The surface of the particles was determined as the  $\phi = 0.9$  isosurface of the phase field. The solid phases were then identified and colored according to the underlying concentration values. Here  $\alpha$  solid phase is red,  $\beta$  is yellow, and the liquid phase is transparent.

Here,  $\alpha$  solid phase (in which the concentration of  $c_1$  component is high) is colored with red,  $\beta$  solid phase (with high  $c_2$  concentration) is yellow<sup>9</sup>, and the liquid phase is transparent. In some cases not the equilibrium solid phases appear, rather a metastable

<sup>8</sup>MATLAB environment was used to determine the isosurface and create 3D plots.

<sup>9</sup>Originally blue color was used for the  $\beta$  phase, but in order to have better contrast in the printed (grayscale) matters, the blue color was replaced with yellow. However in the supplementary videos, the original color scheme remained.

one (due to e.g. very high pulling speed), in which  $c_1 \approx c_2$ . That metastable solid phase is colored with purple<sup>10</sup>.

### 4.3 Starting configurations

Two kinds of initial configurations were used to start the solidification process. On the left side of Fig. 4.6, a single seed of the homogeneous  $\alpha$  phase is shown, where the radius of the spherical particle was greater than the critical radius of the nucleation to prevent remelting of the seed. The composition of liquid was set to  $c_1 = c_2 = 0.455$  and  $c_3 = 0.09$ , and flux noise was added in this case.

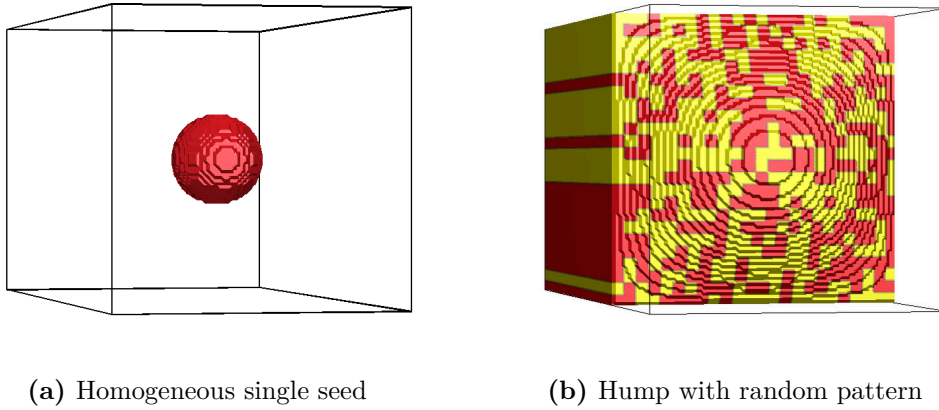


**Figure 4.6.** Initial configurations. (a) Homogeneous spherical seed of the  $\alpha$  solid phase. (b) Optimized configuration to shorten the required time for the two-phase dendrites to appear. Slab of solid with a small hump on top, random transversal pattern of  $\alpha$  and  $\beta$  solid phases of typical size scale close to the natural wavelength of eutectic growth.

For most of the simulations an optimized starting configuration was used, in which a slab of solid with a small hump was placed into the box [Fig. 4.6 (b)]. The solid was made up as a random distribution of the  $\alpha$  and  $\beta$  phases in a length scale comparable to the preferred wavelength of eutectic growth. This setup was chosen to approximate the result of the initial transient of the previous approach, and therefore saving substantial computation time. To validate this approach, test simulations have been made in a few cases, and the results of the two approaches were compared (see Section 5.4.1).

---

<sup>10</sup>Purple for this metastable phase makes sense considering it is a mixture of the original colors: red and blue.



## 4.4 Reference conditions

The default parameters for the simulations are collected in Table 4.1. No noise has been added to the equations of motions unless stated otherwise.

The parameters used in the ideal- and regular solution models were chosen so that the ternary phase diagram is symmetric in the  $c_1 - c_2$  components. Therefore, the reference composition of the liquid ( $c_1 = c_2 = 0.455$  and  $c_3 = 0.09$ ) belongs to the three-phase eutectic line between the  $l + \alpha$  and  $l + \beta$  coexistence regions in the ternary eutectic phase diagram. Consequently, when the reference composition is used, the  $\alpha - \beta$  volume fraction will be 0.5.

Parameter	Value
Time step	$\Delta t = 0.0025$
Spatial step	$\Delta x = 1.0$
Grid size	$N_x \times N_y \times N_z = 96 \times 96 \times 612$
Size of the simulation box:	$L_i = N_i \cdot \Delta x$ , where $i = x, y$ or $z$
Boundary conditions	$x$ and $y$ direction: periodic, $z$ : no-flux
Initial composition of the liquid	$c_1 = c_2 = 0.455$ , $c_3 = 0.09$
Pulling velocity	$v_{\text{pull}} = 0.2$
Phase-field mobility	$M_\phi = 1.0$
Free energy density parameters	$f_i^l = 0$ , $f_i^s = -0.964$
Interaction parameters	$\Omega_{12} = 3.05$ , $\Omega_{23} = \Omega_{31} = 3.0$
Temperature gradient	$\partial f_i^s / \partial z = 3.667 \times 10^{-4}$
Solid-liquid interface free energy	$\gamma_{\text{SL},0} = 0.059$
Kinetic anisotropy	$\epsilon_4 = 0.3$
Coefficients of the square-gradients	$\epsilon_\phi^2 = 0.75$ , $\epsilon_c^2 = 0.4$
Free energy scale	$w = 0.0469$

**Table 4.1.** Reference conditions of the simulations.

## 4.5 Hardware used

For the numerical simulations various computers have been utilized. The majority of the simulations were run on one of our CPU clusters located in Wigner RCP, Budapest. There are three blocks of nodes, whose parameters have been summarized in Table 4.2.

A block has several identical computing nodes<sup>11</sup> (which makes parallelization easier), and each node in a block has been connected by a high-speed InfiniBand network.

For a few large simulations I used the Hitachi SR16000/M1 supercomputer<sup>12</sup> in Tohoku University, Japan, which has 1280 IBM POWER7 3.83 GHz processors in total. However, the largest block one can utilize at once, was limited to 512 or 2048 cores, which, as it turned out, did not reduced the run time of the simulations that much compared to our largest block.

The GPU version of the simulation program used the following graphics cards: 5×Nvidia GTX 580 3 GB<sup>13</sup>, 5×Nvidia GTX 590 3 GB<sup>14</sup> and 8×Nvidia Tesla C2050 3 GB<sup>15</sup>.

	<b>CPU block A</b>	<b>CPU block B</b>	<b>CPU block C</b>
Nodes	16	36	16
CPU <sup>16</sup>	Intel Xeon L5420	Intel Xeon E5530	Intel Xeon X5650
CPU frequency	2.5 GHz	2.4 GHz	2.67 GHz
CPUs/node	2	2	2
Total CPUs	32	72	32
Cores/CPU	4	4	6
Total cores	128	288	192
Memory/node	16 GB	24 GB	24 GB
Total memory	256 GB	864 GB	384 GB
Network speed	20 Gb/s	40 Gb/s	40 Gb/s

**Table 4.2.** Details of the used CPU clusters.

The typical computation times were between 35-40 hours for the reference grid size. A few large scale simulations with  $380 \times 380 \times 511$  grid size (see Section 5.5) took more than 3 weeks of computation time.

<sup>11</sup>Supermicro 1U Twin systems: 2 computing nodes per 1U rackmount system <https://www.supermicro.nl/products/nfo/1UTwin.cfm>

<sup>12</sup>[http://www-lab.imr.tohoku.ac.jp/~hitachi/super\\_en/outline\\_en.html](http://www-lab.imr.tohoku.ac.jp/~hitachi/super_en/outline_en.html)

<sup>13</sup><https://www.geforce.com/hardware/desktop-gpus/geforce-gtx-580/specifications>

<sup>14</sup><https://www.geforce.com/hardware/desktop-gpus/geforce-gtx-590/specifications>

<sup>15</sup>[http://www.nvidia.co.uk/object/product\\_tesla\\_C2050\\_C2070\\_uk.html](http://www.nvidia.co.uk/object/product_tesla_C2050_C2070_uk.html)

<sup>16</sup>More information about the CPUs: Xeon L5420: [https://ark.intel.com/products/33929/Intel-Xeon-Processor-L5420-12M-Cache-2\\_50-GHz-1333-MHz-FSB](https://ark.intel.com/products/33929/Intel-Xeon-Processor-L5420-12M-Cache-2_50-GHz-1333-MHz-FSB), Xeon E5530: [https://ark.intel.com/products/37103/Intel-Xeon-Processor-E5530-8M-Cache-2\\_40-GHz-5\\_86-GTs-Intel-QPI](https://ark.intel.com/products/37103/Intel-Xeon-Processor-E5530-8M-Cache-2_40-GHz-5_86-GTs-Intel-QPI), Xeon X5650: [https://ark.intel.com/products/47922/Intel-Xeon-Processor-X5650-12M-Cache-2\\_66-GHz-6\\_40-GTs-Intel-QPI](https://ark.intel.com/products/47922/Intel-Xeon-Processor-X5650-12M-Cache-2_66-GHz-6_40-GTs-Intel-QPI)

# Chapter 5

## Results and discussion

In this chapter the results are presented, starting with the formation of a *steady-state* two-phase single spiral. Then, the exploration of the parameter space is shown in order to investigate the properties of the two-phase dendrites, and how they compare to their one-phase counterparts, and also to find the optimized conditions for growing spiraling structures. The parameter space is defined by composition, temperature gradient, pulling speed, solid-liquid interfacial free energy and kinetic anisotropy. A broad range of these parameters has been explored. Then, the various eutectic patterns (e.g. single- and multi-armed spirals) and the stochastic nature of pattern selection are presented. After that, the significance of anisotropy during the forming steady-state spiraling structures is discussed with the help of large scale simulations. Lastly, dendrites formed with unequal volume fraction of the phases (using off-eutectic composition) are presented.

### 5.1 Formation of a two-phase dendrite

Using the reference conditions (Table 4.1), the evolution of a two-phase single spiral dendrite can be seen in Fig. 5.1. The growth direction is along the z coordinate axis, which is pointing outwards from the plane of the page. The starting configuration is shown in Fig. 5.1 (a), where the hump setup is used. First, the hump starts to grow, while the initial fine pattern becomes coarser [panel (b)]. After that, the hump becomes bigger [panel (c)], and a striped eutectic pattern starts to appear at the solid front. At this point, the pattern is still disordered, i.e. a clear spiral morphology cannot be

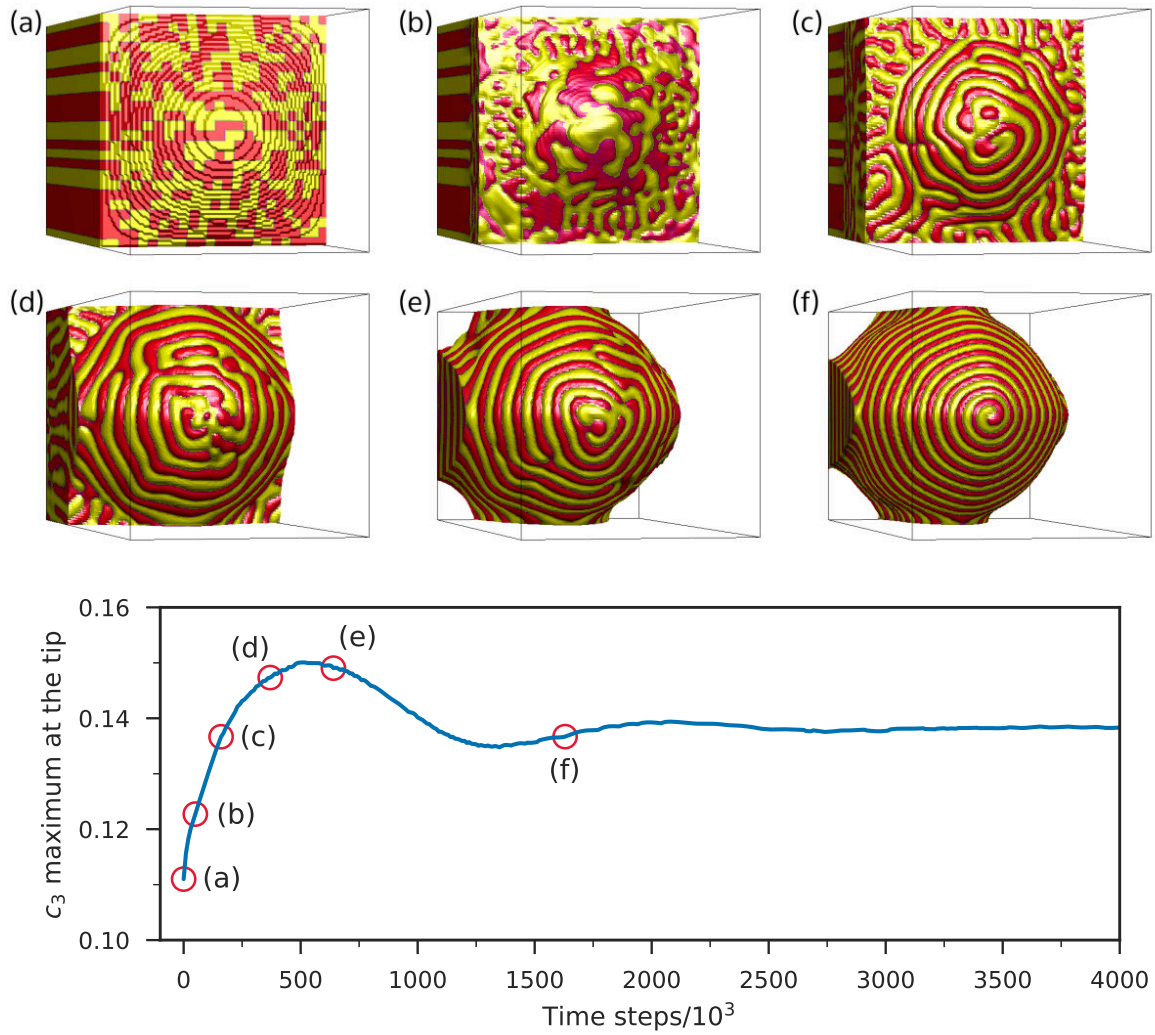


**Figure 5.1.** Formation of a two-phase single spiral dendrite traveling with a constant velocity. (a) Initial random configuration. (b) The hump starts to grow while the initial pattern becomes coarser. (c) An unordered pattern of  $\alpha$  and  $\beta$  lamellae appears. (d)-(e) The solidification front evolves into a structure that has a shape of a dendrite while there are still many defects in the pattern. (f) The morphology becomes stable, the structure evolves into a steady-state single spiral dendrite. The snapshots are taken from the  $t = 50, 160, 370, 640,$  and  $1630 \times 10^3$ th time steps. The simulation box follows the tip of the dendrite during the growth. Bottom: concentration of the third component as function of time just ahead of the tip with markings indicating the times and  $c_3$  values of the snapshots.

Video 5.1: <https://rlphd.phasefield.hu/s1>

identified. The  $\alpha$  and  $\beta$  solid lamellae have many defects, like lamella-splitting/merging, kinks and elbows, which are forming at the tip region, then proceed through the solid. In panels (d) and (e), the solidification front reaches its final dendritic shape, while the pattern is still not ordered. After a long transient period, in panel (f), an ordered

pattern, in this case a stable single spiral motif appeared on the surface of the dendrite. We call this stabilized structure a *steady-state* dendrite, in the sense that the shape of the solidification front and the number of spiral arms do not change during the further growth. Naturally, the eutectic patterns change continuously (e.g. the two solid phases are rotating around each other) during the solidification according to their respective growth modes (see Section 5.4). In the bottom of Fig. 5.1 the pile-up of the third component ( $c_3$ ) has been plotted. The circles mark the values of  $c_3$  at times corresponding to the snapshots.

## 5.2 Domain of ordered two-phase dendrites

To identify the concentration region, in which dendrites with ordered pattern form in the phase diagram, the solidification morphology has been investigated in the neighborhood of the reference composition ( $c_1 = c_2 = 0.455$ , and  $c_3 = 0.09$ ), while the other

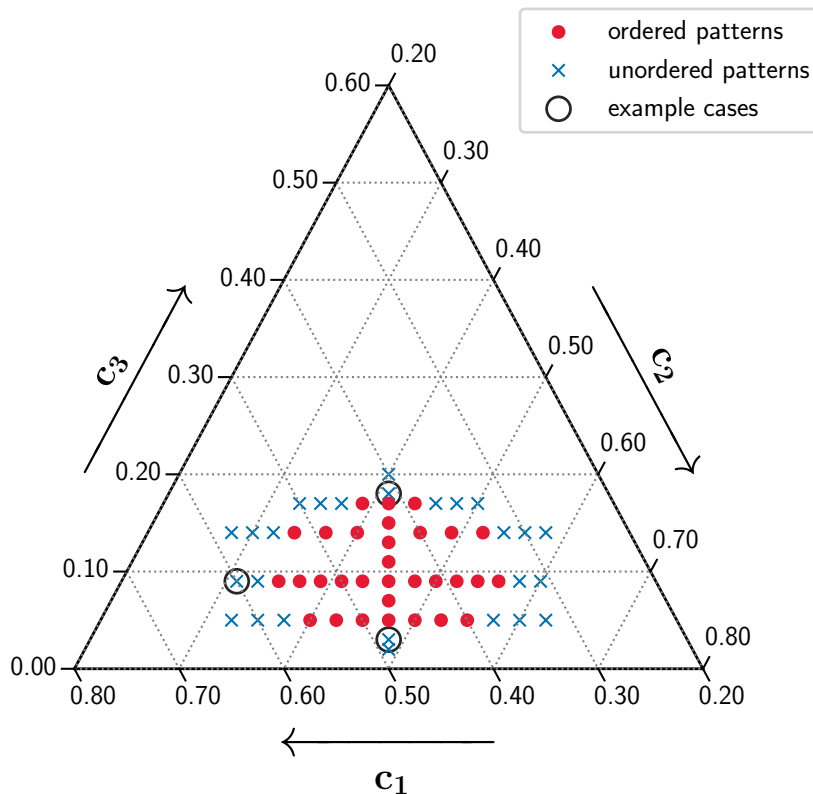


**Figure 5.2.** Compositions at which two-phase dendrites of target or spiral pattern have been observed using the reference parameter set (Table 4.1). The open circles mark the examples structures showed in Fig. 5.3.

parameters are kept at their reference values listed in Table 4.1. The respective domain is shown in Fig. 5.2. This indicates that spiraling eutectic dendrites may be observed in a region that extends to  $0.35 < c_1 < 0.56$  along the line  $c_3 = 0.09$ , whereas it covers the range  $0.05 < c_3 < 0.17$  along the line of symmetric compositions ( $c_1 = c_2$ ).

In Fig. 5.3 (a), the asymmetric composition case ( $c_1 = 0.60$ ,  $c_2 = 0.31$  and  $c_3 = 0.09$ ) is shown, where the volume fractions of the two solid phases are significantly different. Here the  $\alpha$  majority solid phase forms the tip and the inner region of the dendrite, while the  $\beta$  minority phase appears only at the bottom of the dendrite in the form of thin channels. The high asymmetry between the volume fractions of the phases prevents the forming of ordered morphologies.

In the  $c_3$  component rich case [Fig. 5.3 (b)], where  $c_3 = 0.18$  and  $c_1 = c_2 = 0.41$ , the formation of individual  $\alpha$  and  $\beta$  solid phases was prevented by the limited diffusion of the components. The dendrite is formed by a metastable solid phase (colored with purple), where  $c_1 = c_2 = 0.44$  and  $c_3 = 0.12$ , instead of the equilibrium  $\alpha$  and  $\beta$  phases. Similar behavior can be seen, when the pulling speed is high enough (see Section 5.3.3).

In contrast, at the low  $c_3$  component case [Fig. 5.3 (c)], where  $c_3 = 0.03$  and  $c_1 = c_2 = 0.485$ , the solidification front is flat since the concentration of  $c_3$  component is not enough to generate the usual dendritic shape.

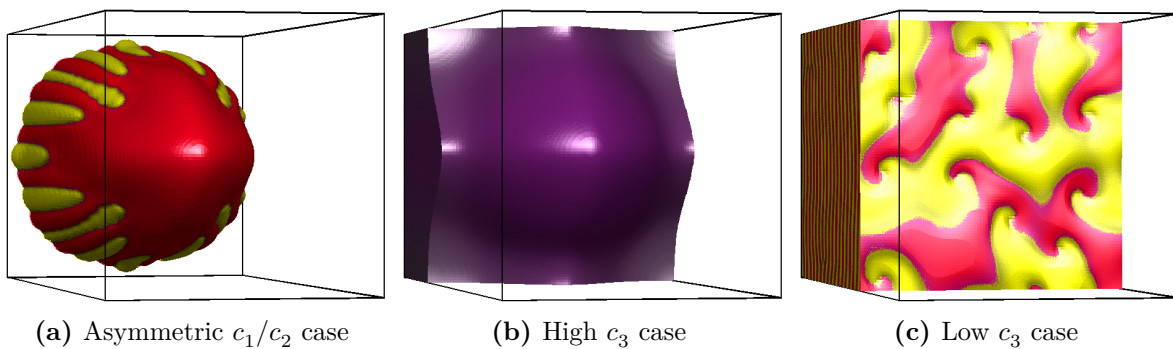


**Figure 5.3.** Structures formed outside of the ordered-pattern region. (a) Asymmetric composition case, where the  $c_1/c_2$  ratio is high, therefore the volume fractions of the two solid phases are significantly different. The majority  $\alpha$  solid phase forms the dendrite, while the minority  $\beta$  phase appears only at the bottom of the dendrite. (b) High  $c_3$  concentration case, where the dendrite is formed by a metastable phase (colored with purple), in which the concentration is  $c_1 = c_2 = 0.44$  and  $c_3 = 0.12$ . (c) Low  $c_3$  concentration case, where the front is flat with unordered pattern.

## 5.3 Dendrite morphology

The shape of the dendrites and the eutectic wavelength can be influenced by multiple ways. First, I describe the procedure I used for evaluating quantities that describe the dendritic and eutectic microstructure, then I present a typical two-phase spiraling dendrite formed with the reference parameter set (Table 4.1). Finally I show the effects of the pulling speed of the temperature gradient, the solid-liquid interface energy and the kinetic anisotropy on the solidification front.

### 5.3.1 Characteristic quantities

To characterize the results, the tip radius ( $R_{\text{tip}}$ ) and the wavelength of the eutectic pattern ( $\lambda$ ) have been measured on the structures. The eutectic wavelength has to be measured on the surface of the solid front (see Fig. 5.4). It is not an easy task to automate, since it has to be measured on a 3D surface, and as it will be seen, the shape of the solidification front and the eutectic pattern change significantly with the changing pulling velocity. Because of this, the eutectic wavelength was measured manually, by plotting the solidification front in 3D, then finding a characteristic part on the surface, where both solid phases were present, and then measuring the distance perpendicularly to the lamellae of the phases. This process was repeated a few times at different parts of the surface to get an averaged value of  $\lambda$  (typically with  $\pm 0.9$  standard deviation).

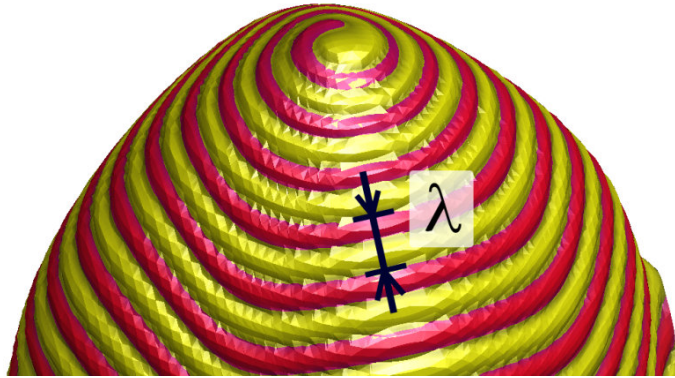


**Figure 5.4.** Illustration of the eutectic wavelength ( $\lambda$ ) on the surface of a single spiral dendrite. The wavelength was measured at multiple parts of the surface to get an averaged value.

The tip radius was calculated programmatically by first fitting a paraboloid function to the  $\phi = 0.5$  isosurface in the tip region of the dendrite. As in the presence of anisotropy the dendrite is not axially symmetric, this fit was used just to obtain the tip coordinates. Then, the exact form of the solid-liquid interface was obtained using the  $y - z$  planar section of the dendrite going through the tip, by locating the points corresponding to  $\phi = 0.5$  phase field value. Finally, the radius of the dendrite was determined by fitting a parabolic function to the solid-liquid interface points near the tip region. The process was repeated several times at different time steps after the dendrite became a steady-state structure to get an averaged value of  $R_{\text{tip}}$  (typically with  $\pm 0.4$  standard deviation).

### 5.3.2 Morphology of a single spiral dendrite

A typical two-phase single spiral dendrite is shown in Fig. 5.5. In Fig. 5.5 (a) both phases are plotted showing the spiraling motif on the surface. In panel (b) only the  $\alpha$  phase is shown, displaying the helical structure formed by this solid phase, which is a connected domain inside the dendrite for the spiraling patterns (see Fig. 5.16 for cross sections). In panel (c) the contour lines are showing the transverse  $x - y$  plane sections at  $10\Delta x$  distances (using  $\phi = 0.5$  value for the contours). Behind the tip it has a rounded-square-like section.

In the fin directions (e.g.  $x - z$  plane), the longitudinal profile can be fitted reasonably well by  $z = z_{\text{max}} - |x|^\nu$  expression, where  $z_{\text{max}}$  is the tip position,  $x$  is the distance from the axis of the dendrite, and  $\nu$  is  $\sim 1.58 \pm 0.05$  [Fig. 5.5 (d)]. This exponent is somewhat smaller than  $\nu = 5/3$  predicted theoretically for single-phase dendrites [65], or the  $\nu = 1.67$  obtained experimentally for xenon dendrites [66, 67, 68]. These findings are in a reasonable agreement with a detailed characterization of tip shapes of single-phase dendrites by phase-field simulations [69]. This indicates that there is a crossover between a corrected paraboloid valid close to the tip and the power-law behavior on the tail; therefore, the results depend (here too) on the range of distances one chooses to fit the shape.



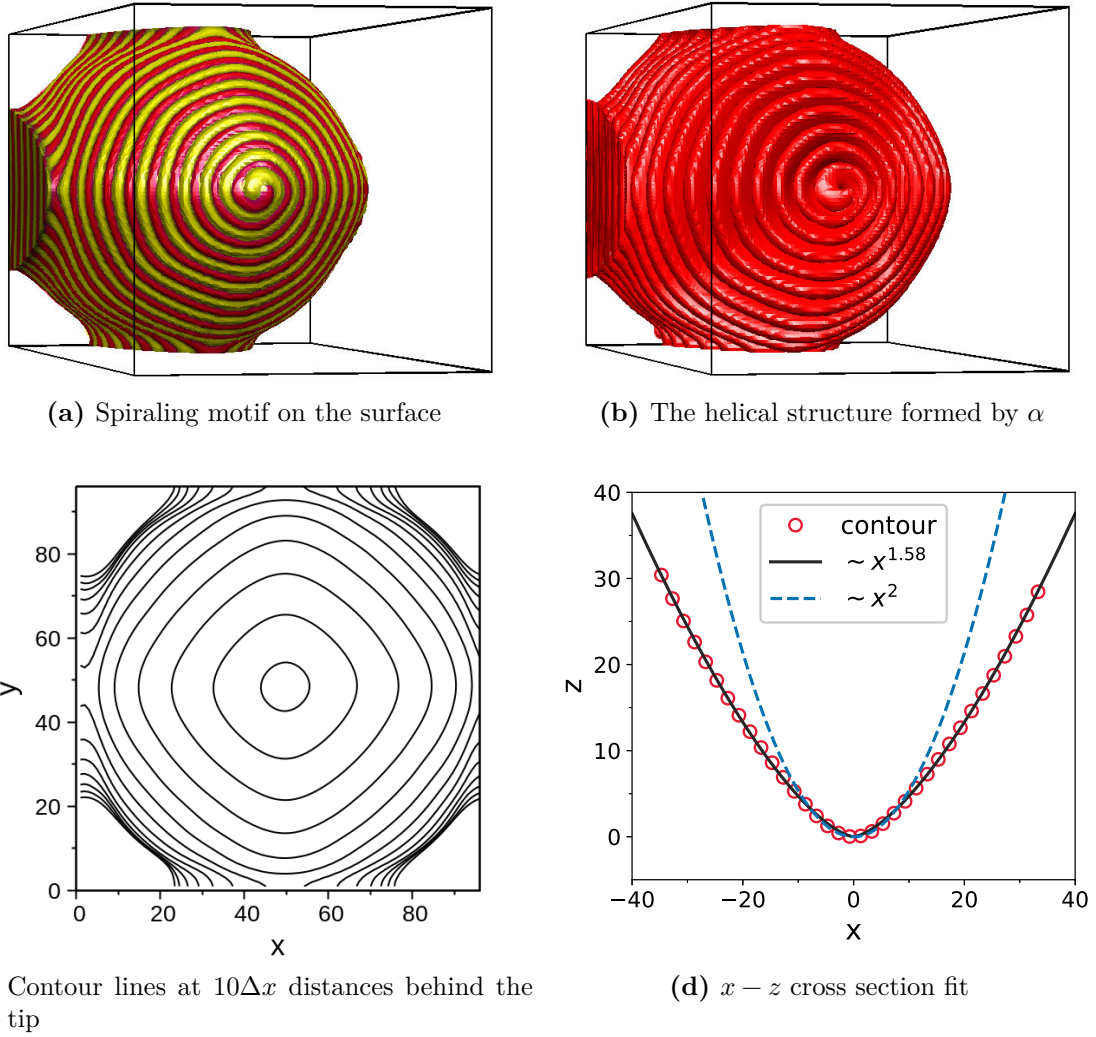


**Figure 5.5.** Two-phase spiraling dendrite growth under the reference conditions (Table 4.1).

### 5.3.3 Effect of pulling speed and the Jackson–Hunt scaling

The solidification morphology has been investigated as a function of pulling velocity ( $v_{\text{pull}}$ ) to see whether the standard relationship [see Eq. (2.49)] applies to the eutectic pattern on the surface of the two-phase dendrites.

For low pulling velocities ( $v_{\text{pull}} < 0.01$ ) a planar front with a disordered lamellar pattern can be observed [see Fig. 5.6]. Increasing  $v_{\text{pull}}$  resulted in a dendritic morphology yet with disordered lamellar pattern. Around  $v_{\text{pull}} \approx 0.2$  ordered eutectic patterns form, such as the target and spiraling patterns. At higher  $v_{\text{pull}} \approx 0.3$ , solidification takes place via forming lamellae perpendicular to the temperature gradient. Above this velocity partitionless dendrite forms indicating that solute trapping does not occur for  $c_3$  at the same level as for the other two components. At even higher pulling velocities

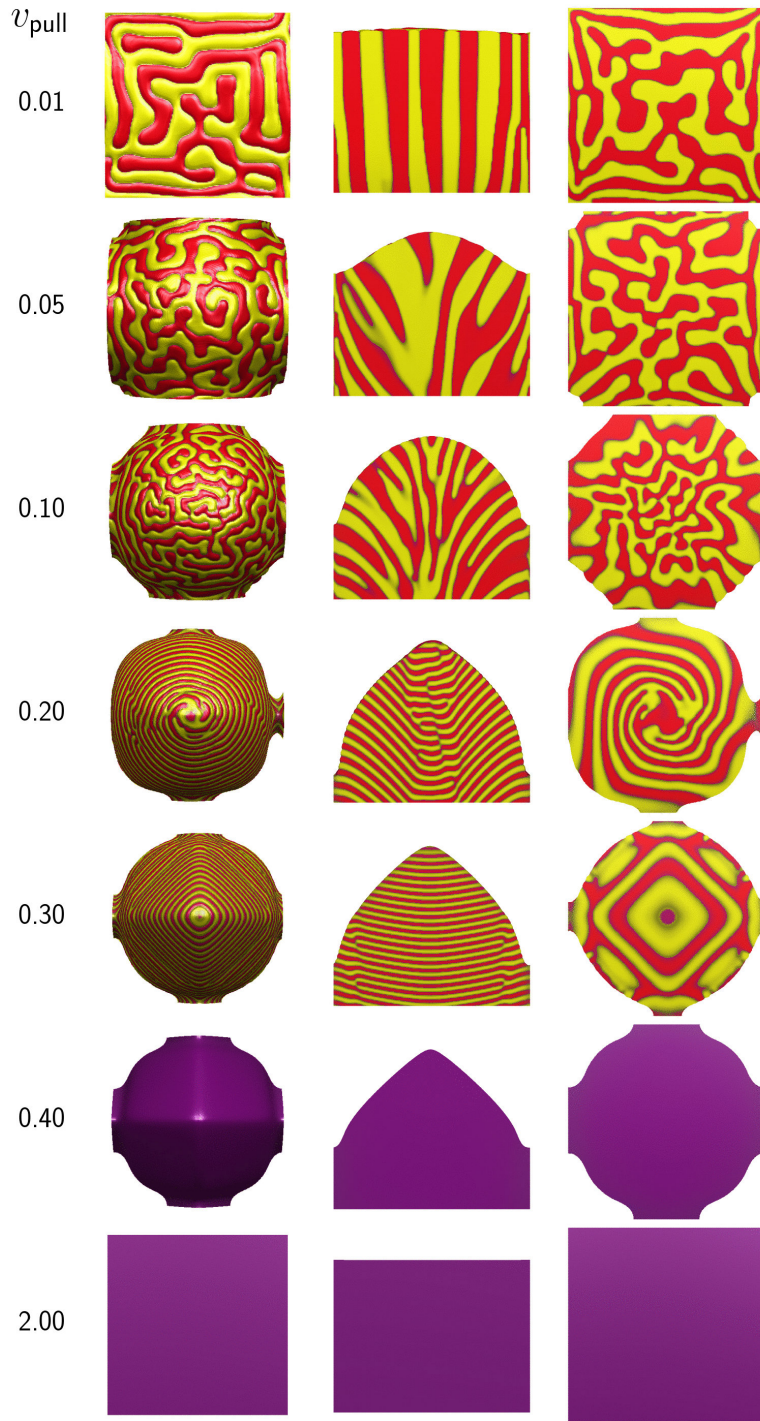


**Figure 5.6.** Solidification morphology and pattern formation as a function of pulling velocity  $v_{\text{pull}}$ . The front view (first column), the longitudinal cross section (second column) and transverse cross sections (third column) are displayed. With increasing velocity, the sequence of growth morphologies is: flat front lamellae  $\rightarrow$  eutectic colonies  $\rightarrow$  eutectic dendrites  $\rightarrow$  dendrites with target pattern  $\rightarrow$  partitionless dendrites  $\rightarrow$  partitionless flat front. At extremely low and high velocities planar fronts develop. Above  $v_{\text{pull}} \approx 0.35$  solidification takes place without  $c_1/c_2$  partitioning. At extreme high velocities ( $v_{\text{pull}} \gtrsim 0.8$ ) full solute trapping occurs.

( $v_{\text{pull}} \approx 2.0$ ) partitionless growth with a flat interface has been observed.

The results shown in Fig. 5.6 suggest that the transition from flat lamellar eutectic structure to the partitionless growth with flat interface happens via the following sequence with increasing pulling velocity: flat lamellar front  $\rightarrow$  eutectic colonies  $\rightarrow$  eutectic dendrites  $\rightarrow$  dendrites with target pattern  $\rightarrow$  partitionless dendrites  $\rightarrow$  partitionless flat front.

During the transition from a flat surface with lamellae perpendicular to it (seen at small velocities) to a flat surface at full solute trapping (at high velocities), the direction of lamellae is altering gradually from the usual parallel to the temperature gradient seen at low velocities to perpendicular to the temperature gradient seen at  $v_{\text{pull}} \approx 0.3$ . Similar transition (lamellae parallel with the temperature gradient to lamellae perpendicular to it) has been observed when increasing the velocity in binary eutectic simulations [70, 71].

### Jackson–Hunt scaling

It was found that the natural length scale of eutectic solidification follows the Jackson–Hunt scaling (see symbols and the fitted Eq. (2.49) as solid line in Fig. 5.7), confirming thus the assumption made in Ref. [72].

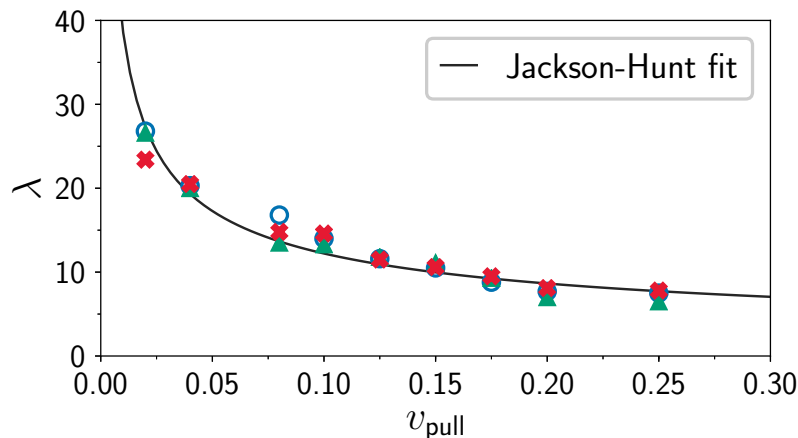


**Figure 5.7.** The wavelength of eutectic solidification as a function of pulling velocity. (Symbols of different colors denote series of simulations with different initial patterns.) Note the reasonable agreement with the Jackson-Hunt scaling, shown by the  $\lambda \propto v_{\text{pull}}^{-1/2}$  solid line.

### 5.3.4 Effect of solid-liquid interface free energy

For single-phase dendrites a theoretical relationship,  $R_{\text{tip}} \propto \gamma_{\text{SL}}^{1/2}$  has been derived [73, 30]. To see how far a two-phase dendrites follow the behavior of single-phase dendrites, the magnitude of the solid-liquid interface free energy ( $\gamma_{\text{SL}}$ ) has been varied via changing the free energy of the single-component solid-liquid interface energy ( $\gamma_{\text{SL},0}$ ). After the dendrite reached its steady-state, the tip radius ( $R_{\text{tip}}$ ) was evaluated and averaged in the fin directions. The result is shown in Fig. 5.8. It was found that  $R_{\text{tip}} \propto \gamma_{\text{SL},0}^{0.50 \pm 0.01}$ , which is very close to the theoretical relationship derived for single-phase dendrites. It probably indicates that the chemical contribution is negligible to the total interfacial free energy  $\gamma_{\text{SL}}$ , which supports our argument that  $\gamma_{\text{SL}}$  can be set using only the single-component part,  $\gamma_{\text{SL},0}$  (see Section 3.1).

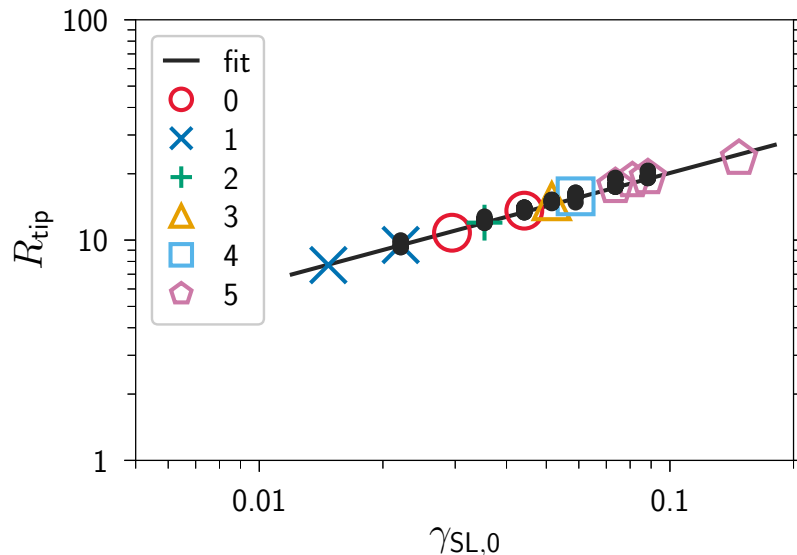


**Figure 5.8.** Tip radius vs. solid-liquid interface energy. Results obtained with the same initialization but at different  $\gamma_{\text{SL},0}$  values are depicted by different symbols according to their actual eutectic pattern. The black symbols stand for 20 additional simulations, which were performed under the same condition as the underlying ones, except that the initial random spatial distribution of the solid phases was different.

The number of spiral arms,  $N_{\text{arm}}$ , was also evaluated for each dendrite via counting the individual spiral arms in a perpendicular cross section. The different symbols in Fig. 5.8 indicate the different value of  $N_{\text{arm}}$  of the dendrite (using empty circle for the target pattern, where  $N_{\text{arm}} = 0$ ). The symbols suggest that increasing  $\gamma_{\text{SL},0}$  tends to increase the number of spiral arms as well, but not in a monotonic way.

Simulations under the same conditions ( $\gamma_{\text{SL},0}$ ) but with different initial pattern can result dendrites with different  $N_{\text{arm}}$ . This stochastic behavior and pattern-selection depending on physical parameters will be discussed in more detail later in Section 5.4.1.

To check whether the eutectic pattern has significant effect on the shape of the dendrite, 20 additional simulations (with different initial pattern) were performed at some specific values of  $\gamma_{\text{SL},0}$ . These tip radii are plotted with small black points in Fig. 5.8. The deviation of tip radii for one specific value of  $\gamma_{\text{SL},0}$  was less than 5%, indicating that the shape of the dendrite is essentially independent of the eutectic pattern ( $N_{\text{arm}}$ ).

### 5.3.5 Effect of kinetic anisotropy

Another way to influence the shape of the dendrites is to change the kinetic anisotropy via altering the  $\epsilon_4$  amplitude parameter in the expression of anisotropy function [Eq. (3.6)]. The results are shown in Fig. 5.9 (a). Increasing the anisotropy yields a decreasing tip radius, in other words, the dendrites become sharper as the anisotropy gets stronger. The variation of the kinetic anisotropy influences the shape of the cross-section in the direction of the fins. The exponent  $\nu$ , describing the shape of the dendrite tip, has been obtained by fitting the expression  $z = z_{\text{max}} - |x|^\nu$  to the longitudinal cross section of the dendrite, where  $z_{\text{max}}$  is the tip position and  $x$  is the distance from the axis of the dendrite.

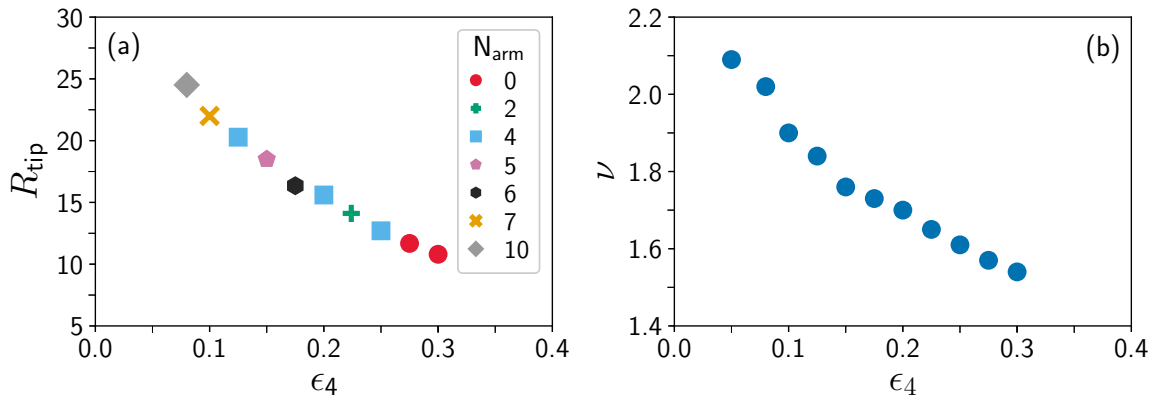


**Figure 5.9.** The effect of kinetic anisotropy ( $\epsilon_4$ ) on the shape of the two-phase dendrite. (a) Tip radius vs. kinetic anisotropy at  $\gamma_{\text{SL},0} = 0.0295$ . (b) Exponent  $\nu$  (describing the shape of the dendrite tip) vs. kinetic anisotropy. The dendrites become sharper as the kinetic anisotropy increases.

The exponent  $\nu$  changes from  $\sim 1.5 \pm 0.1$  to  $\sim 2.1 \pm 0.1$  with decreasing anisotropy [see Fig. 5.9 (b)]; i.e. it varies roughly between the experimental value for xenon (1.67) and the rotational paraboloid (2.0) expected for isotropic case. This is combined with a change of the shape of transverse section from a square of rounded corners to a circle. Apparently, there is a correlation between the tip radius and the number of spiral arms: the probability of having larger number of spiral arms increases with increasing tip radius. The reason for observing  $\nu > 2$  is probably finite-size effect: the boundary of the simulation box may influence the dendrite shape far from the tip region.

### 5.3.6 Eutectic wavelength vs. tip radius

The other assumption of Ref. [72] that the tip radius and the eutectic wavelength are proportional, i.e.  $\lambda \propto R_{\text{tip}}$  is satisfied, provided that the other parameters are kept constant. Fig. 5.10 (a) shows the eutectic wavelength as a function of the tip radius for three sets of simulations (same as in Fig. 5.7), where the pulling velocity was varied.

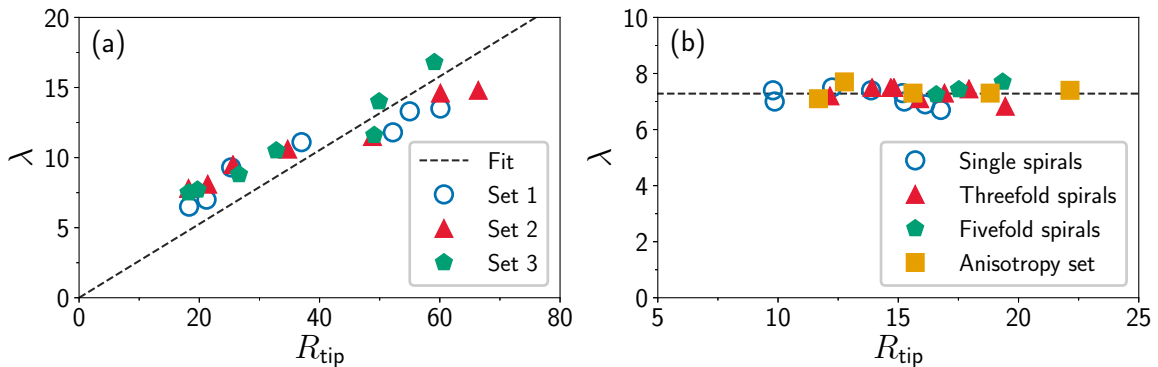


**Figure 5.10.** Eutectic wavelength vs. tip radius. (a) Pulling velocity is varied, while other parameters are fixed. Different symbols stand for sets of simulations with different initial patterns. (b) Varying the interface free energy  $\gamma_{\text{SL},0}$  or the kinetic anisotropy  $\epsilon_4$  while keeping the velocity constant. Here circles, triangles and pentagons indicate the number of spiral arms observed in simulations where  $\gamma_{\text{SL},0}$  was varied, while squares stand for results from simulations where the kinetic anisotropy  $\epsilon_4$  was varied. In the experiments  $\gamma_{\text{SL},0}$  and  $\epsilon_4$  are fixed, under such conditions the two characteristic lengths are roughly proportional to each other,  $\lambda \propto R_{\text{tip}}$ , as assumed in Ref. [72]. The dashed lines are to guide the eye. The standard deviation is  $\pm 0.4$  for the tip radius and  $\pm 0.9$  for the eutectic wavelength.

In our simulations, the proportionality coefficient  $\lambda = (0.26 \pm 4.5\%)R_{\text{tip}}$  is smaller than in the experiments  $\lambda \approx 1.33R_{\text{tip}}$  [72]. However, the ratio can be tuned via chang-

ing the interface free energy or the kinetic anisotropy. If the velocity is kept constant and either the interface free energy is increased or the kinetic anisotropy decreased, the tip radius increases, whereas the eutectic wavelength remains roughly constant [Fig. 5.10 (b)]. Accordingly, one could move towards the experimental conditions via decreasing the interface free energy or increasing the kinetic anisotropy.

The finding that  $\lambda \approx \text{const.}$  follows from the fact that in the present model the free energy of the solid-solid interface,  $\gamma_{\alpha\beta}$ , is independent of the solid-liquid interface free energy,  $\gamma_{\text{SL}}$ . At the trijunction the Young's law relates these interface energies to the contact angles as [74]:

$$\gamma_{\alpha\beta} = \gamma_{\alpha L} \sin \theta_{\alpha} + \gamma_{\beta L} \sin \theta_{\beta}, \quad (5.1)$$

where in our symmetric model system the properties of the  $\alpha$  and  $\beta$  phases are identical, including the contact angles:  $\theta_{\alpha} = \theta_{\beta}$ , and the solid-liquid interface free energies:  $\gamma_{\alpha L} = \gamma_{\beta L} = \gamma_{\text{SL}}$ . Furthermore the eutectic wavelength is expressible as follows [74]:

$$\lambda_{\text{JH}} = \sqrt{2l_D [(1 - \eta)d_{\alpha} \sin \theta_{\alpha} + \eta d_{\beta} \sin \theta_{\beta}] / P(\eta)}, \quad (5.2)$$

where  $d_{\alpha} = d_{\beta} = \gamma_{\text{SL}}T_E / (L|m|\Delta C)$  are the (in our case equal) capillary lengths of the two solid phases,  $L$  is the heat of fusion,  $m$  is the slope of the liquidus,  $\Delta C$  is the concentration difference between the solid solutions, whereas the volume fraction of the  $\alpha$  phase is  $\eta = 0.5$  in our symmetric model, and  $P(\eta) = \sum_{n=1}^{\infty} [\sin^2(\eta\pi n) / (\pi n)^3]$ . Considering these and inserting Eq. (5.1) into Eq. (5.2), we found the following relation:

$$\begin{aligned} \lambda_{\text{JH}} &= \sqrt{l_D (d_{\alpha} \sin \theta_{\alpha} + d_{\beta} \sin \theta_{\beta}) / P(0.5)} \\ &= \sqrt{l_D \gamma_{\alpha\beta} T_E / (P(0.5) L |m| \Delta C)} = \text{const.} \end{aligned} \quad (5.3)$$

This is the reason why  $\lambda$  remained constant in Fig. 5.10 (b) while the  $\gamma_{\text{SL}}$  was changed: in our model, the solid-solid interface free energy ( $\gamma_{\alpha\beta}$ ) has a fixed value, variation of solid-liquid interface free energy ( $\gamma_{\text{SL}}$ ) must be compensated by a change of the contact angles, so Eq. (5.3) is maintained.

## 5.4 Eutectic patterns

At the beginning of this chapter, the evolution process of a *single spiral* has been shown in Fig. 5.1. However, beside the single spiral, additional patterns have also been found, including the *target pattern* and multiarm spirals (double, threefold, fourfold, etc.). In this section, the formation of two-phase patterns on the surface of eutectic dendrites will be discussed in detail.

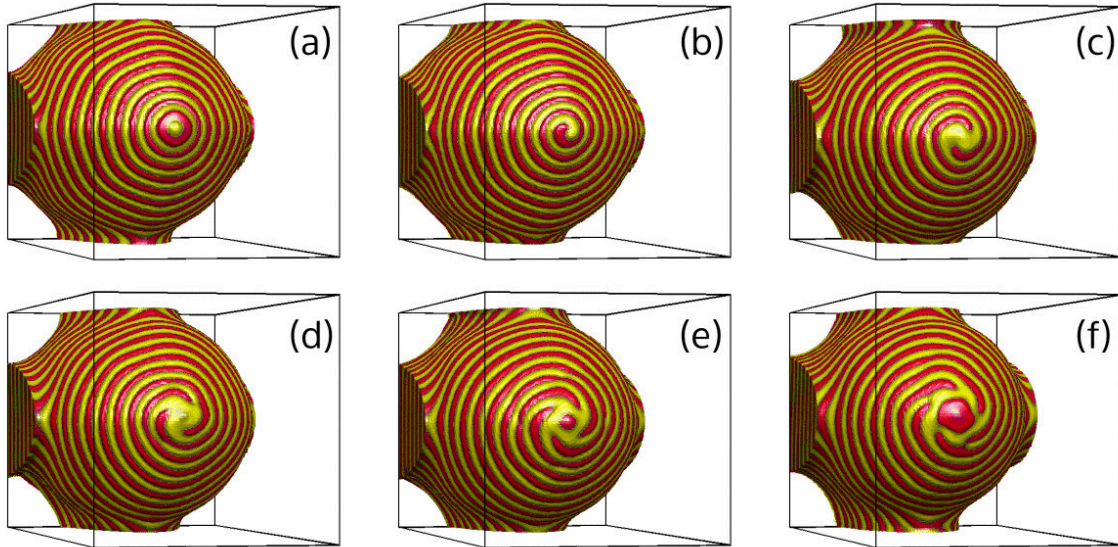


**Figure 5.11.** Eutectic patterns observed during the simulations with different solid-liquid interfacial free energy. (a) Target pattern, (b) single- and (c)-(f) multiarm spiral motifs. For better comparison, only spirals with clockwise rotating pattern were selected, the rotation direction in the simulations is random.

The *target pattern* [Fig. 5.11 (a)] looks like concentric rings of the two phases with increasing radius. This pattern forms via alternating nucleation of the two solid phases on top of each other, confining the occurrence of this mode to larger undercoolings.

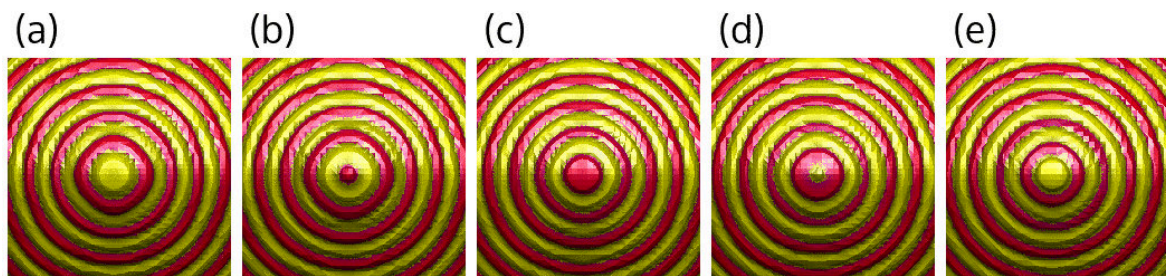


**Figure 5.12.** Growth process of a dendrite having the target pattern. The time increases from left to right by  $4 \times 10^3$  time steps.

■ Video 5.12: <https://rlphd.phasefield.hu/s0>



One full cycle of the growth process can be seen in Fig. 5.12. The  $\beta$  solid phase on the top forms a homogeneous disk [panel (a) of Fig. 5.12] until its diameter becomes about the  $\lambda$  eutectic wavelength, when the  $\alpha$  phase nucleates on top [panel (b)] and the cycle starts over now with the  $\alpha$  phase [panels (c)-(e)]. Similar structure has been observed in [27].

In contrast to the target pattern, no nucleation is required for the formation of *single-* and *double spirals*, in which the eutectic pattern originates from alternating occupation of the tip region by the two solid phases. In the case of a single spiral, the growth process can be seen in Fig. 5.13. Both solid phases can grow simultaneously, which appears as a rotation around each other on the surface of the dendrite creating a similar scenario to coupled lamellar eutectic growth shown in Fig. 2.16 of Section 2.3.3.

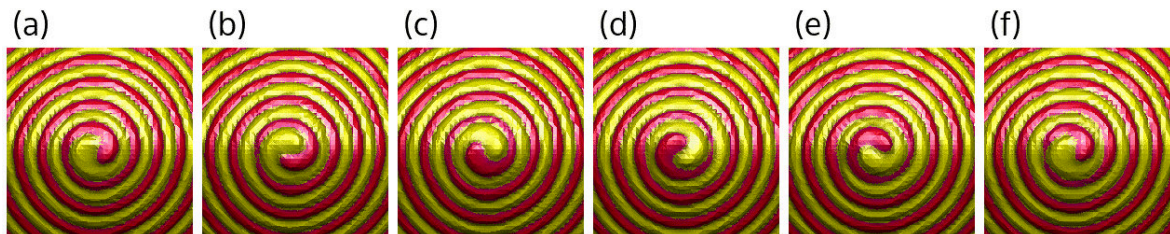


**Figure 5.13.** A full rotation cycle during the growth of a single spiral dendrite. The time increases from left to right by  $4 \times 10^3$  time steps.

🎬 Video 5.13: <https://rlphd.phasefield.hu/s1>

In the case of double spiral the growth (Fig. 5.14) happens so that the  $\alpha$  and  $\beta$  phases remain spatially continuous: Having a growing  $\beta$  region at the tip [panel (a) of Fig. 5.14], the  $c_1$  component piles up ahead of the tip slowing down the growth of the  $\beta$  and accelerating the growth of the  $\alpha$  phase [panel (b)], that now grows over the  $\beta$  region creating the double spiral motif on the surface [panel (c)]. This is followed

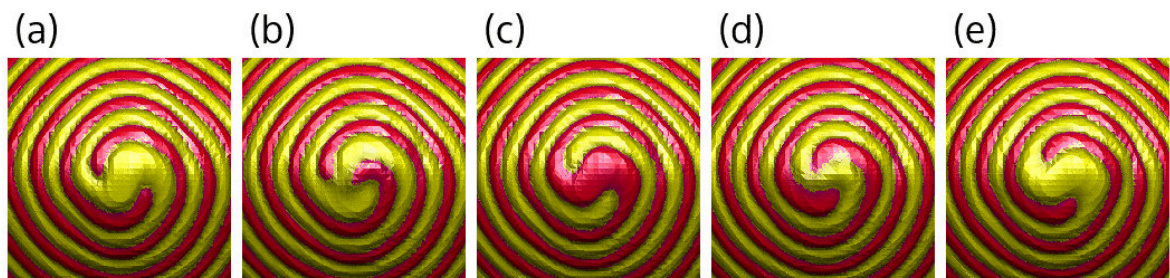


**Figure 5.14.** Growth process of a double spiral. The time increases from left to right by  $4 \times 10^3$  time steps.

🎬 Video 5.14: <https://rlphd.phasefield.hu/s2>

by the same process, but now for the  $\beta$  phase [panels (d)-(e)]. Since in this way the formation of spiral arms (single or double) does not need nucleation, these mechanisms can prevail at small undercoolings.

The growth modes with larger number of spiral arms ( $N_{\text{arm}} \geq 3$ ) become increasingly more complex, still displaying alternating phase appearance at the tip. The spiral arms usually do not join to each other directly in one specific center point (like the lines in an asterisk symbol: \*), but they connect to a homogeneous disk having 1-2 times the wavelength diameter, which nucleated on top of the other solid phase at the tip. This growth process for a fivefold spiral can be followed in Fig. 5.15. First, the  $\alpha$  phase nucleates at the tip [panel (a) of Fig. 5.15], which then begins to grow [panel (b)], until it becomes so large that the spiral arms start to connect to it [panel (c)]. Simultaneously with the arm-joining process of  $\alpha$  phase, the other solid phase,  $\beta$ , nucleates on top and forms a disk [panels (c) and (d)]. Shortly after all of the spiral arms of  $\alpha$  phase connect to the central disk [panel (d)], the same process starts for the  $\beta$  phase [panel (e)] and so on. The larger the number of spiraling arms, the more disordered tip region forms, e.g. the spiral arms rarely connect at the same time to the center disk. As a result, larger numbers of point- and line defects appear and travel down on the surface of the dendrite (see Section 5.4.3). This is especially so for the simulations performed with noise in the concentration fields.

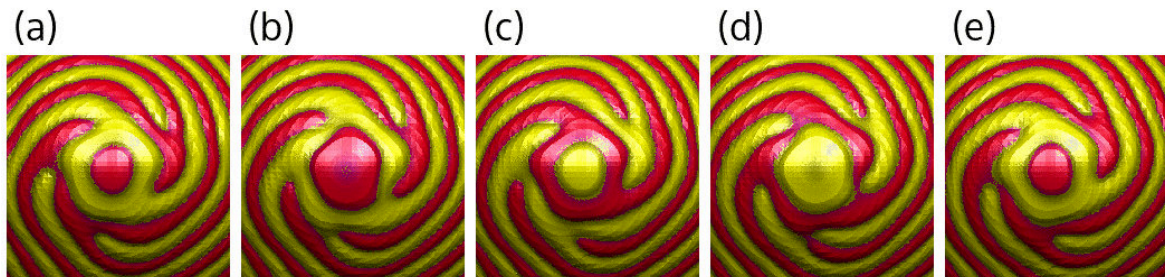


**Figure 5.15.** Growth process of a fivefold spiral. The time increases from left to right by  $4 \times 10^3$  time steps.

■ Video 5.15: <https://rlphd.phasefield.hu/s5>

The internal structure of eutectic dendrites with the target pattern, and the single-, triple- and five-arm spiraling modes are presented in Fig. 5.16. Apart from periodically occurring defect-rich regions, the target pattern is composed of conical domains of the two phases, where the domains of the same phase are not connected spatially, i.e.

alternating nucleation of the two phases is needed to create them, as it was shown in Fig. 5.12. In contrast, the inner structures corresponding to the single or multiple spirals on the surface are single or multiple helical structures, where the  $\alpha$  and  $\beta$  domains are connected. The longitudinal sections of the two-phase dendrites are fairly similar for all these modes, although weak systematic differences can be observed [(e) column]. More characteristic are the front views and the transverse sections: The individual eutectic growth modes (number of spiral arms) can clearly be distinguished [(a)-(d)]. It has been observed that in the appropriate parameter domain, the spiraling two-phase dendrites are quite robust.

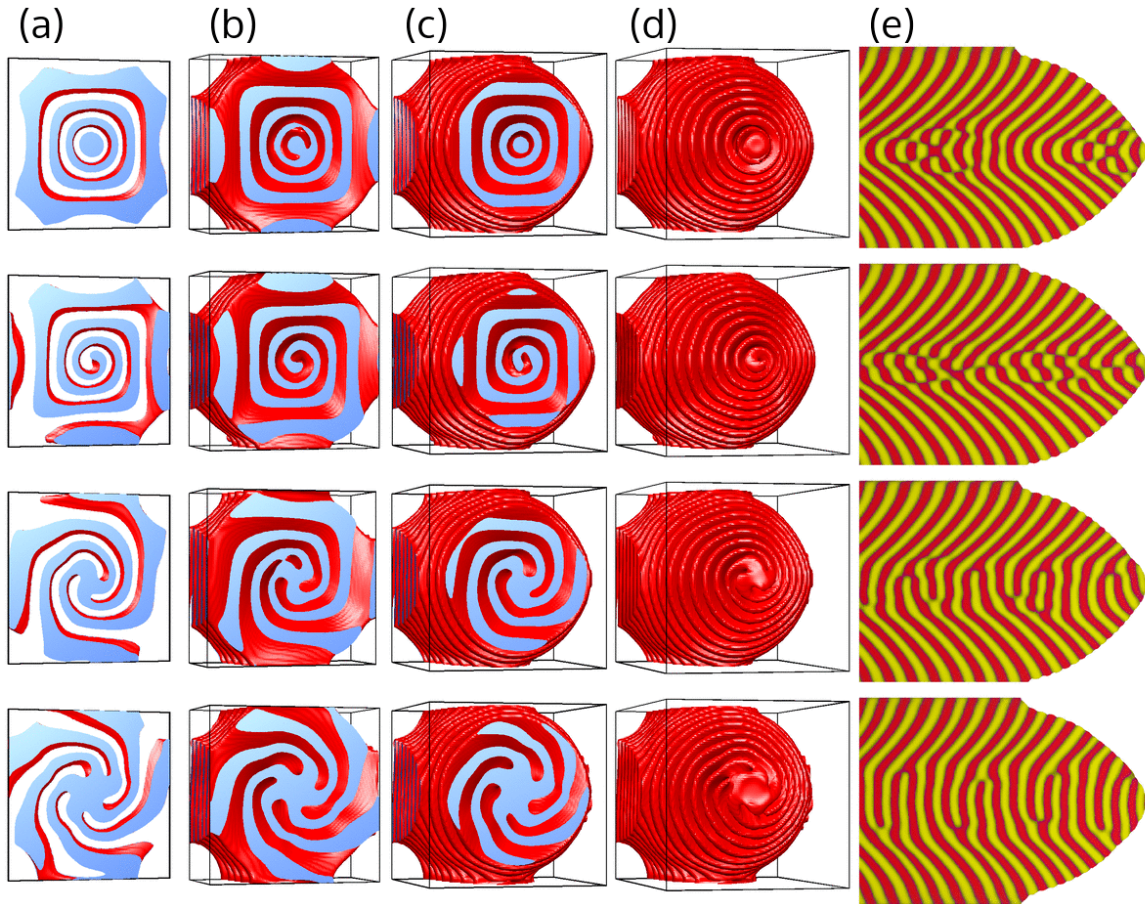


**Figure 5.16.** Dendrite cross sections for the target, single-, triple- and five-arm cases shown in Fig. 5.11. (a)-(c) columns: one phase  $x-y$  plane frontal view, the box cut at  $z = 3, 50$  and  $100$ , respectively, perpendicular to  $z$  axis. The cut surfaces were colored with blue for better contrast. (d) column: helical structure formed by one of the spiraling phases. The phases inside the spiraling eutectic structures are connected. (e) column:  $y-z$  plane (parallel to the temperature gradient) cross sections.

### 5.4.1 Pattern selection

As seen earlier in Fig. 5.8, the number of spiral arms ( $N_{\text{arm}}$ ) tends to increase with increasing solid-liquid interfacial free energy ( $\gamma_{\text{SL},0}$ ), which in turn is reflected in the increasing tip radius. In a set of simulations (colored symbols in Fig. 5.8) the same initial eutectic pattern was used with varying  $\gamma_{\text{SL},0}$ . To investigate further how the steady-state pattern depends on the initial configuration, 8 values of interfacial free energy were selected, where 20 additional simulations with different initial random pattern were performed each (black dots in Fig. 5.8). The results (see Fig. 5.17) showed that at a value of  $\gamma_{\text{SL},0}$  different steady-state patterns can be obtained if different initial patterns are used. For example at  $\gamma_{\text{SL},0} = 0.059$ , these patterns include the target pattern together with single- to fivefold spirals. This indicates that there is a multiplicity of the possible steady-state solutions for the same physical conditions from which the random initialization chooses. This stochastic behavior is characterized by a peaked probability distribution of  $N_{\text{arm}}$  (plotted in Fig. 5.17), which shows that the number of spiral arms increases in a statistical manner with the increasing solid-liquid interfacial free energy (and therefore tip radius).

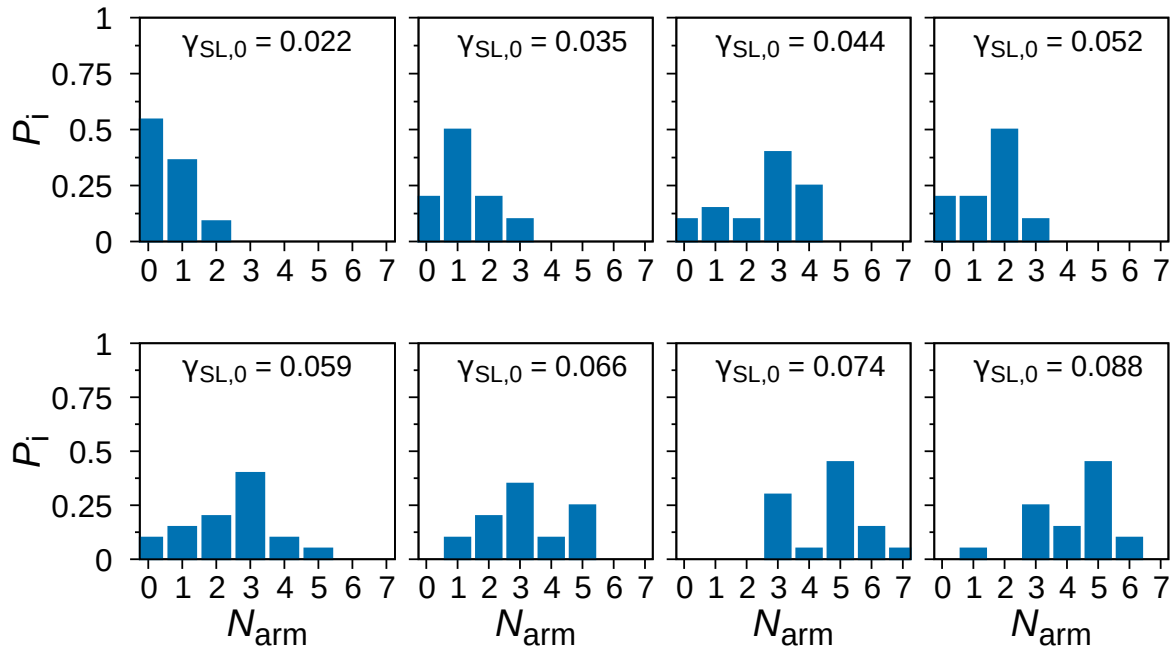


**Figure 5.17.** Probability distributions of the number of spiral arms of steady-state eutectic patterns at 8 different values of solid-liquid interface free energy. Each histogram is based on 20 simulations started from different initial eutectic pattern.

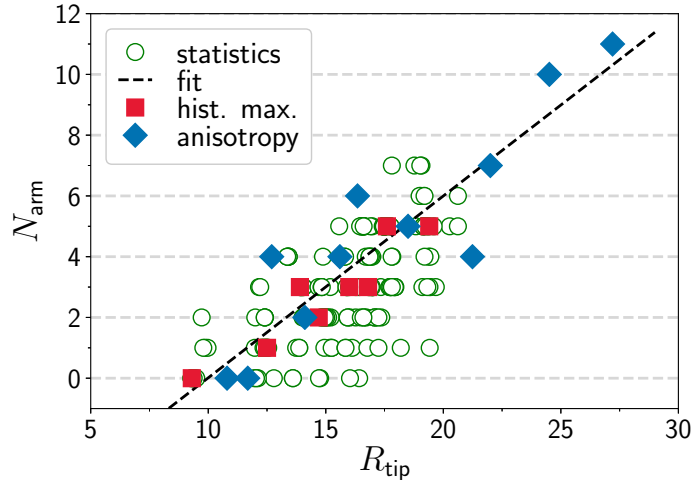


**Figure 5.18.** Number of spiral arms vs. tip radius. Empty (green) circles: results from random initial eutectic patterns at  $\epsilon_4 = 0.3$  ( $8 \times 20$  simulations, whose histograms are shown in 5.17). Red squares: the most likely eutectic patterns from those 20 random initializations (peak positions in Fig. 5.17). Blue diamonds: same initialization, but  $\epsilon_4$  varies between 0.3 and 0.05 (Fig. 5.9).

The number of spiral arms as a function of tip radius for these large number of simulations is shown in Fig. 5.18. The most likely value of  $N_{\text{arm}}$  for a specific  $\gamma_{\text{SL},0}$  and a set of simulations where the  $\epsilon_4$  anisotropy parameter has been varied between 0.3 and 0.05 are also illustrated. This figure shows that  $N_{\text{arm}}$  is increasing with the tip radius, which is reasonable since the eutectic wavelength (i.e. the width of the spiral arms) remains constant, while the tip region of the dendrites becomes more flat, therefore more spiral arms can be formed.

Apparently, there are multiple steady-state solutions for a given set of operating parameters, from which the fluctuations choose during the growth. These features closely resemble the behavior reported for Liesegang patterns, where the fluctuations determine, which of the competing modes (rings, single-, double-, triple- and multiple helices, or disordered patterns) is realized [8, 15].

In all simulations presented until now, stochasticity was incorporated into the simulations by using a random initial composition pattern. In order to check the validity of the assumption that just using a random initialization can reasonably represent the effect of compositional fluctuations during the whole growth process, 20 additional simulations were performed at  $\gamma_{\text{SL},0} = 0.059$ , starting from a single-phase crystal seed [Fig. 4.6 (a) starting configuration] while adding flux noise to the EOMs for the con-

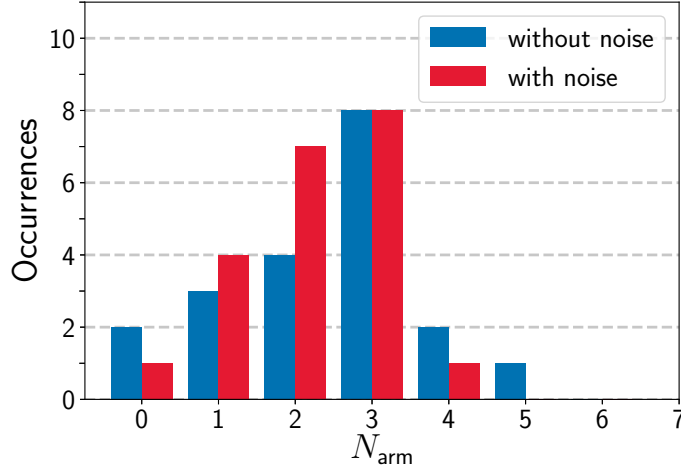


**Figure 5.19.** Distributions for the accessible eutectic patterns differing in the number of spiral arms obtained on the basis of 20 simulations. Blue: started from random initial eutectic patterns without noise. Red: started from a single-phase seed while applying flux noise in the EOMs for the concentration fields. The individual runs differed in the initialization of the random number generator.

centration fields as in [75]. These 20 simulations differed in only the initialization of the random number generator. Such simulations are rather time consuming since growth from the seed to the steady-state dendrite has to be covered, and the additional chemical flux noise also slows down the simulation process.

The probability distributions of  $N_{\text{arm}}$  obtained from a set of simulations with this method are compared to the distribution obtained from computations with random initial two-phase patterns in Fig. 5.19. Considering the scattering of the results due to the relatively small number of simulations limited by the available computational power, a reasonable agreement can be seen between the two types of probability distributions. This justifies the use of the faster method in most of our simulations.

### 5.4.2 Rotation direction

One of the components of the pseudo-ternary alloy used in Ref. [16] is a chiral molecule, but in spite of this, both left- and right-handed spirals have been observed in the experiments. Since in the simulations the chirality of the components was not taken into account, the rotation direction of the spirals is expected to be random. Evaluating the spirals from the previous  $\gamma_{\text{SL},0}$ -changing set (Fig. 5.17), it was found that the probability of clockwise and counterclockwise spirals within 20 simulations (started

with different initial eutectic pattern) is fairly close to 50% – 50% (see Fig. 5.20).

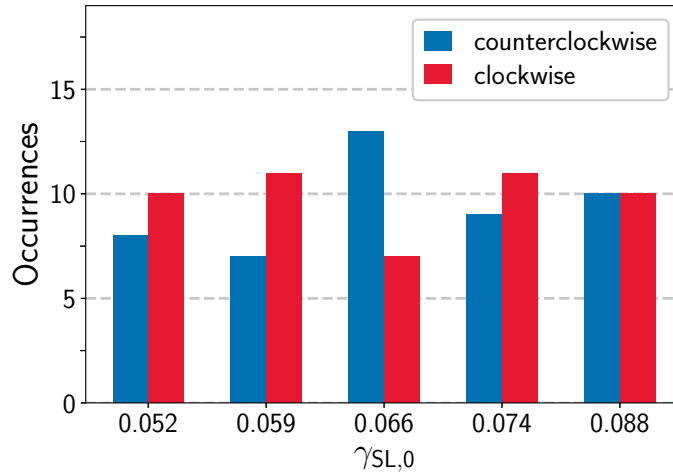


**Figure 5.20.** Randomness of rotation direction. Evaluated from 20 simulations of 5 different  $\gamma_{SL,0}$  values whose histograms were plotted in Fig. 5.17. (The target pattern was excluded.)

### 5.4.3 Defects in the spiraling eutectic patterns

Not every spiraling dendrite develops such regular patterns as in Fig. 5.11, where each lamella is defect-free and the number of spiral arms can be obviously determined just by looking at the tip region. Many of them have different amount of various defects and irregularities even after the standard duration of simulation ( $4 \times 10^6$  time steps), which is usually sufficient time for the regular spiraling dendrites to form a defect-free pattern. In Fig. 5.21 two examples are shown. In panel (a) there is an almost regular fourfold spiral dendrite, where one of the lamellae of the  $\beta$  phase has disjointed, therefore the lamellae of the other solid phase are connected forming a horizontal H-shaped defect. This kind of defects are morphologically very similar to the ones presented in Fig. 5 of [76]. However they are not in steady-state, as the eutectic pattern advances, these defects change as well; e.g. one disappears, a new one forms, or changes the disjoint phase. In panel (b) a lamella splitting/merging can be seen at the top region of the dendrite. This defect can move downwards, as the spiraling pattern makes a rotating cycle, via splitting from and joining to a neighboring lamella of the same phase. The pattern on the surface of the dendrite, where the lamellae have stair-like deformations, is the results of movement of the defect.

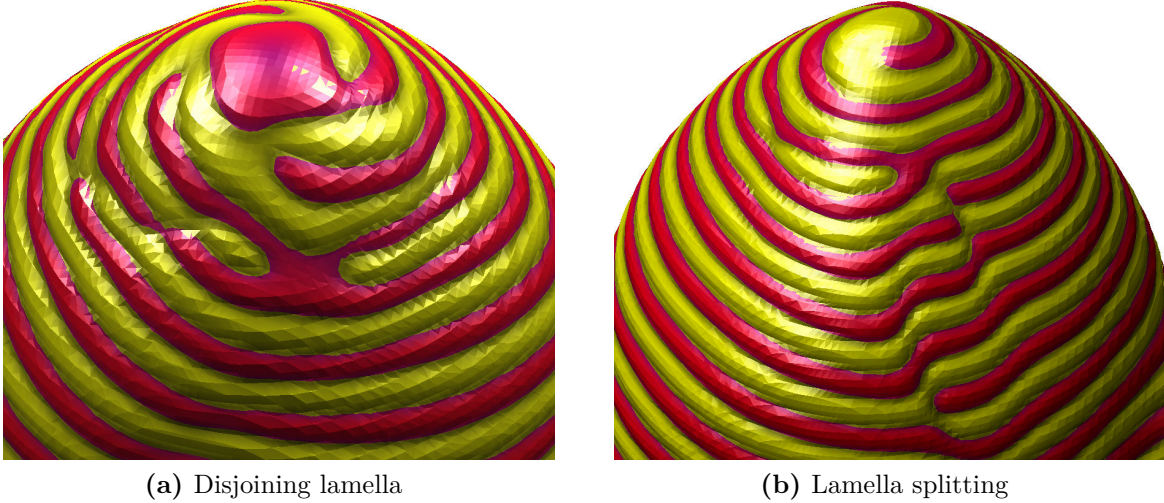


**Figure 5.21.** Defects in the spiraling eutectic patterns. (a) Disjoining lamella in a fourfold spiral pattern. (b) A lamellae splitting defect that moves downwards as the dendrite grows. The pattern on the surface, where the lamellae have step-like deformations, is the results of the movement of the defect. Both snapshots are taken at the  $4 \times 10^6$ th time step in a reference sized ( $96 \times 96 \times 612$  grid) simulation.

## 5.5 Significance of the presence of anisotropy in the spiral growth

One of the most interesting conclusions of the work of Akamatsu *et al.* [72] is that unlike in the case of single-phase dendrites, where the presence of anisotropy is a pre-condition of dendritic growth [77–84], it is expected that in the case of spiraling ternary eutectic dendrites, dendritic growth is possible without anisotropy. They claim that the spiral mechanism itself makes a steady-state two-phase dendritic growth possible along the curved solid-liquid interface, and therefore no anisotropy effects are required. Unfortunately, this statement is hard to check experimentally, since one cannot turn off the anisotropy of the phases.

In order to test this expectation, large isotropic ( $\epsilon_4 = 0$ ) simulations have been performed along with their anisotropic counterparts. Two pulling speeds have been used: the reference one ( $v_{\text{pull}} = 0.2$ ) and a slower one with half of the reference speed. To minimize finite-size effects that, in principle, might help in forming to the realization of the two-phase dendrites, the cross-section of the simulations has been chosen as large as possible ( $380 \times 380 \times 511$  grid) while keeping the computational time at a reasonable



level. The simulations were started from 25 randomly positioned single-phase seeds.

### 5.5.1 Eutectic colonies and cells

Performing the simulation without anisotropy at  $v_{\text{pull}} = 0.1$  (see Fig. 5.22), the growing eutectic particles impinge upon each other, and after a transient period of frustrated eutectic patterns, the solid-liquid interface forms a 3D disordered cellular morphology

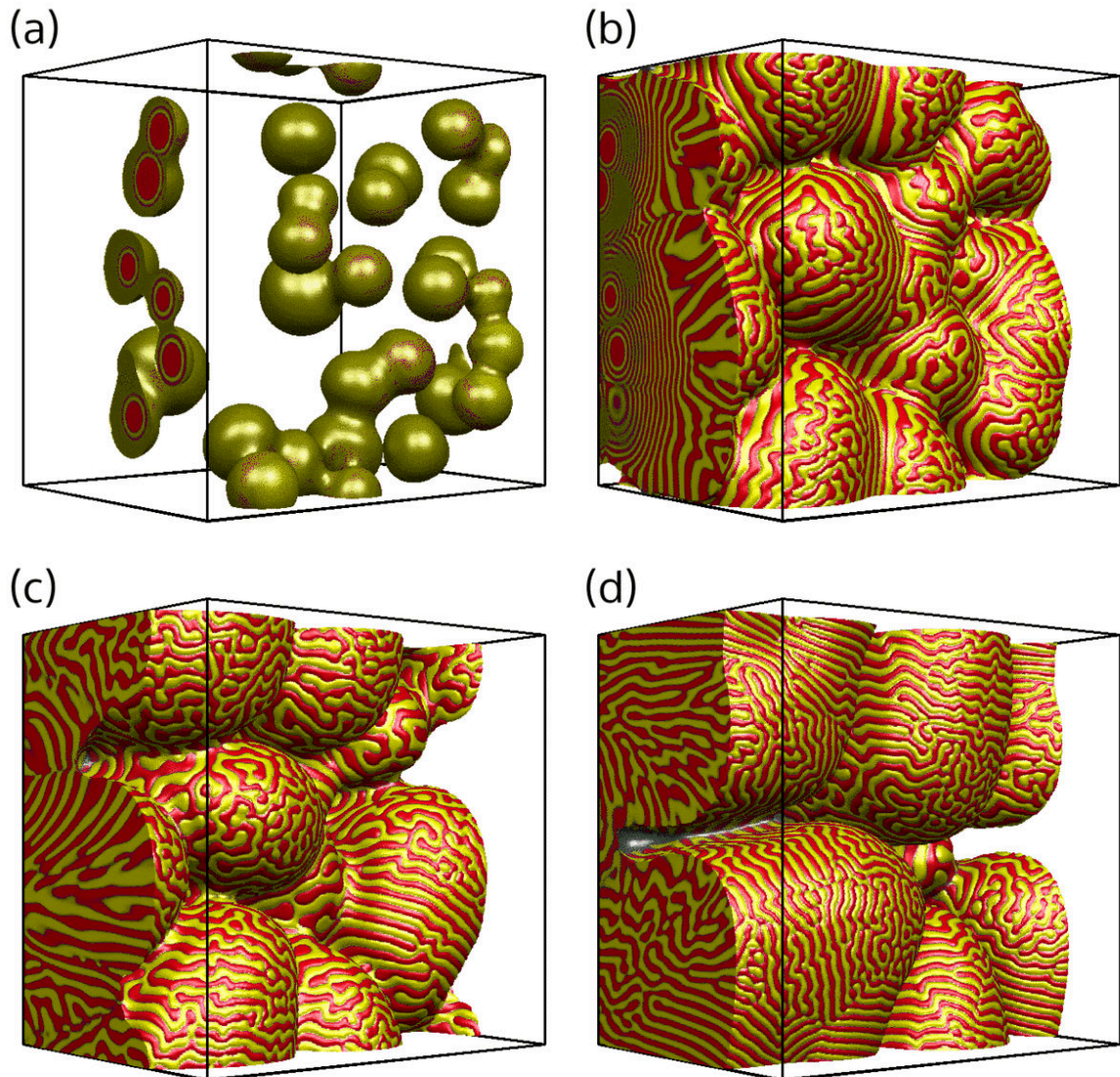


**Figure 5.22.** Formation of eutectic colonies started from 25 single-phase seeds performed at  $v_{\text{pull}} = 0.1$  without anisotropy in a large scale simulation ( $380 \times 380 \times 511$  grid). Snapshots have been taken at  $10^4$ ,  $6.2 \times 10^5$ ,  $1.6 \times 10^6$ , and  $4.0 \times 10^6$  time steps. Competing cellular structures evolve after a transient period, and the cellular structure dynamically changes with time.

Video 5.22: <https://rlphd.phasefield.hu/iso-slow>

with dynamically appearing and disappearing tips and ridges of rather flat end, covered by a disordered lamellar eutectic pattern with lamellae perpendicular to the solid-liquid interface. These structures are well-known as eutectic colonies seen in ternary systems experimentally [85] and in simulations [86, 87].

Using the same conditions and initialization but with the reference anisotropy ( $\epsilon_4 = 0.3$ ), the growth is quite similar to the isotropic case until the end of the transient period of frustrated eutectic patterns (Fig. 5.23). After that, a couple of large eutectic cells remain in the system along with a few smaller ones which disappear shortly after.

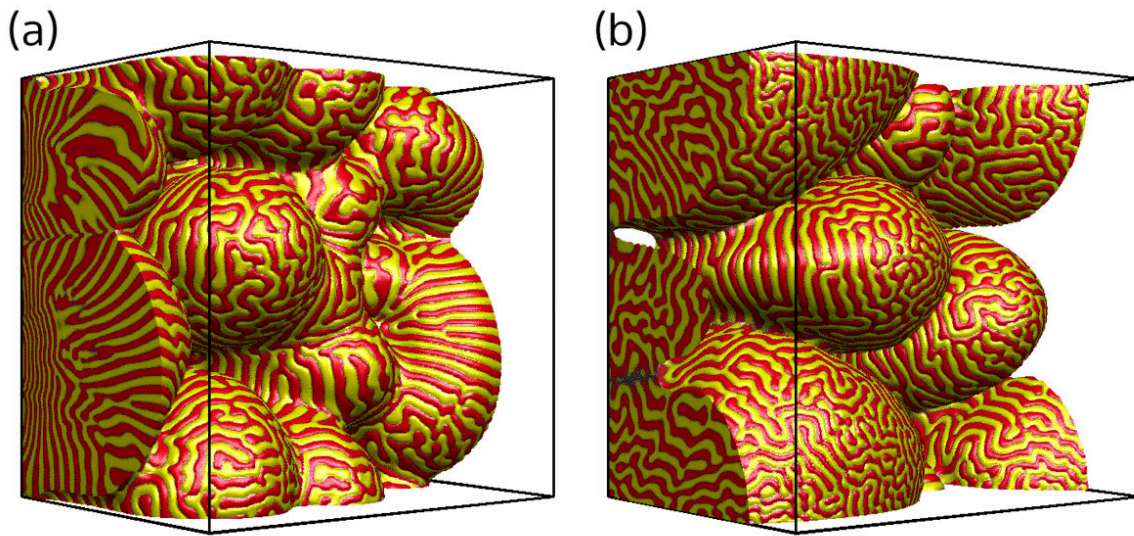


**Figure 5.23.** Formation of eutectic cells in a large scale simulation ( $380 \times 380 \times 511$  grid) performed at  $v_{\text{pull}} = 0.1$  pulling speed with kinetic anisotropy. The snapshots were taken at the (a):  $8.5 \times 10^5$ th and (b):  $4 \times 10^6$ th time step. The solidification was started from 25 single-phase seeds.

■ Video 5.23: <https://rlphd.phasefield.hu/aniso-slow>

The difference between the two cases can be easily seen in a top view snapshots of the simulation boxes (Fig. 5.24). Without anisotropy [in panel (a)], the eutectic structures fill all the accessible space until they meet each other, and the enrichment of the  $c_3$  component between the ridges prevents further expanding. In contrast, in the anisotropic case, the eutectic structures have distinct, cellular shape.

As expected, neither of the two cases shows spiraling eutectic pattern at this lower pulling velocity. The two solid phases form a random, labyrinth-like, unordered lamellar eutectic pattern on the surface of the structures.

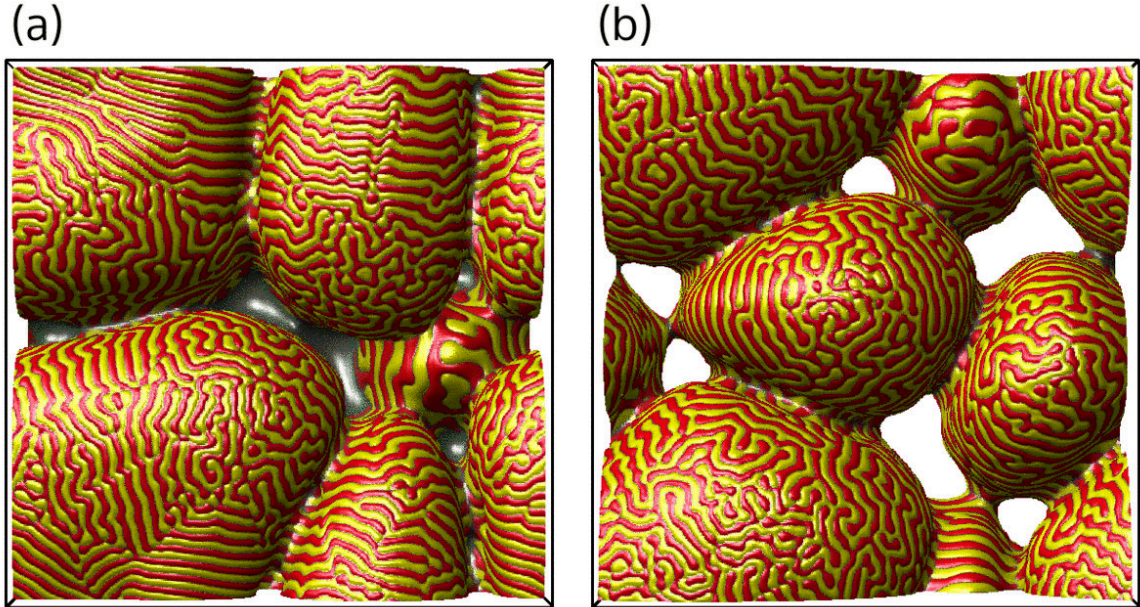


**Figure 5.24.** Top view of eutectic colonies (a) formed without anisotropy and (b) cells formed with anisotropy in a large scale simulation ( $380 \times 380 \times 511$  grid). Both snapshots were taken at  $4 \times 10^6$ th time step. It should be noted, that the large object in the bottom left corner of (a) will probably split into two smaller, more cellular-like stable structures after a long transient period.

### 5.5.2 Stabilizing effect of the anisotropy

The difference between the isotropic ( $\epsilon_4 = 0$ ) and anisotropic ( $\epsilon_4 = 0.3$ ) cases is more noticeable at the reference  $v_{\text{pull}} = 0.2$  pulling speed (see Fig. 5.25). In the anisotropic simulation (right column of Fig. 5.25), four well-defined steady-state dendrites form in the system. In contrast, in the isotropic case (left column of Fig. 5.25), many, varying shaped eutectic fingers can be found in the simulation. These eutectic fingers, though some of them show a (temporary) spiraling pattern, are not steady-state structures; the larger flat tips tend to undergo tip splitting, and the smaller ones occasionally get eliminated during the solidification. These are similar to the dynamic tip splitting and cell elimination processes shown by quantitative phase-field modeling of cellular growth in binary alloys of low anisotropy [88, 89]. As a consequence, the shape of the solidification front is changing continuously; a stable dendritic structure cannot form in the isotropic system. To illustrate the dynamic behavior of the solidification front, snapshots taken at each  $10^6$ th time steps are shown in Fig. 5.26. Between two snapshots, each eutectic finger changed its shape (or even disappeared completely from the system).

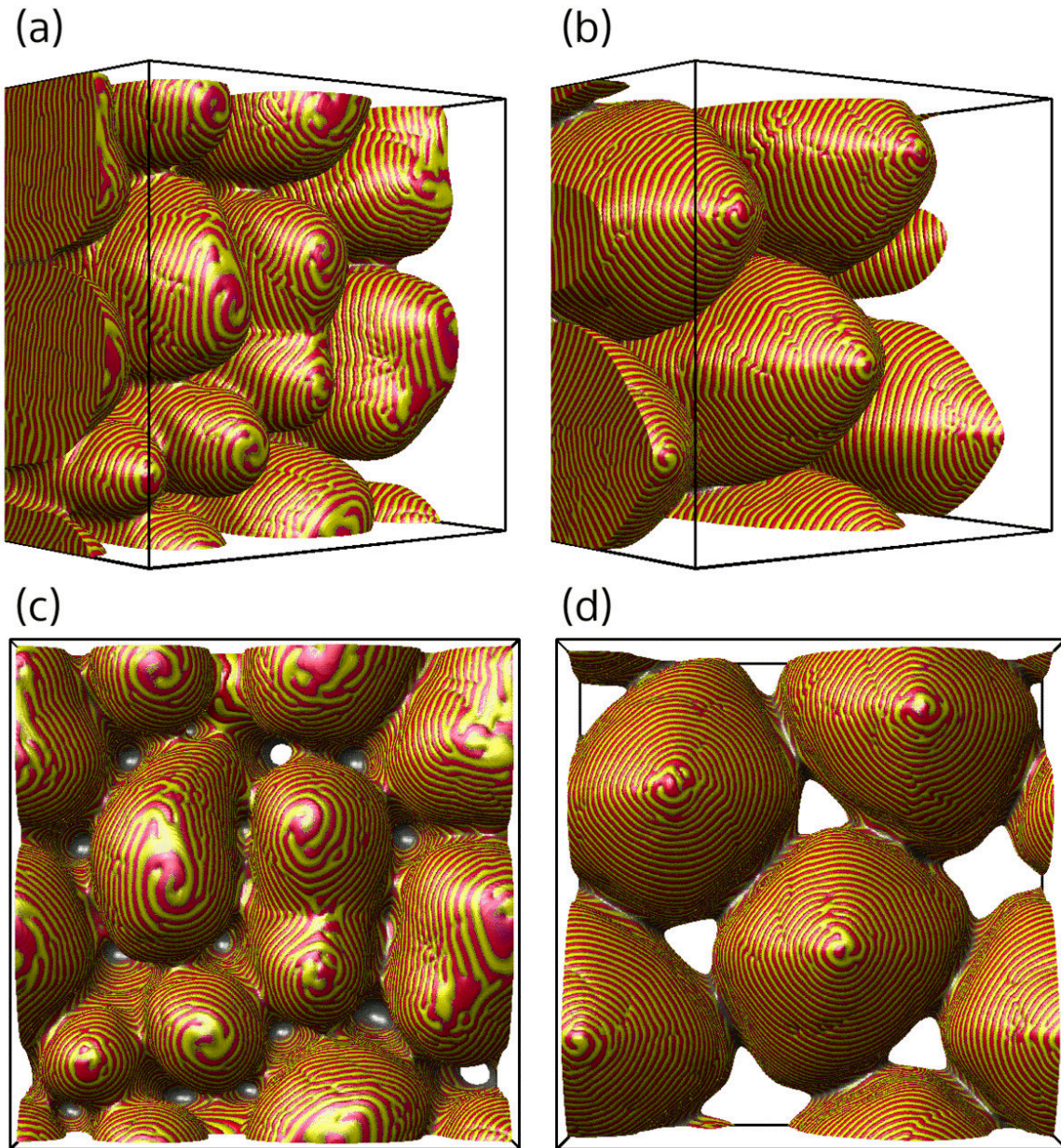


**Figure 5.25.** The effect of anisotropy on the eutectic morphology grown from 25 single-phase seeds in large scale simulations ( $380 \times 380 \times 511$  grid) performed at  $v_{\text{pull}} = 0.2$ . (a) and (c): without anisotropy random eutectic cellular structure emerges, that continuously changes with time (tilted frontal and top views). (b) and (d): with anisotropy ( $\epsilon_4 = 0.3$ ) steady-state spiraling eutectic dendrites evolve, caused by the included kinetic anisotropy (tilted frontal and top views). The snapshots were taken at the  $3 \times 10^6$ th time step for the isotropic and at the  $3.2 \times 10^6$ th time step for the anisotropic case.

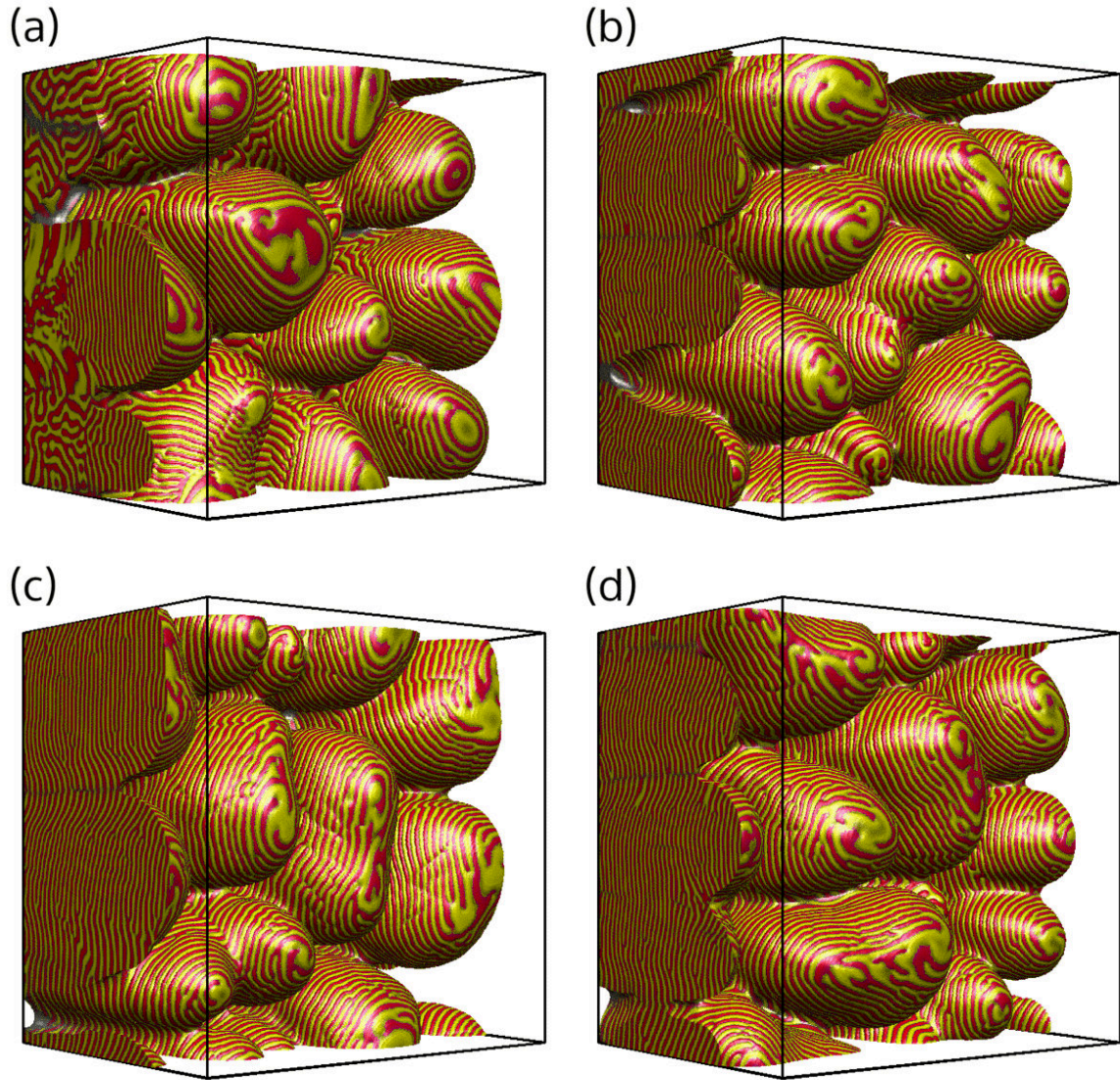


**Figure 5.26.** Formation of eutectic fingers in a large isotropic simulation ( $380 \times 380 \times 511$  grid) performed at  $v_{\text{pull}} = 0.2$ . Panels (a)-(d) display snapshots taken at  $1 \times 10^6$ ,  $2 \times 10^6$ ,  $3 \times 10^6$ , and  $4 \times 10^6$  time steps, respectively.

🎥 Video 5.26: <https://rlphd.phasefield.hu/iso>

An example of tip elimination is shown in Fig. 5.27. The pictures focus on a tip and its adjacent region in the large isotropic simulation. First the growth of the tip starts to slow down [panel (b)], while the eutectic pattern on the surface keeps rotating. This slowing down can be caused by e.g. a more dominant (larger) neighboring tip, which increases the concentration of the  $c_3$  component ahead of the tip being investigated, therefore the growth slows down. At some point the tip becomes almost flat, while the rotation of eutectic pattern also slows down, then stops entirely [panel (c)]. As a result, the remainings of the tip disappear entirely from the system and adjacent tips

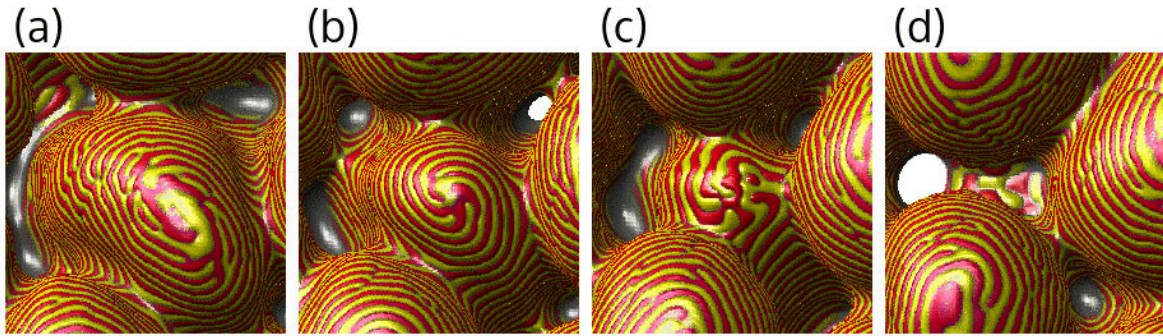


**Figure 5.27.** Tip elimination process in a large ( $380 \times 380 \times 511$  grid) isotropic simulation. The snapshots show only part of the simulation box focusing on a disappearing tip. (a) A developed solid tip, surrounded by other tips and ridges. (b) The tip becomes smaller, meanwhile the eutectic pattern on the surface is still rotating. (c) The tip is almost flat and the pattern stops rotating. (d) The tip is completely eliminated, the surrounding solid occupies the available space. [Panels (a)–(d) display snapshots taken at  $2.28 \times 10^6$ ,  $2.52 \times 10^6$ ,  $2.68 \times 10^6$ , and  $3.04 \times 10^6$  time steps, respectively.]

take the freed space.

A tip splitting process is shown in Fig. 5.28. First, an eutectic finger in the center of the image becomes large enough to form a second peak. This can be induced by e.g. a decaying adjacent tip, since without anisotropy the solid structures tend to occupy

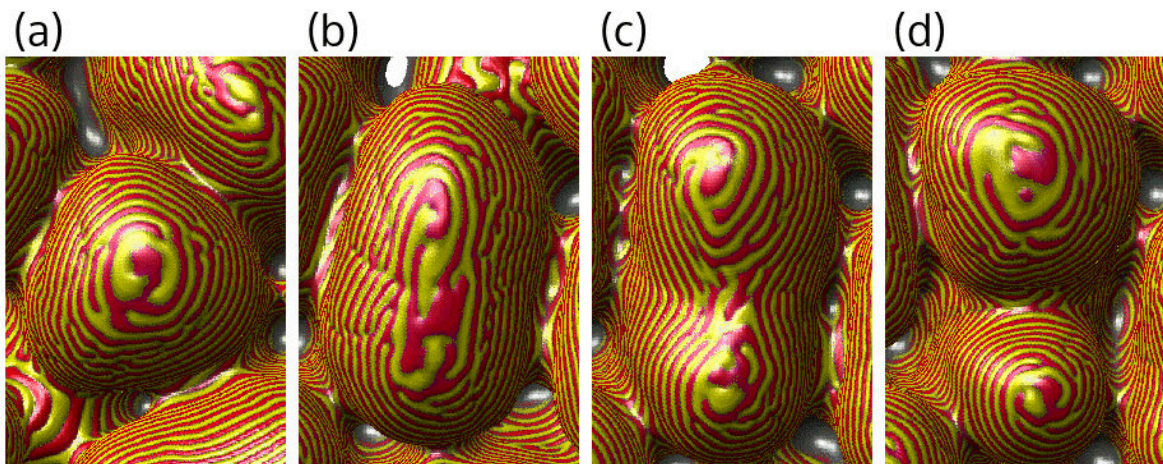


**Figure 5.28.** Tip-splitting process in a large ( $380 \times 380 \times 511$  grid) isotropic simulation. The snapshots show only part of the simulation box focusing on a tip that splits into two. (a) A growing, dendrite-like solid surrounded by bigger ones. (b) As the solid becomes larger, it starts to lose its initial dendritic shape, a second tip appears on the bottom. (c) The newly formed tip becomes larger and the growth in the saddle region between the two tips slows down because of the enrichment of the  $c_3$  component. (d) The two peaks became entirely separated. [Panels (a)–(d) display snapshots taken at  $2.3 \times 10^6$ ,  $2.86 \times 10^6$ ,  $3.14 \times 10^6$ , and  $3.4 \times 10^6$  time steps, respectively.]

most of the available space as it was illustrated in Fig. 5.24. In the example shown in Fig. 5.28 (b), the tip located in the top is currently slowing down, therefore the tip in the center can extend in that direction and forms a vertical ridge-like structure. As the newly formed ridge grows, the center of the original tip shifts upwards, while a second peak appears at the bottom, and therefore a saddle region formed between the two peaks [panel (c)]. The enrichment of the third component slows down the growth at saddle region, therefore it becomes deeper and deeper until the two tips separate entirely [panel (d)].

As a consequence of the continuously changing landscape of the solidification front (tips disappear and split into two), steady-state spiraling morphologies cannot be formed, since a stable dendrite-like shape would be required for steady-state eutectic patterns. On occasion, local spiraling eutectic patterns can be spotted at the top region of the eutectic fingers, however these patterns are only temporary, and they disappear as the underlying finger changes. The perpendicular cross section [see Fig. 5.29]

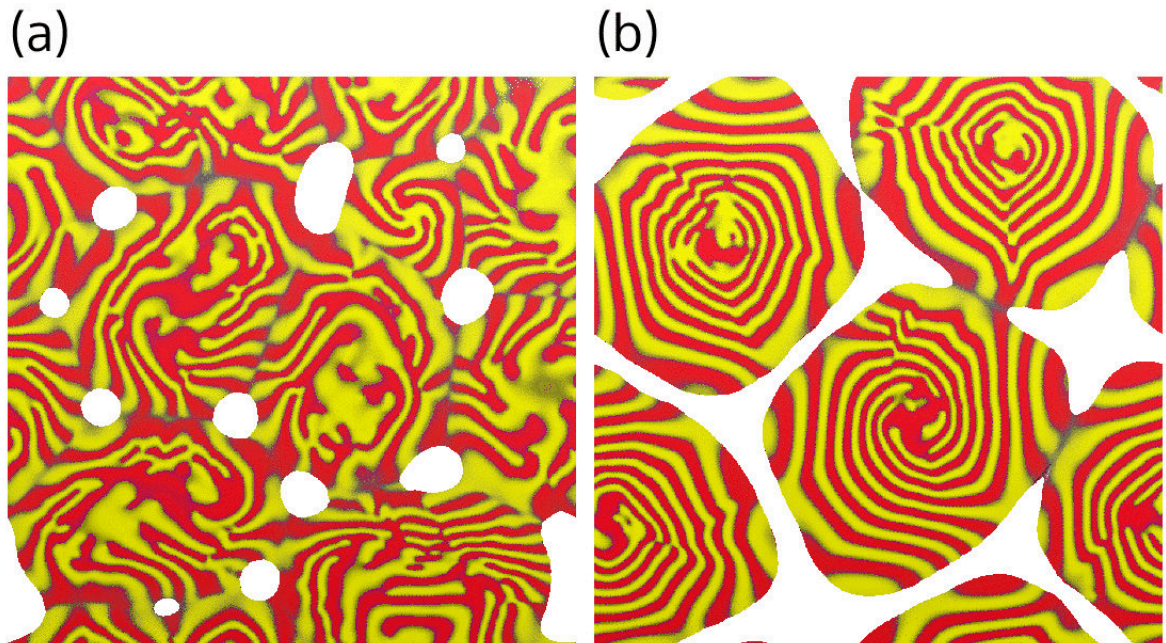


**Figure 5.29.** Cross sections of the large simulations in the  $x - y$  plane, perpendicular to the temperature gradient at  $z = 50$ , taken from the  $2.85 \times 10^6$ th time step. (a) Isotropic case, steady-state spiraling eutectic pattern cannot be spotted in the cross section. The fivefold spiral pattern located near the top right corner belongs to the disappearing tip presented in Fig. 5.27. (b) Anisotropic case, spiraling pattern can be found, e.g. the dendrite located in the center is a fivefold spiral, the top right is a single, the bottom left is a double.

also shows that compared to the large spiraling dendrites from the anisotropic system, the inner structure of these eutectic fingers is rather disordered.

Adding anisotropy to the system changes the landscape of the solidification front. The formation of steady-state eutectic dendrites is shown in Fig. 5.30. After a short transient period, while the individual grains compete with each other [panel (b)], four

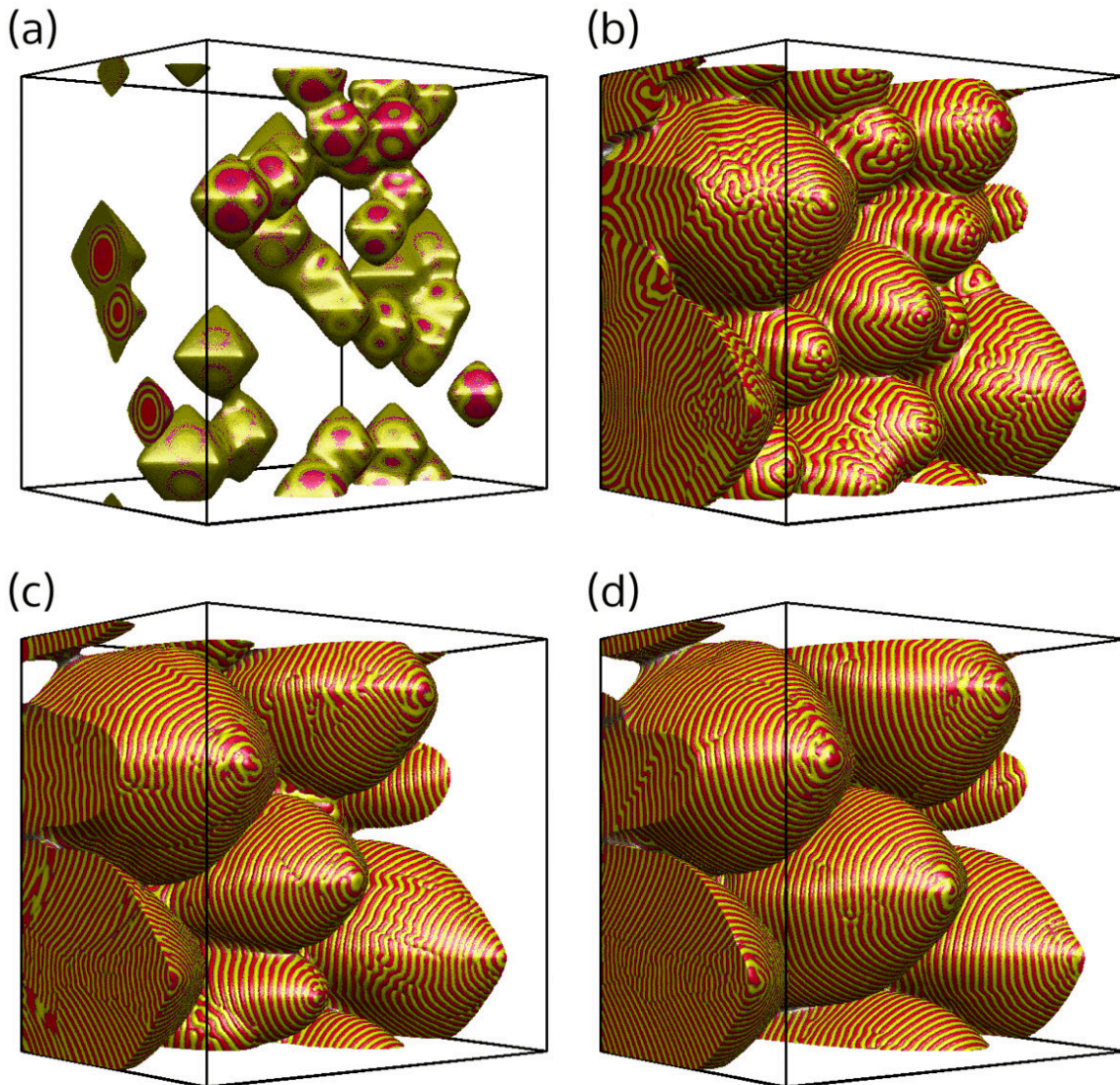


**Figure 5.30.** Formation of two-phase eutectic dendrites in a large anisotropic simulation ( $380 \times 380 \times 511$  grid) performed at  $v_{\text{pull}} = 0.2$ . (a) Starting from 25 homogeneous seeds the initial shape of the grains is similar to a octahedron. (b) A few dendrites start to become bigger, the smaller ones decay. (c) The four remaining dendrites are clearly visible at this point (d) Steady-state growth of the remaining dendrites. Snapshots were taken at  $3 \times 10^5$ ,  $5 \times 10^5$ ,  $10^6$ , and  $2.0 \times 10^6$  time steps.

■ Video 5.30: <https://rlphd.phasefield.hu/aniso>



remaining larger dendrites emerge [panel (c)]. Shortly after, these four dendrites reach their final shape and size [panel (d)], and each smaller dendrite has been eliminated. These dendrites are stable structures, neither of them will undergo tip splitting or elimination process at the later stages of the simulation. While the dendrites reach their final shape, ordered patterns appear on the surface, however more defects can be seen than usually in a smaller simulation, where only a single dendrite is present.

To summarize this section, according to our simulations, anisotropy is required for steady-state spiraling dendrites. Without anisotropy, the solidification front does not have a stable structure; the tips tend to undergo tip-splitting and tip-elimination phenomena. As a consequence, the landscape of the solidification front is continuously changing, which prevents the appearance of steady-state spiraling patterns.

## 5.6 Off-eutectic compositions

As it was stated in Section 4.4, our ternary phase diagram is symmetric in the  $c_1 - c_2$  components, and by choosing  $c_1 = c_2$  as reference composition, the volume fraction of the solid phases (or the phase ratio) has to be  $\eta = 0.5$ . In general, it is beneficial for the spiraling growth modes to keep the volume fraction near 0.5. As we have seen during the exploration of the spiraling domain on the concentration-triangle (Fig. 5.2) in Section 5.2, when the component ratio is too unequal, spiraling growth is not possible [see Fig. 5.3 (a)], since the dendrite has been formed almost exclusively by the majority phase, the minority phase appeared only at bottom region, in the form of thin channels.

However, as in the experiments [16], spiraling dendrites can form with non-equal volume fractions, which can be achieved in our model by setting the liquid composition to an off-eutectic value. In this section, I present two different approaches: in the first one, the composition of the liquid entering the simulation box has been changed gradually (using equal jumps) during the simulation starting from the eutectic value. In the second approach, the composition has been set directly to the required off-eutectic values.

The volume fraction of the  $\alpha$  phase at time  $t$  has been calculated using a  $\phi$ -weighted

approximation:

$$\eta_\alpha(t) = \frac{\sum_{\vec{r}} \phi(\vec{r}, t) c_1(\vec{r}, t)}{\sum_{\vec{r}} \phi(\vec{r}, t) [c_1(\vec{r}, t) + c_2(\vec{r}, t)]}. \quad (5.4)$$

### 5.6.1 Gradually changing composition

In this approach, the starting configuration was a steady-state single spiral dendrite made with the reference eutectic composition ( $c_1 = c_2 = 0.455$ ,  $c_3 = 0.09$ ) and using a lower solid-liquid interface energy:  $\gamma_{\text{SL},0} = 0.022$ , which is in the region, where no spirals with many arms are expected (see Fig. 5.17). This helps the dendrite to remain a single spiral during the growth. After the start of the simulation, the  $c_2$  concentration has been increased by 0.005 on the cost of the  $c_1$  concentration at each  $4 \times 10^5$ th time step, while the  $c_3$  concentration kept constant at the initial  $c_3 = 0.09$  value. The  $4 \times 10^5$  time steps between the composition jumps ensured that the dendrite had enough time to respond to the change, i.e. it reaches a new steady-state structure. An off-eutectic spiraling dendrite can be seen in Fig. 5.31, in which the composition is  $c_1 = 0.35$ ,  $c_2 = 0.56$  and  $c_3 = 0.09$ .

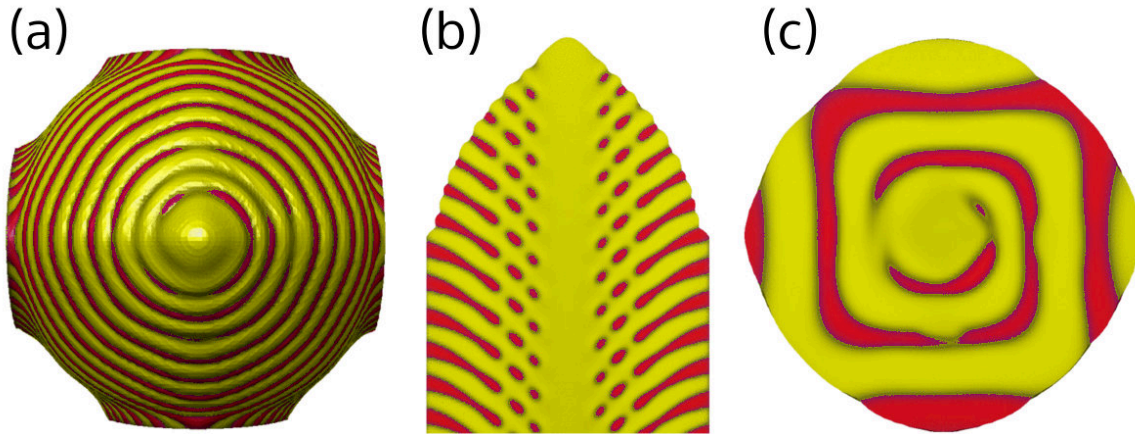


**Figure 5.31.** Off-eutectic spiraling dendrite via changing the composition gradually from the reference point to  $c_1 = 0.35$ ,  $c_2 = 0.56$  and  $c_3 = 0.09$  by 0.005 steps. (a) Top view, the majority phase formed a single phase channel in the center of the dendrite. (b) Parallel cross section at the center of the dendrite. (c) Perpendicular cross section at  $z = 70$ .

■ Video 5.31: <https://rlphd.phasefield.hu/offeut>

The majority phase ( $c_2$  component rich  $\beta$ ) formed a homogeneous channel in the middle of the dendrite [Fig. 5.31 (b)], while the spiraling growth remained at the outer region. The eutectic wavelength is:  $\lambda = 8.4 \pm 0.6$ , which is a bit above the reference

$\lambda^{\text{ref}} = 7.7 \pm 0.5$  value, but taking into account the uncertainty of the determination of wavelength, it is not a significant difference. The widths of the individual lamellae of phases are  $\lambda_{\beta} = 5.2 \pm 0.5$  for the majority phase and  $\lambda_{\alpha} = 3.1 \pm 0.4$  for the lamella of minority phase. The volume fraction is  $\eta_{\alpha} \approx 0.375$ .

On the perpendicular cross section [Fig. 5.31 (c)] a spiraling eutectic pattern can be observed, which is very similar to the cross section of a previously presented single spiral made with the reference composition (second row in Fig. 5.16). However, a closer inspection of the channel region revealed that there are actually two distinct helical structures inside the dendrite: a small inner one around the homogeneous channel and a bigger outer one, which forms the spiraling pattern. This inner helical structure can be seen in Fig. 5.32 (b), where only the minority phase has been shown. The inner structure of the minority phase, which looks like a wire loosely scrolled around a cylinder, and the outer region do not have connection with each other. This can also be seen on the parallel cross section [Fig. 5.31 (b)], where the innermost red disks belong to the inner helical structure, while the rest of the red regions forms the cross section of the outer spiraling structure. The outer part is similar to the eutectic composition case (Fig. 5.16), aside from that the majority phase occasionally penetrates it near the center of the dendrite. In Fig. 5.32 (a), only the majority phase has been plot; the

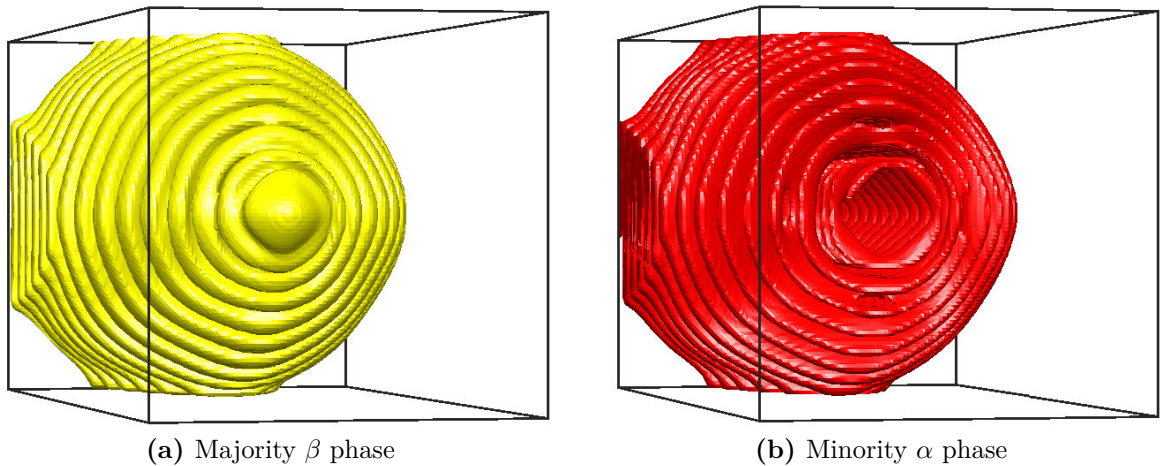


**Figure 5.32.** Off-eutectic dendrite one-phase plots. (a) The majority  $\beta$  phase forms the homogeneous channel in the middle of the dendrite and the spiraling outer region. (b) The minority  $\alpha$  phase creates two distinct helical structure: an inner one around the homogeneous channel formed by the majority phase and a spiraling structure at the outer region.

homogeneous central channel and the outer spiraling region are connected with each other.

The formation of the central homogeneous channel can be seen in Fig. 5.33, where snapshots of parallel cross sections taken in the middle of the dendrite are shown. Only the majority  $\beta$  phase (yellow regions) has been plot, and for the shake of better visibility the cut surfaces are colored with blue. First [panel (a)], the central zone is

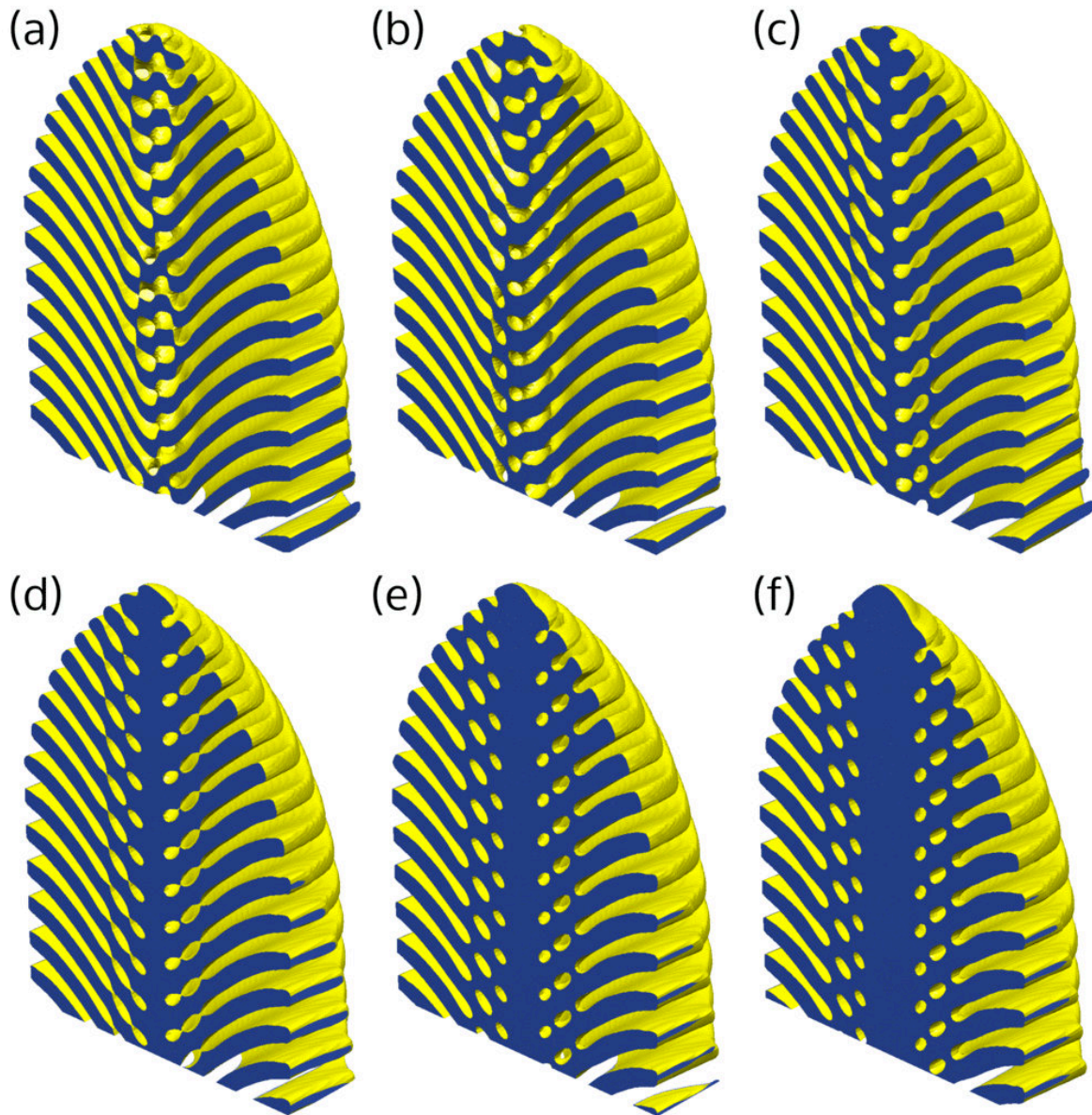


**Figure 5.33.** Parallel ( $y-z$ ) cross sections in the middle of the dendrite showing the formation of the homogeneous channel of the majority phase. Only the  $\beta$  majority phase has been shown (with yellow) and the cut surfaces colored with blue for the better visibility. The concentrations are: (a)  $c_1 = 0.425, c_2 = 0.485$  (b)  $c_1 = 0.400, c_2 = 0.510$  (c)  $c_1 = 0.390, c_2 = 0.520$  (d)  $c_1 = 0.375, c_2 = 0.535$  (e)  $c_1 = 0.365, c_2 = 0.545$  (f)  $c_1 = 0.350, c_2 = 0.560$

similar to a single spiral (Fig. 5.16) formed with the reference composition, then as the  $c_2$  concentration increases, a cork-screw like structure of the majority phase appears in the middle [panel (b)]. Next, a homogeneous, central, thin cylinder forms [panel (c)], that becomes wider and wider as the  $c_2$  concentration increases [panels (d)-(f)].

Likewise the previous figure, Fig. 5.34 shows the parallel cross sections of the minor-

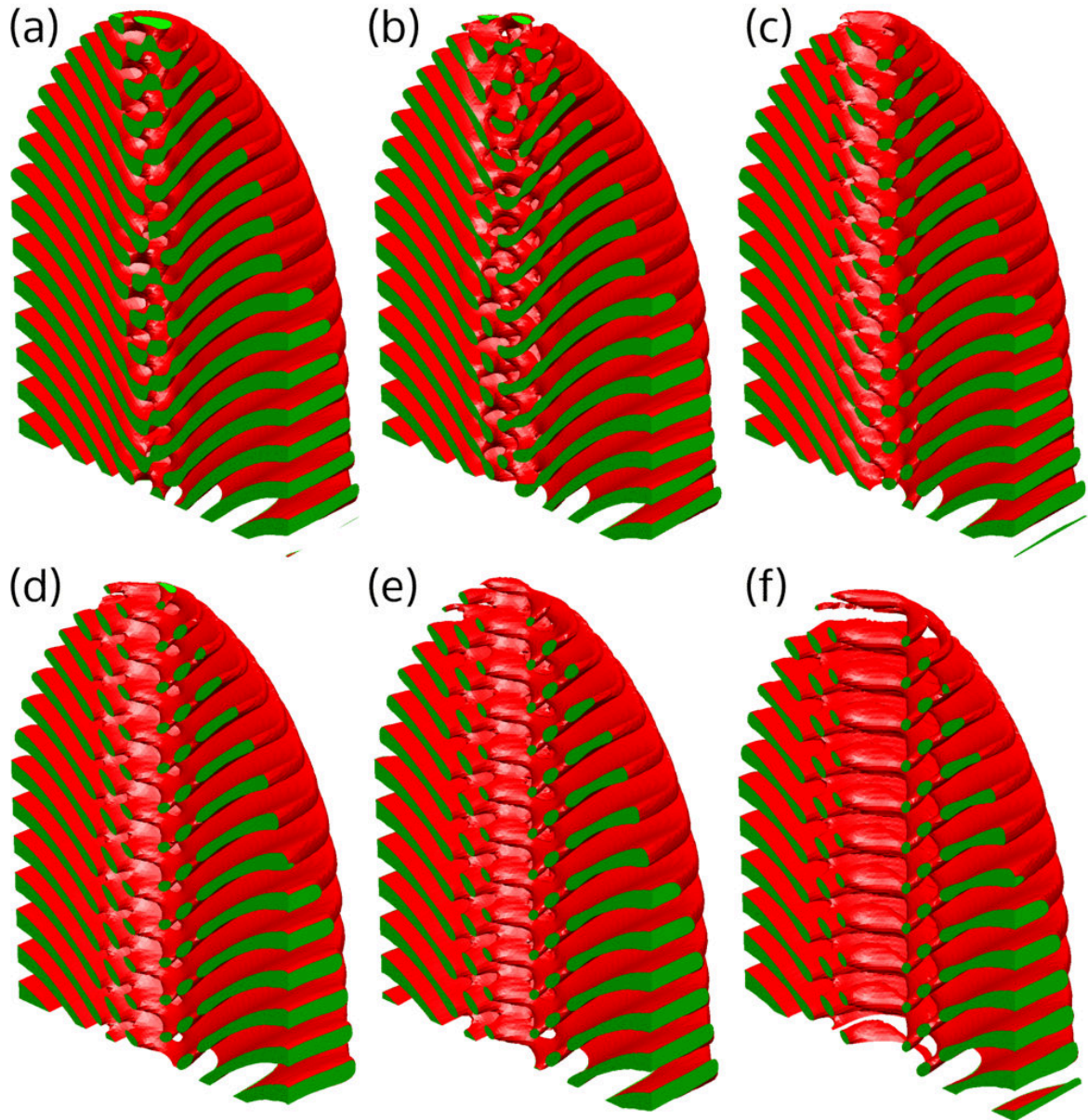


**Figure 5.34.** Parallel ( $y-z$ ) cross sections in the middle of the dendrite showing the formation of the inner and outer helical structures of the minority phase. Only the  $\alpha$  minority phase has been shown (with red) and the cut surfaces colored with green for better visibility. The concentrations are: (a)  $c_1 = 0.425$ ,  $c_2 = 0.485$  (b)  $c_1 = 0.400$ ,  $c_2 = 0.510$  (c)  $c_1 = 0.390$ ,  $c_2 = 0.520$  (d)  $c_1 = 0.375$ ,  $c_2 = 0.535$  (e)  $c_1 = 0.365$ ,  $c_2 = 0.545$  (f)  $c_1 = 0.350$ ,  $c_2 = 0.560$

ity  $\alpha$  phase at the same time steps ( $c_1/c_2$  ratios). An empty cylindrical space appears in the central region in panels (b) and (c), which indicates the formation of the homogeneous central channel of the majority phase. Then, the channel becomes wider, therefore the minority phase draws back towards the outer part of the dendrite [panels (d)-(f)].

## 5.6.2 Directly set composition

In this approach, the composition was set directly to the required off-eutectic values, and the simulations were started from a homogeneous seed with included chemical noise. The solid-liquid interface energy was set to the reference value ( $\gamma_{SL,0} = 0.059$ ), which permits dendrites with more spiral arm as well.

In the first example, the composition is set to  $c_1 = 0.395$ ,  $c_2 = 0.515$  and  $c_3 = 0.09$  and after a long transient period, a threefold spiral dendrite has formed. As seen in Fig. 5.35 (a), this off-eutectic spiraling pattern is very similar to the threefold pattern seen previously with the reference composition [Fig. 5.11 (d)], as well as the parallel and vertical cross sections [panels (b) and (c) of Fig. 5.35 compared to Fig. 5.16 third row]. The measured eutectic wavelength is  $\lambda = 7.7 \pm 0.5$ , which is close to the reference value:

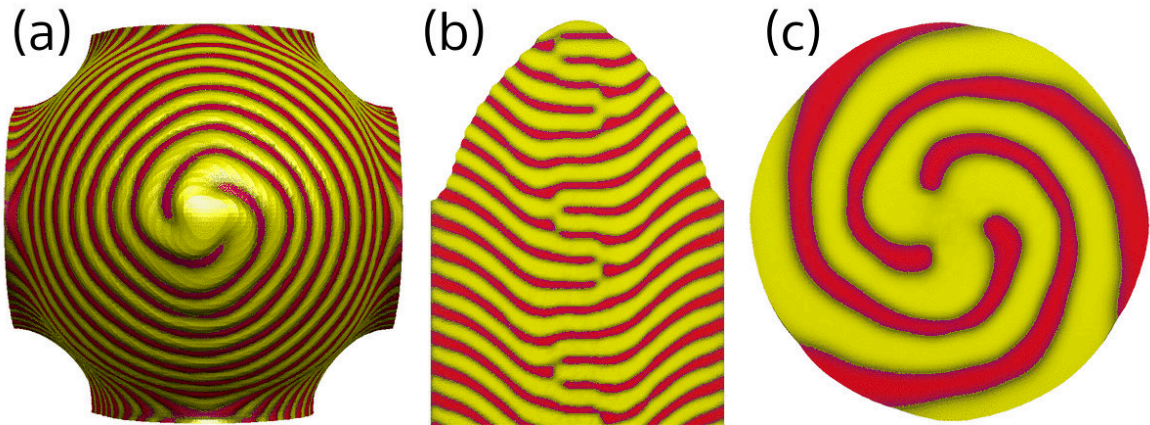


**Figure 5.35.** Off-eutectic threefold spiral dendrite via directly setting the composition to  $c_1 = 0.395$ ,  $c_2 = 0.515$  and  $c_3 = 0.09$ , the volume fraction is:  $\eta_\alpha = 0.421$ . (a) Top view, the lamellae of majority phase are thicker than the lamellae of minority phase. (b) Parallel cross section at the center of the dendrite. Similar to the cross section of a threefold dendrite of reference composition: alternating  $\alpha$  and  $\beta$  phases in the center. (c) Perpendicular cross section at  $z = 70$ . The snapshots are taken from the  $8 \times 10^6$ th time step.

■ Video 5.35: <https://rlphd.phasefield.hu/offeut2>

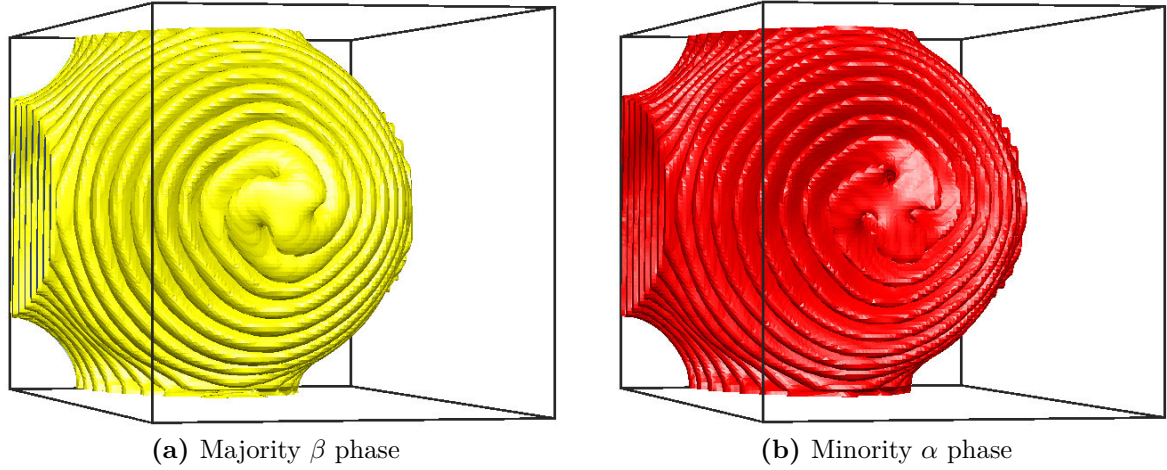


**Figure 5.36.** One-phase plots of off-eutectic threefold spiral dendrite via directly setting the composition to  $c_1 = 0.395$ ,  $c_2 = 0.515$  and  $c_3 = 0.09$ , the volume fraction is:  $\eta_\alpha = 0.421$ . (a) The majority  $\beta$  phase. (b) The minority  $\alpha$  phase.

$\lambda^{\text{ref}} = 7.6 \pm 0.5$ . The widths of the individual lamellae of phases are  $\lambda_\beta = 4.7 \pm 0.5$  for the majority phase and  $\lambda_\alpha = 3.6 \pm 0.4$  for the lamella of minority phase. The volume fraction is  $\eta_\alpha \approx 0.421$ . The one-phase plots can be seen in Fig. 5.36. The different widths of the lamellae is apparent, the majority phase [panel (a)] formed thicker lamellae than the minority phase [panel (b)]. However, their internal structure are similar, the majority phase has not yet created a homogeneous channel in the middle of the dendrite.

Increasing further the  $c_1/c_2$  ratio in a new simulation (Fig. 5.37) by setting the

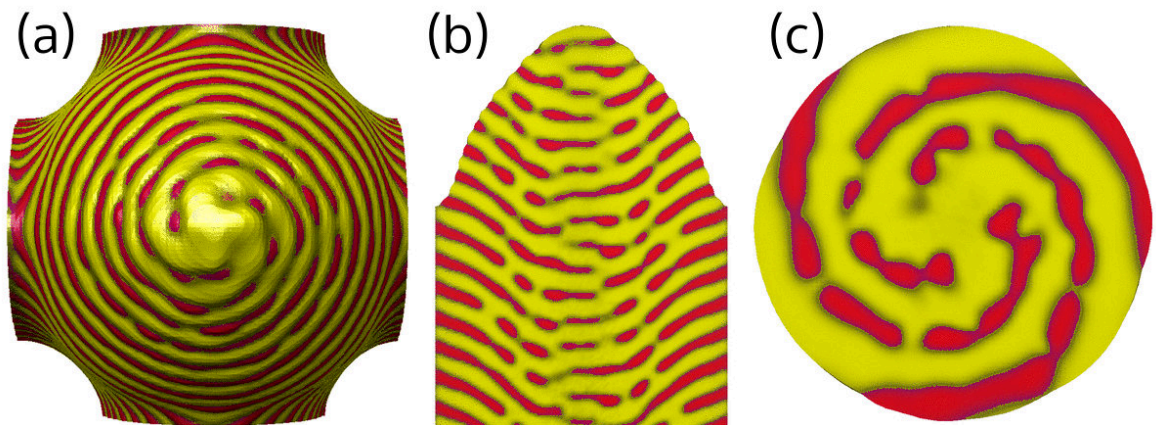


**Figure 5.37.** Off-eutectic threefold spiral dendrite via directly setting the composition to  $c_1 = 0.385$ ,  $c_2 = 0.525$  and  $c_3 = 0.09$ , the volume fraction is:  $\eta_\alpha = 0.407$ . (a) Top view. (b) Parallel cross section at the center of the dendrite. (c) Perpendicular cross section at  $z = 80$ .

Video 5.37: <https://rlphd.phasefield.hu/offeut3>

liquid composition to  $c_1 = 0.385$ ,  $c_2 = 0.525$  and  $c_3 = 0.09$  results in a volume fraction of  $\eta_\alpha = 0.407$ , and changes the solidification morphology. In contrast to the previous case, the minority phase formed many disjointed sections on the surface of the dendrite [Fig. 5.37 (a)], instead of thin lamellae whose width corresponds roughly the volume fraction. However, the spiraling pattern is still recognizable on the surface and at the perpendicular cross section [panel (c)].

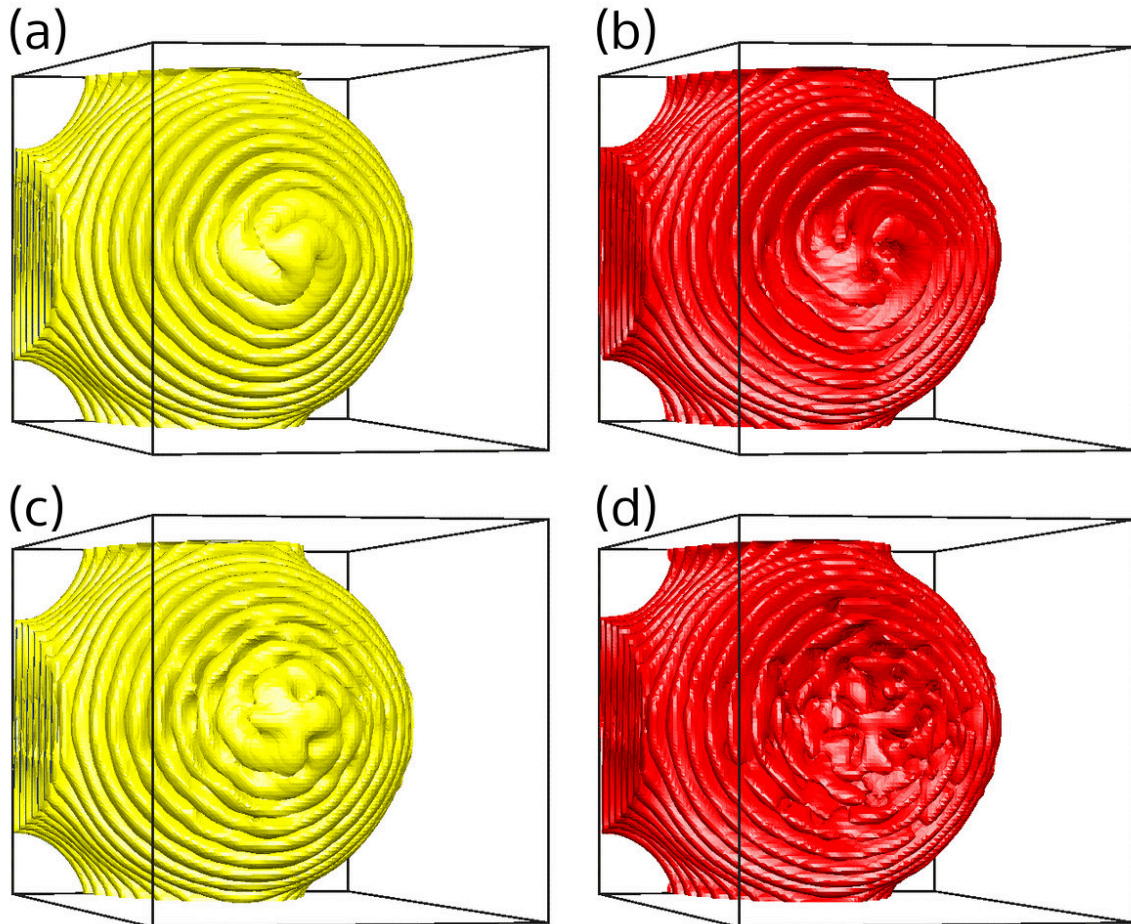


**Figure 5.38.** One-phase plots of off-eutectic threefold spiral dendrite via directly setting the composition to  $c_1 = 0.385$ ,  $c_2 = 0.525$  and  $c_3 = 0.09$ , the volume fraction is:  $\eta_\alpha = 0.407$ . (a)-(b): the structure before the transition at the  $4 \times 10^6$ th time step, majority and minority phases. (c)-(d): the structure after the transition at the  $8 \times 10^6$ th time step, majority and minority phases.

Remarkably, the transition from regular lamellae growth, like in the previous case (Fig. 5.35), to this irregular lamellae growth happens within a single simulation at this component ratio. After a long transient period, first, a threefold dendrite is forming with regular lamellae, then starting from the tip, this regular structure slowly turns into the irregular lamellae. In Fig. 5.38 the one phase plots are shown before the



transition (first row) and after the transition (second row), while the parallel cross section plots can be seen in Fig. 5.39. The structure formed by the minority phase looks like disjointed sections on the surface of the dendrite [Fig. 5.37 (a)], but they are connected internally [see Fig. 5.38 (d) and Fig. 5.39 (b)]. They form a lamellar spiraling structure with many holes and irregularities, that the majority phase fills out.

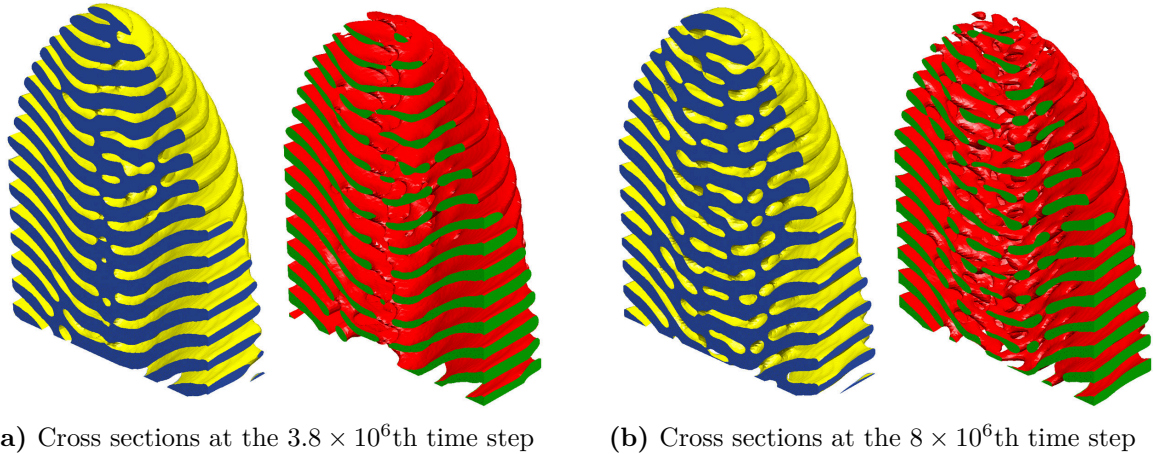


**Figure 5.39.** Parallel ( $y-z$ ) one-phase cross sections in the middle of the dendrite showing the transition from regular- to irregular lamellae growth ( $c_1 = 0.385$ ,  $c_2 = 0.525$  and  $c_3 = 0.09$ , the volume fraction is:  $\eta_\alpha = 0.407$ ).

Before the transition, the eutectic wavelength is  $\lambda = 7.8 \pm 0.5$ , meanwhile the widths of the individual lamellae of phases are  $\lambda_\beta = 4.9 \pm 0.5$  for the majority  $\beta$  phase and  $\lambda_\alpha = 2.9 \pm 0.4$  for the minority  $\alpha$  phase. After the transition, measuring the wavelength of the lamellae is getting harder, but it can be done by finding a few characteristic sections on the surface where both phases are present with their typical width and making the measurement there. The widths of the lamellae after the transition are  $\lambda_\beta = 4.4 \pm 0.5$  for the majority phase and  $\lambda_\alpha = 3.6 \pm 0.4$  for the minority phase. The volume fraction does not change, it is still  $\eta_\alpha = 0.407$  for both cases. So it seems that, when the volume fraction would result in a spiraling lamellar structure, where the lamellae widths of the two phases are too unequal, it becomes unstable and forms this complex structure, where the lamellae widths are closer to each other.

This transition is similar to the intermediate states of rods-lamellae-rods transition in a binary eutectic system [76], where the volume fraction of the phases was changed linearly from 0.8 to 0.2 via changing the concentration in a 3D phase-field simulation. The transition from rods to lamellae happens around 0.3 volume fraction, when some

thin lamellae disjoin and first they form wider, rounded rectangle shaped columns, then these columns become the rounded rods at 0.2 volume fraction. In the ternary spiraling system, individual rods cannot be seen, since the growth is much more complicated and the whole eutectic pattern is rotating. However the trends are similar; increasing the volume fraction makes the structure formed by the majority phase more coherent [see Fig. 5.39 (b)], while the minority phase forms more disjoint regions instead of very thin lamellae. This process can be understood as a way of minimizing the interface and therefore the interface free energy between the  $\alpha - \beta$  phases.

To summarize this section, my goal was not to make quantitative statements, but to show some interesting features of the off-eutectic spiraling dendrites. Considering the complexity of the problem and the large number of parameters, further research is required to explore the whole ternary parameter space and study the wide range of structures, that a ternary system can produce. I hope this work will also inspire further research on exotic ternary systems.

# Chapter 6

## Summary

In my doctoral work I have investigated the formation of ternary eutectic dendrites within the Phase-Field Theory. The work was inspired by the experimental results of Akamatsu *et al.* on spiral two-phase dendrites: During the growth of a two-phase solid from a ternary melt, two components of the alloy combine to form the eutectic microstructure. Meanwhile, the third one is rejected into the liquid, which generates the Mullins-Sekerka instability, i.e. destabilizing the eutectic growth front and creating the dendritic shape of the solid. The spiraling pattern is caused by the growth of two different crystal phases from the apex of a parabolic finger, which leaves behind a double helix microstructure in the solid.

In order to model this ternary eutectic alloy with two solid phases, the binary phase-field model was extended to ternary systems. Ideal solution model was used for the liquid, and regular solution model for the solid phases. The parameters were chosen so, that the ternary phase diagram was symmetric in the  $c_1 - c_2$  components. For solving the equations of motion numerically, 3D parallel simulation programs were developed, that can utilize hundreds of CPU cores or graphical cards to allow for sufficiently large simulation boxes. The programs used the finite difference method with the forward Euler time-stepping scheme to solve the equations on uniformly spaced grids. The directional solidification setup used in the experiments was modeled by a temperature gradient that was moved with the pulling speed. In order to save a lot of computational power and reduce the memory requirement, the simulation box followed the solidification front, which greatly decreased the necessary size of the simulation box.

The thermal fluctuations were modeled with added concentration noise or by starting the simulations with a random initial configuration of the two solid phases.

I have explored the parameter space to find the optimized conditions for growing spiraling structures and also to investigate the properties of the two-phase dendrites. First, I have identified the region of the concentration-triangle, in which dendrites with ordered pattern (spiral or target) appear. It is roughly an oval region around the reference composition. Outside that region, when the  $c_1/c_2$  component ratio was too high ( $> 0.6$ ) the majority phase formed an almost homogeneous dendrite, the minority phase appeared occasionally only at the surface far from the tip. In the  $c_3$  component rich case ( $c_3 > 0.17$ ), the formation of individual  $\alpha$  and  $\beta$  solid phases was prevented by the limited diffusion of the components. A homogeneous dendrite is formed by a metastable solid phase, in which  $c_1 \approx c_2$ , therefore spiraling pattern cannot be seen. In the opposite case, when the  $c_3$  concentration is low ( $c_3 < 0.05$ ), the solidification front becomes almost flat with fast growing  $\alpha$  and  $\beta$  phases, since not enough  $c_3$  component is rejected by the front to generate a dendritic structure.

Increasing the pulling velocity, the solidification front shows the following sequence of transitions between morphologies/patterns: flat front lamellae  $\rightarrow$  eutectic colonies  $\rightarrow$  eutectic dendrites  $\rightarrow$  dendrites with ordered pattern  $\rightarrow$  partitionless dendrites  $\rightarrow$  flat partitionless solid (due to full solute trapping). During the transition from a flat surface with lamellae perpendicular to it (seen at small velocities) to a flat surface at full solute trapping (at high velocities), the direction of lamellae is altering gradually from the usual parallel to the temperature gradient seen at low velocities to perpendicular. I have shown that the eutectic wavelength of the two-phase dendrites scales according to the Jackson–Hunt scaling rule when the pulling speed is changed. The geometrical shape of the two-phase dendrites and the tip radius behave analogously to their single-phase counterparts, when the solid-liquid interface energy is changed. Apparently, the underlying eutectic pattern has no significant influence on the shape of the dendrite.

Beside the single spiraling dendrites seen in the experiments, I have found additional patterns including the target pattern and multiarm spirals. The target pattern appears via alternating nucleation of the two solid phases on top of each other, which means, that this mode could appear only at larger undercoolings. However, no nucleation is required for the formation of single- and double spirals, therefore these mechanisms can

prevail at small undercoolings. In the case of a single spiral, both solid phases can grow simultaneously via rotating around each other. The double spiral grows so that the two solid phases occupy the tip region alternately. The growth modes with more than two spiral arms become increasingly more complex, still displaying alternating phase appearance at the tip. The spiral arms of a phase usually connect to a homogeneous disk, which nucleated on top of the other solid phase at the tip. The rotation direction of the spirals is random.

I have shown that at a given parameter set, steady-state dendrites with different number of spiral arms (including the target pattern) can form, of which the fluctuations choose during the solidification. This stochastic behavior is characterized by peaked probability distributions. The number of spiral arms tends to increase with increasing tip radius, that I achieved by increasing the solid-liquid interface energy, or decreasing the kinetic anisotropy.

Using large-scale simulations I have shown that anisotropy is required for appearance of steady-state spiraling dendrites. Without anisotropy, the solidification front does not have a stable structure; the tips tend to undergo tip-splitting as they grow larger. Furthermore, smaller tips sometimes slow down and disappear as a result of the competition between them. The consequence of these phenomena is that the landscape of the solidification front is continuously changing, which prevents the appearance of steady-state spiraling patterns.

I have shown two approaches to produce spiraling dendrites with unequal volume fraction. Since our simple model ternary phase diagram was symmetric in the  $c_1 - c_2$  components, in order to have unequal phase ratio of the two solid phases, the liquid composition was set to an off-eutectic value, where the concentration of  $c_1$  and  $c_2$  components was not equal. In the first approach, I started with a steady-state single spiraling dendrite, which was produced using the reference symmetric composition, then during the simulation the  $c_1/c_2$  ratio of the liquid phase entering the simulation box was changed gradually using small equal jumps. The timing of the composition jumps ensured that the dendrite had enough time to respond to the new environment i.e. reaching its new steady-state structure. With this method the dendrite developed a homogeneous channel of the majority phase in the middle, while the spiraling structure remained at the outer region. The eutectic wavelength did not changed significantly,

but the lamellae of the minority phase became thinner, which was compensated by the thicker lamellae of the majority phase.

In the second method, the composition was set to the off-eutectic value right at the beginning, and the simulation was started with a small spherical seed of either of the two solid phases. After a long transient period, steady-state spiraling dendrites formed as well. The ratio of the lamellae width of the two phases followed the volume fraction until a specific value, where the regular spiraling lamellar growth became unstable. After that the structure slowly transformed into a complex shape, where the lamellae of the minority phase became thicker, but also had many holes and irregularities, that the majority phase filled out. However, the spiraling pattern was still recognizable on the surface of the dendrite, and in the cross sections as well. This phenomenon can be viewed as an analogy of the well-known rod to lamellar transition in binary eutectic systems, realized now in a complex helical environment.

# References

- [1] Elizabeth A. Kessler. “Resolving the nebulae: the science and art of representing M51”, *Studies in History and Philosophy of Science Part A*, **38**(2):477–491, 2007.
- [2] Kun Wei, Zhong-liang Jing, Yuan-xiang Li, and Su-liang Liu. “Spiral band model for locating Tropical Cyclone centers”, *Pattern Recognition Letters*, **32**(6):761–770, 2011.
- [3] Jeffrey L. Hutter and John Bechhoefer. “Banded spherulitic growth in a liquid crystal”, *Journal of Crystal Growth*, **217**(3):332–343, 2000.
- [4] Florian Siegert and Cornelis J. Weijer. “Spiral and concentric waves organize multicellular Dictyostelium mounds”, *Current Biology*, **5**(8):937–943, 1995.
- [5] Jens Rietdorf, Florian Siegert, and Cornelis J. Weijer. “Analysis of Optical Density Wave Propagation and Cell Movement during Mound Formation in Dictyostelium discoideum”, *Developmental Biology*, **177**(2):427–438, 1996.
- [6] A.M. Mathai and T. Anthony Davis. “Constructing the sunflower head”, *Mathematical Biosciences*, **20**(1-2):117–133, 1974.
- [7] R. V. Suganthi, E. K. Girija, S. Narayana Kalkura, H. K. Varma, and A. Rajaram. “Self-assembled right handed helical ribbons of the bone mineral hydroxyapatite”, *Journal of Materials Science: Materials in Medicine*, **20**(S1):131–136, 2009.
- [8] Shibi Thomas, István Lagzi, Ferenc Molnár, and Zoltán Rácz. “Helices in the wake of precipitation fronts”, *Physical Review E*, **88**(2):022141, 2013.
- [9] C. Klemenz. “Hollow cores and step-bunching effects on (0 0 1)YBCO surfaces grown by liquid-phase epitaxy”, *Journal of Crystal Growth*, **187**(2):221–227, 1998.
- [10] Marilyn Hawley, Ian D. Raistrick, Jerome G. Beery, and Robert J. Houlton. “Growth Mechanism of Sputtered Films of YBa<sub>2</sub>Cu<sub>3</sub>O<sub>7</sub> Studied by Scanning Tunneling Microscopy”, *Science*, **251**(5001), 1991.
- [11] C. Gerber, D. Anselmetti, J. G. Bednorz, J. Mannhart, and D. G. Schlom. “Screw dislocations in high-Tc films”, *Nature*, **350**(6316):279–280, 1991.
- [12] G. Springholz, A. Y. Ueta, N. Frank, and G. Bauer. “Spiral growth and threading dislocations for molecular beam epitaxy of PbTe on BaF<sub>2</sub> (111) studied by scanning tunneling microscopy”, *Applied Physics Letters*, **69**(19):2822–2824, 1996.

- [13] R.L Fullman and D.L Wood. “Origin of spiral eutectic structures”, *Acta Metallurgica*, **2**(2):188–193, 1954.
- [14] H.Y. Liu and H. Jones. “Solidification microstructure selection and characteristics in the zinc-based Zn-Mg system”, *Acta Metallurgica et Materialia*, **40**(2):229–239, 1992.
- [15] Shibi Thomas, István Lagzi, Ferenc Molnár, and Zoltán Rácz. “Probability of the Emergence of Helical Precipitation Patterns in the Wake of Reaction-Diffusion Fronts”, *Physical Review Letters*, **110**(7):078303, 2013.
- [16] Silvère Akamatsu, Mikaël Perrut, Sabine Bottin-Rousseau, and Gabriel Faivre. “Spiral Two-Phase Dendrites”, *Physical Review Letters*, **104**(5):056101, 2010.
- [17] Bakthier Vasiev, Florian Siegert, and Cornelis Weijer. “Multiarmed Spirals in Excitable Media”, *Physical Review Letters*, **78**(12):2489–2492, 1997.
- [18] C.T Lin. “Study of growth spirals and screw dislocations on YBa<sub>2</sub>Cu<sub>3</sub>O<sub>7-δ</sub> single crystals”, *Physica C: Superconductivity*, **337**(1-4):312–316, 2000.
- [19] György Tegze and Gyula I. Tóth. “Osmotic convection-driven instability and cellular eutectic growth in binary systems”, *Acta Materialia*, **60**(4):1689–1694, 2012.
- [20] Alar Toomre. “Theories of Spiral Structure”, *Annual Review of Astronomy and Astrophysics*, **15**(1):437–478, 1977.
- [21] Vincent Hakim and Alain Karma. “Theory of spiral wave dynamics in weakly excitable media: Asymptotic reduction to a kinematic model and applications”, *Physical Review E*, **60**(5):5073–5105, 1999.
- [22] A. Karma and V. S. Zykov. “Structure of the Resonance Attractor for Spiral Waves in Excitable Media”, *Physical Review Letters*, **83**(12):2453–2456, 1999.
- [23] Aric Hagberg and Ehud Meron. “Complex patterns in reaction-diffusion systems: A tale of two front instabilities”, *Chaos: An Interdisciplinary Journal of Nonlinear Science*, **4**(3):477–484, 1994.
- [24] Alain Karma and Mathis Plapp. “Spiral Surface Growth without Desorption”, *Physical Review Letters*, **81**(20):4444–4447, 1998.
- [25] T. Kyu, H.-W. Chiu, A. J. Guenthner, Y. Okabe, H. Saito, and T. Inoue. “Rhythmic Growth of Target and Spiral Spherulites of Crystalline Polymer Blends”, *Physical Review Letters*, **83**(14):2749–2752, 1999.
- [26] Jean-Marc Debierre, Rahma Guérin, and Klaus Kassner. “Crystal growth in a channel: Pulsating fingers, merry-go-round patterns, and seesaw dynamics”, *Physical Review E*, **88**(4):042407, 2013.
- [27] Arka Lahiri, Chandrashekhara Tiwary, Kamanio Chattopadhyay, and Abhik Choudhury. “Eutectic colony formation in systems with interfacial energy



- anisotropy: A phase field study”, *Computational Materials Science*, **130**:109–120, 2017.
- [28] J B Pendry. “A chiral route to negative refraction.” *Science*, **306**(5700):1353–5, 2004.
- [29] S. A. Souza, C. T. Rios, A. A. Coelho, P. L. Ferrandini, S. Gama, and R. Caram. “Growth and morphological characterization of Al-Cr-Nb eutectic alloys”, *Journal of Alloys and Compounds*, **402**(1-2):156–161, 2005.
- [30] Jonathan Dantzig and Michel Rappaz. “Solidification”, EPFL Press, 2009.
- [31] A.J. Melendez and C. Beckermann. “Measurements of dendrite tip growth and sidebranching in succinonitrile–acetone alloys”, *Journal of Crystal Growth*, **340**(1):175–189, 2012.
- [32] R. E. Napolitano, H. Meco, and C. Jung. “Faceted solidification morphologies in low-growth-rate Al-Si eutectics”, *JOM*, **56**(4):16–21, 2004.
- [33] W. W. Mullins and R. F. Sekerka. “Morphological Stability of a Particle Growing by Diffusion or Heat Flow”, *Journal of Applied Physics*, **34**(2):323–329, 1963.
- [34] L.X. Liu. and J.S. Kirkaldy. “Relationship between free and forced velocity or cellular dendrites”, *Scripta Metallurgica et Materialia*, **29**(6):801–806, 1993.
- [35] L. Sturz, V.T. Witusiewicz, U. Hecht, and S. Rex. “Organic alloy systems suitable for the investigation of regular binary and ternary eutectic growth”, *Journal of Crystal Growth*, **270**(1):273–282, 2004.
- [36] C. Zener. “Kinetics of the decomposition of austenite”, *Trans. Met. Soc. AIME*, **167**:550–955, 1946.
- [37] J.D. Hunt and J.P. Chilton, *J. Inst. Metals*, **92**:21, 1963.
- [38] K.A. Jackson and J.D. Hunt. “Lamellar and rod eutectic growth”, *Trans. Met. Soc. AIME*, **236**:1129–1142, 1966.
- [39] W. J. Boettinger, J. A. Warren, C. Beckermann, and A. Karma. “Phase-Field Simulation of Solidification”, *Annual Review of Materials Research*, **32**(1):163–194, 2002.
- [40] A Malik, G Amberg, A Borgenstam, and J Ågren. “Phase-field modelling of martensitic transformation: the effects of grain and twin boundaries”, *Modelling and Simulation in Materials Science and Engineering*, **21**(8):085003, 2013.
- [41] Shinji Nambu and Djuniadi A. Sagala. “Domain formation and elastic long-range interaction in ferroelectric perovskites”, *Physical Review B*, **50**(9):5838–5847, 1994.
- [42] I. Steinbach, F. Pezzolla, B. Nestler, M. Seeßelberg, R. Prieler, G.J. Schmitz, and J.L.L. Rezende. “A phase field concept for multiphase systems”, *Physica D: Nonlinear Phenomena*, **94**(3):135–147, 1996.

- [43] Celeste Sagui, Daniel Orlikowski, Andrés M. Somoza, and Christopher Roland. “Three-dimensional simulations of Ostwald ripening with elastic effects”, *Physical Review E*, **58**(4):R4092–R4095, 1998.
- [44] D. Rodney, Y. Le Bouar, and A. Finel. “Phase field methods and dislocations”, *Acta Materialia*, **51**(1):17–30, 2003.
- [45] Y. M. Jin, Y. U. Wang, and A. G. Khachaturyan. “Three-dimensional phase field microelasticity theory and modeling of multiple cracks and voids”, *Applied Physics Letters*, **79**(19):3071–3073, 2001.
- [46] Deepali N. Bhate, Ashish Kumar, and Allan F. Bower. “Diffuse interface model for electromigration and stress voiding”, *Journal of Applied Physics*, **87**(4):1712–1721, 2000.
- [47] X.N. Jing, J.H. Zhao, G. Subhash, and X.-L. Gao. “Anisotropic grain growth with pore drag under applied loads”, *Materials Science and Engineering: A*, **412**(1):271–278, 2005.
- [48] Qiang Du, Chun Liu, and Xiaoqiang Wang. “Simulating the deformation of vesicle membranes under elastic bending energy in three dimensions”, *Journal of Computational Physics*, **212**(2):757–777, 2006.
- [49] V. L. Ginzburg and L. D. Landau. “On the theory of superconductivity”, *J. Exptl. Theoret. Phys.*, **20**:1064, 1950.
- [50] John W. Cahn and John E. Hilliard. “Free Energy of a Nonuniform System. I. Interfacial Free Energy”, *The Journal of Chemical Physics*, **28**(2):258–267, 1958.
- [51] J. Langer. “Models of pattern formation in first-order phase transitions”, in G. Grinstein and G. Mazenko, editors, *Directions in Condensed Matter Physics*, pages 165–185, World scientific, Singapore, 1986.
- [52] Joseph B. Collins and Herbert Levine. “Diffuse interface model of diffusion-limited crystal growth”, *Physical Review B*, **31**(9):6119–6122, 1985.
- [53] Gunduz Caginalp and Paul Fife. “Phase-field methods for interfacial boundaries”, *Physical Review B*, **33**(11):7792–7794, 1986.
- [54] Seong Gyoon Kim, Won Tae Kim, and Toshio Suzuki. “Phase-field model for binary alloys”, *Physical Review E*, **60**(6):7186–7197, 1999.
- [55] A. A. Wheeler, W. J. Boettinger, and G. B. McFadden. “Phase-field model for isothermal phase transitions in binary alloys”, *Physical Review A*, **45**(10):7424–7439, 1992.
- [56] Samuel M. Allen and John W. Cahn. “A microscopic theory for antiphase boundary motion and its application to antiphase domain coarsening”, *Acta Metallurgica*, **27**(6):1085–1095, 1979.
- [57] P. C. Hohenberg and B. I. Halperin. “Theory of dynamic critical phenomena”, *Reviews of Modern Physics*, **49**(3):435–479, 1977.

- [58] J.A. Warren and W.J. Boettinger. “Prediction of dendritic growth and microsegregation patterns in a binary alloy using the phase-field method”, *Acta Metallurgica et Materialia*, **43**(2):689–703, 1995.
- [59] László Gránásy, Tamás Börzsönyi, and Tamás Pusztai. “Nucleation and Bulk Crystallization in Binary Phase Field Theory”, *Physical Review Letters*, **88**(20):206105, 2002.
- [60] Nele Moelans, Bart Blanpain, and Patrick Wollants. “An introduction to phase-field modeling of microstructure evolution”, *Calphad*, **32**(2):268–294, 2008.
- [61] Edgar Gabriel, Graham E. Fagg, George Bosilca, Thara Angskun, Jack J. Dongarra, Jeffrey M. Squyres, Vishal Sahay, Prabhanjan Kambadur, Brian Barrett, Andrew Lumsdaine, Ralph H. Castain, David J. Daniel, Richard L. Graham, and Timothy S. Woodall. “Open MPI: Goals, Concept, and Design of a Next Generation MPI Implementation”, in pages 97–104, Springer, Berlin, Heidelberg, 2004.
- [62] John L. Gustafson and John L. “Reevaluating Amdahl’s law”, *Communications of the ACM*, **31**(5):532–533, 1988.
- [63] Andreas Klöckner, Nicolas Pinto, Yunsup Lee, Bryan Catanzaro, Paul Ivanov, and Ahmed Fasih. “PyCUDA and PyOpenCL: A scripting-based approach to GPU run-time code generation”, *Parallel Computing*, **38**(3):157–174, 2012.
- [64] William H. Press, Saul A. Teukolsky, William T. Vetterling, and Brian P. Flannery. “Numerical recipes in C : the art of scientific computing”, Cambridge University Press, 1992, page 994.
- [65] Efim Brener and Dmitri Temkin. “Noise-induced sidebranching in the three-dimensional nonaxisymmetric dendritic growth”, *Physical Review E*, **51**(1):351–359, 1995.
- [66] U. Bisang and J. H. Bilgram. “Shape of the Tip and the Formation of Sidebranches of Xenon Dendrites”, *Physical Review Letters*, **75**(21):3898–3901, 1995.
- [67] U. Bisang and J. H. Bilgram. “Shape of the tip and the formation of sidebranches of xenon dendrites”, *Physical Review E*, **54**(5):5309–5326, 1996.
- [68] H. M Singer and J. H Bilgram. “Three-dimensional reconstruction of xenon dendrites”, *Europhysics Letters (EPL)*, **68**(2):240–246, 2004.
- [69] Alain Karma, Youngyih H. Lee, and Mathis Plapp. “Three-dimensional dendrite-tip morphology at low undercooling”, *Physical Review E*, **61**(4):3996–4006, 2000.
- [70] K. R. Elder, François Drolet, J. M. Kosterlitz, and Martin Grant. “Stochastic eutectic growth”, *Physical Review Letters*, **72**(5):677–680, 1994.
- [71] François Drolet, K. R. Elder, Martin Grant, and J. M. Kosterlitz. “Phase-field modeling of eutectic growth”, *Physical Review E*, **61**(6):6705–6720, 2000.

- [72] Silvère Akamatsu, Sabine Bottin-Rousseau, Gabriel Faivre, and Efim A. Brener. “Scaling Theory of Two-Phase Dendritic Growth in Undercooled Ternary Melts”, *Physical Review Letters*, **112**(10):105502, 2014.
- [73] W. Kurz and D. J. Fisher. “Fundamentals of Solidification”, Trans Tech, Lausanne, 1989.
- [74] R. Folch and M. Plapp. “Quantitative phase-field modeling of two-phase growth”, *Physical Review E*, **72**(1):011602, 2005.
- [75] Blas Echebarria, Alain Karma, and Sebastian Gurevich. “Onset of sidebranching in directional solidification”, *Physical Review E*, **81**(2):021608, 2010.
- [76] A. Parisi and M. Plapp. “Defects and multistability in eutectic solidification patterns”, *Europhysics Letters (EPL)*, **90**(2):26010, 2010.
- [77] B. Caroli, C. Caroli, B. Roulet, and J. S. Langer. “Solvability condition for needle crystals at large undercooling in a nonlocal model of solidification”, *Physical Review A*, **33**(1):442–452, 1986.
- [78] M. Ben Amar and Y Pomeau. “Theory of Dendritic Growth in a Weakly Undercooled Melt”, *Europhysics Letters (EPL)*, **2**(4):307–314, 1986.
- [79] Angelo Barbieri, Daniel C. Hong, and J. S. Langer. “Velocity selection in the symmetric model of dendritic crystal growth”, *Physical Review A*, **35**(4):1802–1808, 1987.
- [80] David A. Kessler, Joel Koplik, and Herbert Levine. “Pattern selection in fingered growth phenomena”, *Advances in Physics*, **37**(3):255–339, 1988.
- [81] Y. Saito, G. Goldbeck-Wood, and H. Müller-Krumbhaar. “Numerical simulation of dendritic growth”, *Physical Review A*, **38**(4):2148–2157, 1988.
- [82] E Brener, H Müller-Krumbhaar, and D Temkin. “Kinetic Phase Diagram and Scaling Relations for Stationary Diffusional Growth”, *Europhysics Letters (EPL)*, **17**(6):535–540, 1992.
- [83] T. Ihle and H. Müller-Krumbhaar. “Diffusion-limited fractal growth morphology in thermodynamical two-phase systems”, *Physical Review Letters*, **70**(20):3083–3086, 1993.
- [84] T. Ihle and H. Müller-Krumbhaar. “Fractal and compact growth morphologies in phase transitions with diffusion transport”, *Physical Review E*, **49**(4):2972–2991, 1994.
- [85] Silvère Akamatsu and Gabriel Faivre. “Traveling waves, two-phase fingers, and eutectic colonies in thin-sample directional solidification of a ternary eutectic alloy”, *Physical Review E*, **61**(4):3757–3770, 2000.
- [86] Mathis Plapp and Alain Karma. “Eutectic colony formation: A stability analysis”, *Physical Review E*, **60**(6):6865–6889, 1999.

- [87] Mathis Plapp and Alain Karma. “Eutectic colony formation: A phase-field study”, *Physical Review E*, **66**(6):061608, 2002.
- [88] Sebastian Gurevich, Alain Karma, Mathis Plapp, and Rohit Trivedi. “Phase-field study of three-dimensional steady-state growth shapes in directional solidification”, *Physical Review E*, **81**(1):011603, 2010.
- [89] Yiwen Ma and Mathis Plapp. “Phase-field simulations and geometrical characterization of cellular solidification fronts”, *Journal of Crystal Growth*, **385**:140–147, 2014.



# List of Publications

Publications in peer reviewed scientific journals:

- [P1] L. Rátkai, A. Szállás, T. Pusztai, T. Mohri, L. Gránásy, “Ternary eutectic dendrites: Pattern formation and scaling properties”, *Journal of Chemical Physics*, **142**:154501, 2015
- [P2] L. Gránásy, L. Rátkai, A. Szállás, B. Korbuly, Gy. Tóth, L. Környei, T. Pusztai, “Phase-Field Modeling of Polycrystalline Solidification: From Needle Crystals to Spherulites – A Review”, *Metallurgical and Materials Transactions A*, **45**:1694-1719, 2014
- [P3] T. Pusztai, L. Rátkai, A. Szállás, L. Gránásy, “Spiraling eutectic dendrites”, *Physical Review E*, **87**:032401, 2013

Publication in Hungarian:

- [P4] Szállás A., Rátkai L., Pusztai T., Gránásy L., “Helikális mintázat eutektikus ötvözetekben”, [Helical patterns in eutectic alloys], *Fizikai Szemle*, **63**(10):333-337, 2013

Further publications not included in this dissertation:

- L. Rátkai Gy. I. Tóth, T. Pusztai, L. Gránásy, “Phase-field modeling of eutectic structures on the nanoscale: the effect of anisotropy”, *Journal of Materials Science*, **52**:5544, 2017
- T. Pusztai, L. Rátkai, A. Szállás, L. Gránásy, “Phase-Field Modeling of Solidification in Light-Metal Matrix Nanocomposites”, *Magnesium Technology*, 2014
- L. Rátkai, I. Kaban, T. Wágner, J. Kolár, S. Valková, I. Voleská, B. Beuneu, P. Jóvári, “Silver environment and covalent network rearrangement in GeS<sub>3</sub>-Ag glasses”, *Journal of Physics: Condensed Matter*, **25**:454210, 2013
- L. Rátkai, C. Conseil, V. Nazabal, B. Bureau, I. Kaban, J. Bednarcik, B. Beuneu, P. Jóvári, “Microscopic origin of demixing in Ge<sub>20</sub>Se<sub>x</sub>Te<sub>80-x</sub> alloys”, *Journal of Alloys and Compounds*, **509**:5190-5194, 2011

- L. Rátkai, A.P. Gonçalves, G. Delaizir, C. Godart, I. Kaban, B. Beuneu, P. Jávári, “The Cu and Te coordination environments in Cu-doped Ge-Te glasses”, *Solid State Communications*, **151**:1524-1527, 2011

A figure (here Fig. 5.16) in our [P1] publication has been chosen for the journal cover page.

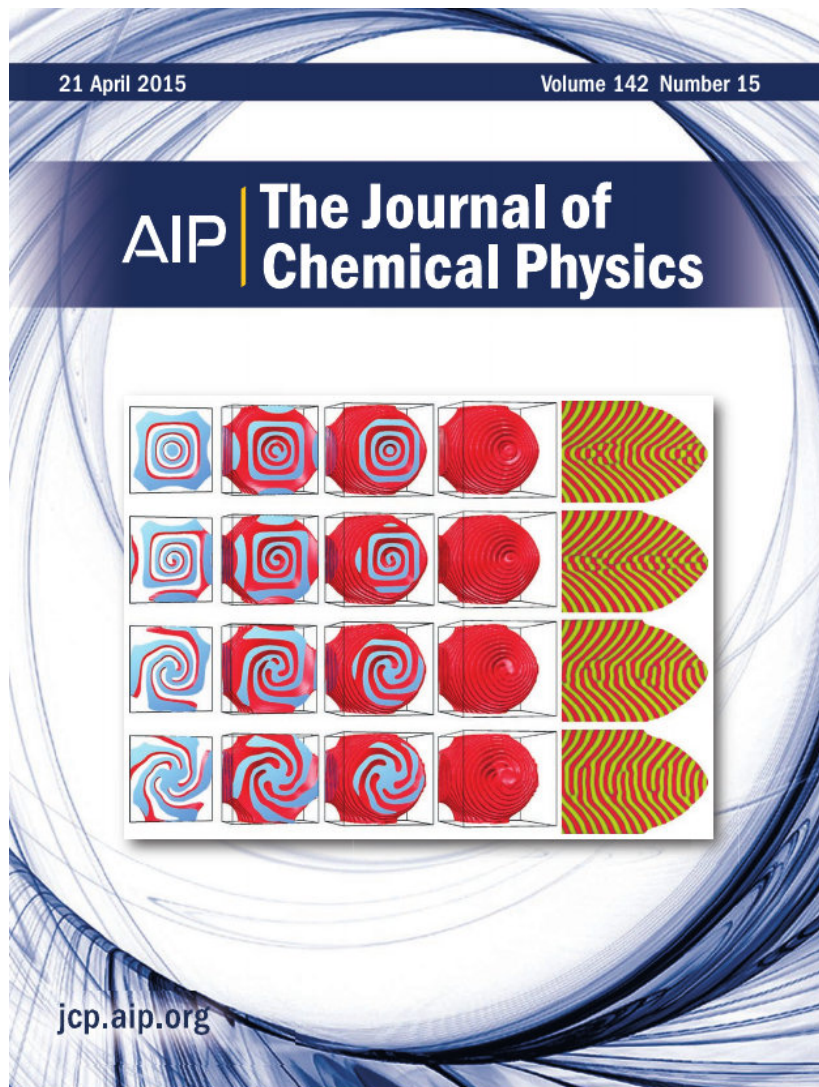


**Figure 6.1.** Dendrite cross-sections for the target pattern and single-, triple-, and five-arm spiral cases. Cover page of *Journal of Chemical Physics* volume 142, issue 15, 2015. <https://aip.scitation.org/toc/jcp/142/15>



# Theses

1. To investigate the formation of spiraling two-phase dendrites observed recently during directional solidification of transparent ternary systems, I constructed a simple ternary phase-field model that relies on ideal solution thermodynamics in the liquid and the regular solution model in the solid state. This turned out to be the first model that reproduced spiraling two-phase dendrites. I identified the stability domain of these spiraling structures both in composition and velocity space. With increasing pulling velocity, I observed the following sequence of transitions in growth morphology and eutectic pattern: flat front with disordered lamellae  $\rightarrow$  cellular structure built of eutectic colonies  $\rightarrow$  two-phase (eutectic) dendrites with a variety of ordered patterns  $\rightarrow$  one phase-dendrites without partitioning for two of the three components  $\rightarrow$  partitionless solid (due to full solute trapping) growing with a flat front. I have shown furthermore that in the case of two-phase spiraling dendrites the eutectic wavelength follows the Jackson-Hunt scaling law when the pulling velocity changes. [P1, P3]
2. I demonstrated that in addition to the single-spiral surface pattern observed experimentally, which emerges from a helical structure in the volume, the two-phase dendrites may have other eutectic motifs on their surface, such as the target pattern or multi-armed spiraling patterns that are the manifestation of layered two-phase structures or multiple helical structures in their volume. I have determined the growth mechanism of these eutectic patterns: the target pattern is formed by the alternating nucleation of the two solid phases at the tip. In the single spiral case, the two solid phases grow simultaneously via rotating around each other. At the double spirals, the two solid phases grow alternately at the tip region. The growth becomes fairly complex for more than two spiraling arms. Here the formation of eutectic patterns happens in two stages: (a) nucleation of one phase on top of the other in the tip region, (b) when it grows sufficiently large, existing spiral arms of the same phase merge with it. [P1, P2]

3. I have characterized the shape of the two-phase dendrites by two quantities: (a) I determined the tip radius from shape of the solid-liquid interface in the vicinity of the tip, (b) I used the exponent of a power-law fit in the fin direction for larger distances from the tip. I have shown that similarly to the single-phase dendrites, the tip radius of the two-phase dendrites shows a square root dependence on the solid-liquid interface energy, and both the tip radius and the exponent that characterizes the shape decreases with increasing kinetic anisotropy. I have also found, that these parameters are essentially independent of the underlying eutectic pattern. [P1, P3]
4. I have shown that a variety of eutectic patterns (target and spiraling as specified under the second thesis point) form under nominally the same physical conditions. Pattern selection is a stochastic process determined by fluctuations of the system. I have quantified pattern selection via the probability distribution of the structures with different number of spiral arms. I have found that the number of spiral arms tend to increase with increasing tip radius. [P1]
5. Using large scale simulations, I have demonstrated that anisotropy is a precondition for the formation of steady-state spiraling dendrites. In the isotropic system, the growing structures undergo dynamic tip-splitting and tip-elimination phenomena similar to the behavior observed in the case of one-phase cellular structures in experiment and phase-field simulations. Apparently, without a stable dendritic structure no steady-state spiraling pattern can form. [P1]
6. I have investigated the formation of two-phase spiraling dendrites with unequal solid phase ratio by using off-eutectic (asymmetric) composition. Two approaches were used. In the first one, I started from a steady-state single-spiral dendrite, and then gradually changed the ratio of the two major components of the incoming liquid, which eventually resulted in a spiraling structure, where the majority phase formed a homogeneous channel along the axis of the dendrite. In the second method, the composition was set from the beginning to an off-eutectic value, and the simulation was started with a homogeneous grain. Steady-state spiraling dendrites were obtained using this approach as well, where changing the phase ratio resulted in different width of the lamellae of the solid phases until a critical value. I have shown that, when the volume fractions of the two solid phases differ substantially, the regular lamellar spiraling structure is replaced by a complex shape, where the lamellae of the minority phase broke up, the holes are filled by the majority phase, yet the spiraling pattern remained. This phenomenon can be viewed as an analogy of the well-known rod to lamellar transition in binary eutectic systems, realized now in a complex helical environment. [P3]

# Résumé

During my doctoral work I have investigated the ternary eutectic dendrites using computational simulations. For the modeling I used the Phase-Field Method, that I extended to ternary systems. For the simulations I developed a program, that can run on graphical cards and CPU clusters as well to be able to handle sufficiently large systems.

I have shown that the two-phase dendrites follows on a wide interval the Jackson-Hunt scaling rule, which defines the correlation between the wavelength of the eutectic pattern and the growing velocity of the solidification front. I have identified the region on the concentration triangle, in which eutectic dendrites of ordered patterns appear. I have shown that beside the single spiraling dendrite, which was seen in the experiment, dendrites with the target pattern and also with multiple spirals arms may appear.

I have investigated the effect of solid-liquid interface energy, temperature gradient and kinetic anisotropy regarding the shape of the solidification front and the eutectic pattern. I have shown that at a given parameter set, steady-state dendrites with different number of spiral arms can form, of which the fluctuations choose during the solidification. I have characterized this stochastic behavior with peaked probability density distributions. The number of spiral arms tends to increase with increasing tip radius, that I achieved by increasing the solid-liquid interface energy, or decreasing the kinetic anisotropy.

I have shown using large scale simulations that anisotropy is required for steady-state spiraling dendrites. In the isotropic system, the growing structures tend to undergo tip-splitting and tip-elimination phenomena, which prevents the appearing of steady-state spiraling patterns.

Using asymmetric composition for the liquid, I have shown spiraling dendrites with unequal phase ratios. When the volume fractions of the two solid phases differ substantially, the regular lamellar spiraling structure is replaced by a complex shape, where the lamellae of the minority phase broke up, the holes are filled by the majority phase, yet the spiraling pattern remained. This phenomenon can be viewed as an analogy of the well-known rod to lamellar transition in binary eutectic systems, realized now in a complex helical environment.



# Összefoglaló

A doktori munkám során ternér eutektikus dendriteket vizsgáltam számítógépes szimulációk segítségével. A modellezéshez a fázismező-elméletet használtam, amelyet kibővítettem három komponensű rendszerek kezelésére. A szimulációkhoz kifejlesztettem egy programot, amely grafikus kártyákat és CPU klasztert is képes használni, ezáltal elegendően nagy rendszereket tudtam szimulálni.

Megmutattam, hogy a kétfázisú eutektikus dendritek széles tartományon teljesítik a Jackson-Hunt skálázódást, ami az eutektikus mintázat hullámhossza és a megszilárdulási front növekedési sebessége között ad összefüggést. Azonosítottam azt a tartományt a koncentráció-háromszögön, ahol rendezett eutektikus mintázattal rendelkező kétfázisú dendritek keletkeznek. Megmutattam, hogy a kísérletekben látott egy spirálkarú dendritek mellett céltábla mintázatú, illetve több spirálkarral rendelkező dendritek is létrejöhetnek.

Feltérképeztem a dendritek alakjára és az eutektikus mintázatra kifejtett hatását a szilárd-folyadék felületi szabadenergiának, a húzási sebességnek és a kinetikus anizotropiának. Megmutattam, hogy adott paraméterek mellett különféle stabil mintázatú dendritek jöhetnek létre, a rendszerben jelen lévő fluktuációk döntik el, hogy melyik mintázat valósul meg a megszilárdulás során. Ezt a sztochasztikus viselkedést csúccsal rendelkező eloszlásokkal jellemeztem. A spirálkarok várható száma növekedett ahogy nőtt a dendritek görbületi sugara, amit a felületi szabadenergia növelésével illetve a kinetikus anizotropia csökkentésével értem el.

Megmutattam nagyskálás szimulációk segítségével, hogy a stabil spirális mintázatú dendritekhez szükség van kinetikus anizotropiára. Anizotropia nélkül ugyanis nem alakulnak ki stabil dendrites szerkezetek; a kialakuló csúcsok időnként szétválnak, és lelassulva eltűnnek a rendszerből, ami megakadályozza a stabil spirális mintázat kialakulását.

Bemutattam aszimmetrikus fázisarányú spirális dendriteket a folyadék összetételét változtatva. Amikor a fázisok térfogati aránya már jelentősen eltért egymástól, akkor a szabályos spirális szerkezet átalakult egy komplex alakzattá, ahol a kisebbségi fázis lamellái felszakadoztak, azonban a spirális mintázat továbbra is megmaradt. Ez a jelenség a binér eutektikus rendszerekben, sík fronton megfigyelt rudas-lamellás átalakulás komplex helikális környezetben megvalósuló analógiájának tekinthető.



# Acknowledgments

First of all, I would like to express my gratitude and thanks to my supervisor, Tamás Pusztai, for his great guidance and continuous help during my scientific work. I also wish to express my appreciation and thanks to our group leader, László Gránásy, for his valuable advice and ideas and the constant encouragement to do more simulations to investigate new, interesting topics, and also for providing the financial basis to our group with his successful grants. [This work has been supported by the EU FP7 projects “ENSEMBLE” and “EXOMET” (co-founded by ESA).] I also thank for his contributions to my former colleague, Attila Szállás, with whom I started to work on this topic.

I thank Mathis Plapp, Silvère Akamatsu and Zoltán Rácz for the enlightening discussions, and Tetsuo Mohri for providing access to the supercomputer in Tohoku University, Sendai, Japan. I am grateful to Ágnes Buka and Aladár Czitrovsky, the former and acting director of the Institute of Solid State Physics and Optics, and Péter Lévai the director general of the Wigner RCP for providing the work facilities. I am also grateful to my colleagues in the Computational Materials Science Group and the members of Department of Experimental Solid State Physics for the pleasant atmosphere.

Last but not least, I would like to thank my family for their support.





# ADATLAP

## a doktori értekezés nyilvánosságra hozatalához\*

### I. A doktori értekezés adatai

A szerző neve: Rátkai László

MTMT-azonosító: 10029286

A doktori értekezés címe és alcíme: Phase-Field Modeling of Spiral Eutectic Dendrites

DOI-azonosító: 10.15476/ELTE.2018.072

A doktori iskola neve: ELTE TTK Fizika Doktori Iskola

A doktori iskolán belüli doktori program neve: Anyagtudomány és szilárdtestfizika

A témavezető neve és tudományos fokozata: Dr. Pusztai Tamás, az MTA doktora

A témavezető munkahelye: MTA Wigner Fizikai Kutatóközpont, SZFI

### II. Nyilatkozatok

#### 1. A doktori értekezés szerzőjeként

a) hozzájárulok, hogy a doktori fokozat megszerzését követően a doktori értekezésem és a tézisek nyilvánosságra kerüljenek az ELTE Digitális Intézményi Tudástárban. Felhatalmazom a Természettudományi kar Dékáni Hivatal Doktori, Habilitációs és Nemzetközi Ügyek Csoportjának ügyintézőjét, hogy az értekezést és a téziseket feltöltse az ELTE Digitális Intézményi Tudástárba, és ennek során kitöltse a feltöltéshez szükséges nyilatkozatokat.

b) kérem, hogy a mellékelt kérelemben részletezett szabadalmi, illetőleg oltalmi bejelentés közzétételéig a doktori értekezést ne bocsássák nyilvánosságra az Egyetemi Könyvtárban és az ELTE Digitális Intézményi Tudástárban;

c) kérem, hogy a nemzetbiztonsági okból minősített adatot tartalmazó doktori értekezést a minősítés (*dátum*)-ig tartó időtartama alatt ne bocsássák nyilvánosságra az Egyetemi Könyvtárban és az ELTE Digitális Intézményi Tudástárban;

d) kérem, hogy a mű kiadására vonatkozó mellékelt kiadó szerződésre tekintettel a doktori értekezést a könyv megjelenéséig ne bocsássák nyilvánosságra az Egyetemi Könyvtárban, és az ELTE Digitális Intézményi Tudástárban csak a könyv bibliográfiai adatait tegyék közzé. Ha a könyv a fokozatszerzést követően egy évig nem jelenik meg, hozzájárulok, hogy a doktori értekezésem és a tézisek nyilvánosságra kerüljenek az Egyetemi Könyvtárban és az ELTE Digitális Intézményi Tudástárban.

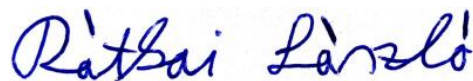
#### 2. A doktori értekezés szerzőjeként kijelentem, hogy

a) az ELTE Digitális Intézményi Tudástárba feltöltendő doktori értekezés és a tézisek saját eredeti, önálló szellemi munkám és legjobb tudomásom szerint nem sértem vele senki szerzői jogait;

b) a doktori értekezés és a tézisek nyomtatott változatai és az elektronikus adathordozón benyújtott tartalmak (szöveg és ábrák) mindenben megegyeznek.

3. A doktori értekezés szerzőjeként hozzájárulok a doktori értekezés és a tézisek szövegének plágiumkereső adatbázisba helyezéséhez és plágium-ellenőrző vizsgálatok lefuttatásához.

Kelt: Budapest, 2018.04.23.



.....  
a doktori értekezés szerzőjének aláírása